



저작자표시-비영리-변경금지 2.0 대한민국

이용자는 아래의 조건을 따르는 경우에 한하여 자유롭게

- 이 저작물을 복제, 배포, 전송, 전시, 공연 및 방송할 수 있습니다.

다음과 같은 조건을 따라야 합니다:



저작자표시. 귀하는 원저작자를 표시하여야 합니다.



비영리. 귀하는 이 저작물을 영리 목적으로 이용할 수 없습니다.



변경금지. 귀하는 이 저작물을 개작, 변형 또는 가공할 수 없습니다.

- 귀하는, 이 저작물의 재이용이나 배포의 경우, 이 저작물에 적용된 이용허락조건을 명확하게 나타내어야 합니다.
- 저작권자로부터 별도의 허가를 받으면 이러한 조건들은 적용되지 않습니다.

저작권법에 따른 이용자의 권리는 위의 내용에 의하여 영향을 받지 않습니다.

이것은 [이용허락규약\(Legal Code\)](#)을 이해하기 쉽게 요약한 것입니다.

[Disclaimer](#)

공학박사학위논문

**Study on Coupling of Lower Hybrid Fast
Wave in Versatile Experiment Spherical
Torus (VEST)**

VEST 장치에서의 고속파 결합 연구

2019년 2월

서울대학교 대학원

에너지시스템공학부

조 종 갑

Abstract

Study on Coupling of Lower Hybrid Fast Wave in Versatile Experiment Spherical Torus (VEST)

JongGab Jo

Department of Energy System Engineering

(Fusion & Plasma Engineering)

The Graduate School

Seoul National University

Fast wave branch in lower hybrid resonance frequency range, especially higher than $2\omega_{lh}$, has been proposed for central or off-axis electron heating and current drive in higher density plasmas than that of slow wave scheme. Cutoff density for the LHF (Lower Hybrid Fast Wave) launching is usually several hundred times higher than that of the LHSW (Lower Hybrid Slow Wave). And rather higher frequency of LHF for high E_z than the other fast waves causes narrow coupling window. Therefore, efficient coupling between antenna and plasma would be a priority issue for the feasibility of LHF. Accessibility conditions are also expected to be significantly modified from linear theory due to $n_{||}$ -upshift that is assumed to bridge the spectral gap for absorption of lower hybrid waves. Intensive investigation on coupling and propagation is an essential starting point of the proof-of-principle of LHF scheme for current drive.

Characteristics of fast wave coupling depending on wave frequency, gap size and electron density profile is investigated using a commercial full wave FEM solver,

COMSOL. Maximum coupling between comb-line antenna and plasma is expected to be at $\sim 500\text{MHz}$ with $n_{\parallel 0} \sim 4.5$. Coupled power ranges from 90% to 60% in gap size between 0.5cm and 1.5cm. Relative power fraction of fast wave is larger than 80% at these conditions. Propagation and coupling power of the fast wave is crucially dependent on plasma density window which is determined by launching and confluence densities. Preliminary experimental results with low power signal generator demonstrate that measured coupling efficiency starts to increase as electron density in front of antenna attains the level of cutoff density for the fast wave propagation. The experimental results are consistent with the coupling simulation using full wave solver in low density plasma ($n_{cutoff,fast} < n_e < n_{confluence}$), but enhanced fast wave coupling is observed contrary to the prediction in high density plasma ($\geq n_{confluence}$) where accessibility condition is not satisfied. The discrepancy between experimental observation and coupling simulation implies that another factor plays a major role in high density plasma overcoming the accessibility limit. To identify cause for the discrepancy between experimental results and coupling simulation, wave measurement in plasma is desired for more information on coupling and propagation of fast wave.

Experimental investigation of LHFV coupling and propagation is carried out with wave measurements utilizing magnetic probes in Versatile Experiment Spherical Torus (VEST). Coupling experiments are conducted in marginal ($n_e \geq n_{confluence}$) and prohibited ($n_e \gg n_{confluence}$) regimes for fast wave coupling. In the marginal regime of $I_p = 25\text{ kA}$, about two folds of n_{\parallel} -upshift is observed. Propagation path of fast wave is largely modified compared to that of full wave simulation and more fast waves are detected inside the last-closed-flux surface despite unsatisfied accessibility condition. Since spectral broadening is measured to be narrow and linearly proportional to coupled wave power with high density fluctuation of about 20% in the frequency range

($\omega_0/\omega_{lh} \sim 15$), it is thought to be crucially correlated with wave scattering rather than parametric decay instabilities. Consequently, the spectral broadening implicates that n_{\parallel} -upshift can take place via wave scattering mechanism. In the prohibited regime of $I_p = 100$ kA, more enhanced coupling of up to 90% is observed with similar density fluctuation to that of the marginal regime, which is explained with intensified wave scattering due to high dielectric constant of spherical torus plasmas.

In conclusion, practical window for propagation and coupling of LHFV, which is the first difficulty of the scheme, is widened with the aid of n_{\parallel} -upshift via wave scattering even though the accessibility condition is not satisfied right in front of the antenna. Significant n_{\parallel} -upshift is measured by magnetic probe array for the first time. Wave measurements reveal that accessibility conditions are largely modified from full wave simulation based on linear model by the n_{\parallel} -upshift and wave scattering. This study give new evidences of the n_{\parallel} -upshift in edge plasma for lower hybrid waves.

Keywords: Lower Hybrid Fast Wave, Spherical Torus, Coupling, accessibility condition, n_{\parallel} -upshift, wave scattering.

Student Number: 2013-30997

Table of Contents

Abstract	i
Table of Contents	iv
List of Tables	vi
List of Figures	vii
Chapter 1. Introduction	1
1.1. Nuclear Energy and Fusion.....	1
1.2. Tokamak.....	3
1.3. Spherical Torus (ST).....	5
1.4. Non-Inductive Current Drive by RF Waves	7
1.4.1. Lower Hybrid Slow Wave (LHSW)	8
1.4.2. Lower Hybrid Fast Wave (LHFW)	9
1.4.3. Spectral Gap Problem	11
1.5. Objective of Research.....	13
Chapter 2. Lower Hybrid Fast Wave (LHFW)	14
2.1. Dispersion Relation	14
2.2. Coupling and Absorption of LHFW in ST	17
Chapter 3. Experimental Setup	19
3.1. RF System.....	19
3.1.1. Comb–line Antenna.....	19
3.1.2. Klystron System.....	24
3.2. Diagnostics.....	28
3.2.1. RF Diagnostics	28
3.2.2. Langmuir Probe [47]	30
3.2.3. Magnetic Probe Array.....	32

Chapter 4. Antenna-Plasma Coupling Simulation [53]	36
4.1. COMSOL Multiphysics Modelling.....	36
4.2. Coupling Study	42
4.2.1. Wave Frequency Effect	42
4.2.2. Gap Size Effect	45
4.2.3. Electron Density Effect	47
4.3. Comparison with Preliminary Experiment	53
Chapter 5. Fast Wave Coupling Experiments [52]	57
5.1. Detection of $n_{ }$ -upshift and Modified Propagation Path.....	57
5.2. Frequency Spectral Broadening by Wave Scattering.....	65
5.3. Enhanced Coupling of LHF in High Density Plasmas	68
5.4. Wave Scattering Effect on the Expanded Accessibility Conditions....	72
Chapter 6. Conclusion	78
6.1. Summary and Conclusion.....	78
6.2. Future Work	81
APPENDIX A. Antenna Conditioning [46]	82
A.1. Immediate antenna operations after vacuum closing	82
A.2. Analyses of Outgassing Characteristics.....	86
A.3. Improvement of Antenna Performance by RF conditioning.....	90
Bibliography	92

List of Tables

Table 4.1 Summarized input parameters for the coupling simulations.	38
Table 4.2 Summarized coefficients of each electron density profile cases (unit: %).	50

List of Figures

Figure 1.1 Cross-section for fusion reactions [2].	2
Figure 1.2 Schematic diagram of tokamak geometry [8].	4
Figure 1.3 Progress in plasma confinement performance of tokamaks [9].	4
Figure 1.4 Schematic diagram of ST geometry compared to that of tokamak [8].	6
Figure 1.5 High beta operation for STs [8].	6
Figure 1.6 Fast waves for heating and current drive in fusion device (n : ion cyclotron harmonic number) [21].	10
Figure 1.7 Parallel refractive indexes of tokamak devices [28].	12
Figure 2.1 Perpendicular refractive indexes of the fast and slow wave in CMA diagram.	14
Figure 2.2 Real part of the perpendicular index of the fast and slow wave as a function of plasma density when (a) $B_0 = 0.1\text{T}$ and (b) $B_0 = 0.2\text{T}$.	15
Figure 2.3 Ratio between imaginary part of the refractive index of the fast and slow wave as a function of plasma density.	18
Figure 3.1 Picture of a comb-line antenna designed and built by GA and installed on JFT-2M [42].	20
Figure 3.2 Equivalent circuit of the comb-line antenna [44].	20
Figure 3.3 A comb-line antenna fabricated and installed in VEST chamber.	21
Figure 3.4 $n_{\parallel 0}$ of designed comb-line antenna.	22
Figure 3.5 S-parameters (S_{11} , S_{21}) and coefficients (R, T, and R+T) of combline antenna installed in VEST [46].	23
Figure 3.6 Schematic diagram of RF system [20].	24
Figure 3.7 Pictures of LHFWRF system (klystron, high voltage DC power supply, transmission line and dummy load) installed in VEST device.	25
Figure 3.8 Frequency response of klystron.	26

Figure 3.9 RF injection into dummy load for klystron test.	26
Figure 3.10 Operation procedures of RF system for VEST experiment.	27
Figure 3.11 Schematic diagram of RF system with VEST chamber.	29
Figure 3.12 Calibration results of power detector and phase detector at 500 MHz.	29
Figure 3.13 Schematic diagram of (a) potential at each tips and (b) measurement circuit of triple probe.	31
Figure 3.14 Fabricated triple probe.	32
Figure 3.15 Pictures of fabricated magnetic probes.	33
Figure 3.16 COMSOL simulation to verify slit effect for separating orthogonal polarization of magnetic fields. (a) Simulation domain and (b) Simulation results.	33
Figure 3.17 Calibration results of one turn loop coils at 500 MHz using Helmholtz coil for known magnetic field source [52].	34
Figure 3.18 Location of magnetic probes installed in VEST chamber [52].	35
Figure 4.1 Schematic drawings of the antenna and simulation domains for the antenna-plasma coupling simulation.	39
Figure 4.2 Total coupling power and the coupled power of fast wave and slow wave calculated from the surface integral of each Poynting vector. B_0 is 0.2T, wave frequency is 500MHz, gap size is varied from 0.5cm to 2cm and $n_{\text{cutoff, fast}} <$ $n_e < n_{\text{confluence}}$	41
Figure 4.3 (a) S-parameter, (b) transmission (T), reflection (R) and coupling (C) coefficient, (c) relative fraction of coupled fast wave and slow wave, and (d) input power fraction of coupled fast wave and slow wave depending on wave frequency. B_0 is 0.2T, gap size is 0.5cm and $n_{\text{cutoff, fast}} < n_e < n_{\text{confluence}}$	43
Figure 4.4 (a) Spectrum of n_{\parallel} and (b) $n_{\parallel 0}$ of excited wave from the comb-line antenna depending on wave frequency.	44

Figure 4.5 (a) S-parameter, (b) transmission (T), reflection (R) and coupling (C) coefficient, (c) relative fraction of coupled fast wave and slow wave, and (d) input power fraction of coupled fast wave and slow wave depending on gap size. B_0 is 0.2T, wave frequency is 500MHz and $n_{\text{cutoff, fast}} < n_e < n_{\text{confluence}}$46

Figure 4.6 Radial density profiles of (a) cutoff density for fast wave and slow wave and confluence density, and (b) field patterns of fast wave (E_y) and slow wave (E_ϕ) depending on density profiles. B_0 is 0.2T, wave frequency is 500MHz and gap size is 0.5cm.49

Figure 4.7 (a) Transmission (T), reflection (R) and coupling (C) coefficients, (b) relative fraction of fast and slow wave, and (c) input power fraction of fast and slow wave depending on edge electron density. $B_0 = 0.2T$, $f = 500\text{MHz}$ and gap size is 0.5cm.51

Figure 4.8 Field patterns of fast wave (E_y) and slow wave (E_ϕ) depending on edge density under $B_0 = 0.1T$. (a) E_y , (b) E_ϕ field in case of $n_{\text{cutoff, fast}} < n_e < n_{\text{confluence}}$, and (c) E_y , (d) E_ϕ field in case of $n_e \sim n_{\text{confluence}}$. Wave frequency is 500MHz and gap size is 0.5cm.52

Figure 4.9 (a) Radial profiles of electron density for four temporal points, and (b) time evolution of discharge #17703.55

Figure 4.10 (a) Field patterns of fast wave (E_y) and slow wave (E_ϕ) depending on measured edge electron density of #17703. (a) E_y , (b) E_ϕ field at $t = 304$ ms, and (c) E_y , (d) E_ϕ field at $t = 308$ ms. B_0 is 0.1T, wave frequency is 500MHz and gap size is 0.5cm.56

Figure 5.1 (a) Time evolution of plasma current, limiter current, edge electron density, RF power and coefficients of reflection and coupling in ohmic discharge (#19526) at $B_0 = 0.1$ T. (b) Power spectrums of \mathbf{B}_ϕ and \mathbf{B}_y fields. (c) n_{\parallel} of \mathbf{B}_ϕ field detected at MP1 and $n_{\parallel 0}$ spectrum of \mathbf{B}_ϕ field calculated from COMSOL simulation. Measurement results of (b) and (c) are from MP1 at $t =$

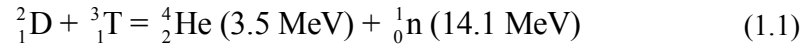
304 ms in the shot # 19526.	59
Figure 5.2 (a) Plasma current of reproduced ohmic discharges. (b) Radial profile of toroidal field strength, poloidal field strength and pitch angle at $I_p \sim 25$ kA. (c) Plasma boundary from equilibrium reconstruction of shot #19526 and location of magnetic probes (MP2) in poloidal plane of VEST. (Surface of $\psi_N = 0.95$ and position of MP2 are displayed as red dot line and blue solid line respectively.) .	60
Figure 5.3 (a) Radial profiles of n_{\parallel} measured at MP1 and MP2. (b) Radial profiles of n_{\perp} measured at MP2. (c) n_{\perp} of slow wave and fast wave as a function of plasma density derived from dispersion relation. (Shaded region signifies the range of n_{\perp} measured at MP2 considering the range of n_{\parallel} and edge n_e .).....	63
Figure 5.4 Radial profiles of pump wave power measured at MP2 and calculated from COMSOL simulation (Coupled wave power: 670 W and 1550 W).	64
Figure 5.5 (a) Power spectrums of B_{ϕ} field measured at MP1 and MP2. (b) Radial profile of broadening width of power spectrums measured at MP1 and MP2.	66
Figure 5.6 (a) Broadening width as a function of coupled wave power measured at MP1 and MP2 ($Z = -0.346$ m). (b) Fluctuation of ion saturation current during ohmic discharges in the SOL measured by a Langmuir probe ($R = 0.745$ m, $Z = 0$ m).....	67
Figure 5.7 (a) Time evolution of plasma current, limiter current, edge electron density, RF power and coefficients of reflection and coupling in ohmic discharge (#20245) at $B_0 = 0.1$ T. (b) Radial profile of B_t , B_p and pitch angle at $I_p \sim 100$ kA.	69
Figure 5.8 Coefficients of reflection (R) and coupling (C) as a function of edge electron density ($R = 0.745$ m). (Confluence density for $n_{\parallel 0} = 4.5$ and	

$n_{\parallel} = 8.5$ is displayed as dash dot line and dash line respectively.)	71
Figure 5.9 Expanded propagation region in high density plasma with n_{\parallel} -upshift.	71
Figure 5.10 Fluctuation of ion saturation current and of square of ion saturation current in the SOL as a function of the distance between the radial position of antenna and the LCFS ($I_p \sim 90\text{kA}$).	72
Figure 5.11 Coefficients of coupling and reflection under $B_0 = 0.1\text{ T}$ and 0.05 T discharges as a function of (a) edge electron density and (b) plasma dielectric constant at $R = 0.745\text{ m}$	76
Figure 5.12 Minimum parallel refractive index in order to satisfy accessibility condition as a function of the plasma dielectric constant.	77
Figure A.1 Schematics of RF system, VEST chamber and diagnostic devices from (a) top and (b) side view.	84
Figure A.2 Power and coefficients of transmission, reflection and dissipation in the antenna as a function of input power before the RF conditioning.....	85
Figure A.3 Fraction of outgassing sources measured by RGA during RF conditioning for 1 hour (30 pulses).	87
Figure A.4 Outgassing rate as a function of dissipated power.	87
Figure A.5 Change of figure-of-merit during RF conditioning shots.....	89
Figure A.6 Transmission, reflection and dissipation coefficients change depending on figure-of-merit (Q/P_d).	89
Figure A.7 (a) Transmission, reflection, and dissipation coefficients before and after RF conditioning. (b) Optimized performance of the antenna for 3 days a week.....	91

Chapter 1. Introduction

1.1. Nuclear Energy and Fusion

Nuclear energy is released by mass defect through fission or fusion reaction of nucleus. Amount of the energy is according to the principle of mass-energy equivalence which is described by Einstein's formula: $E = mc^2$. Nuclear fission and fusion reaction are process of splitting an atom and combining atoms, respectively. In fact, nuclear energy was explored intensively for the development of a nuclear weapon utilizing nuclear fission reaction during World War II. After the monumental success of Manhattan project, atomic bombs were made and used by USA in order to end the war. Mankind witnessed devastating destruction of humans by their own hands. However, more powerful nuclear weapons so called hydrogen bomb were successfully realized again during the Cold war. The hydrogen bomb utilized nuclear fusion reaction, which requires extremely high temperature of fuels to break the barrier for the reaction, with the aid of released energy by explosion of atomic bomb. Nuclear energy was too massive and dangerous to be used for a military purpose only. The International Atomic Energy Agency (IAEA) was established in 1957 for peaceful use of the nuclear energy. Nuclear fission has been utilized for power plant to generate electricity reliably for a long time in the world. It is contributing to a reduction in greenhouse gas which is released from burning fossil fuels. Nuclear fusion for a reactor is more challenging goal to be achieved. Fusion is originally the process that sustains stars by generating energy. From the beginning, the Earth and its inhabitants have already used the fusion energy from the Sun unconsciously. Among the fusion reactions most compromising reaction is DT reaction which fuses deuterium and tritium into an alpha particle with a neutron as follows [1]:



Cross-section for the fusion reactions are shown in Figure 1.1. DT reaction still requires temperature above 10 keV. To attain the fusion condition in controlled experiments, strong confinement of fuels and energy should be realized by strong inward force as gravitation of the Sun. Confinement by magnetic field has been researched for decades and the most pioneering concept of the magnetic confinement is a Tokamak.

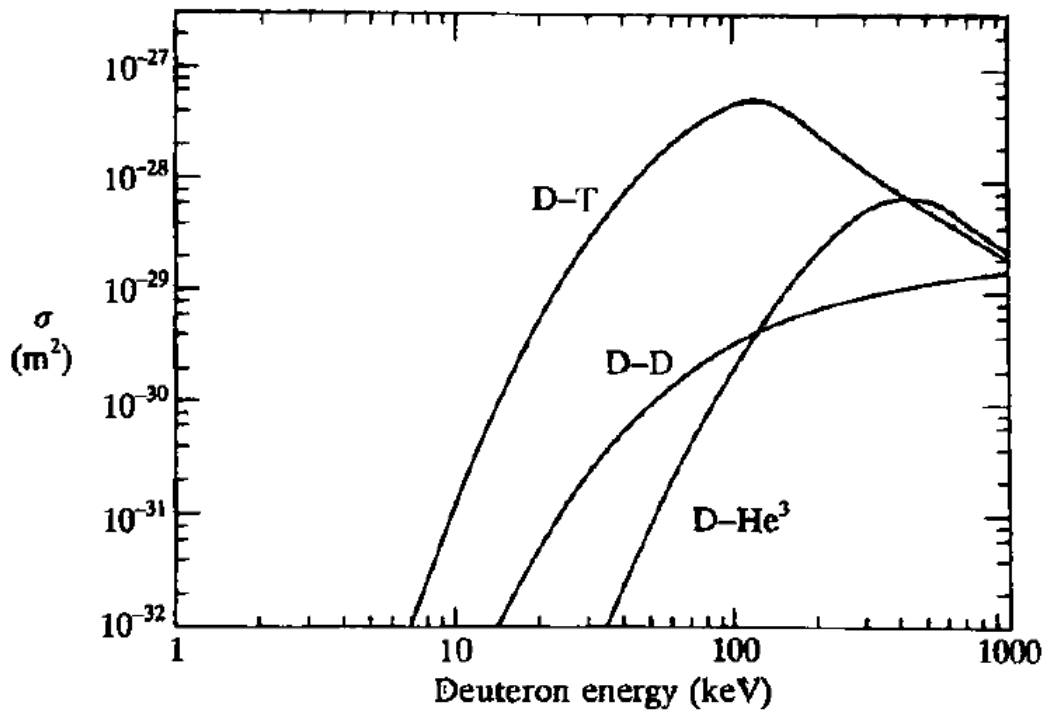


Figure 1.1 Cross-section for fusion reactions [2].

1.2. Tokamak

Tokamak was originally proposed in 1950s by Soviet physicists Tamm and Sakharov to confine a hot plasma in the torus geometry with toroidal magnetic field produced by outer coils and poloidal magnetic field produced by plasma current in toroidal direction. Etymology of the word ‘tokamak’ actually means toroidal chamber with magnetic coils [3]. Geometry of tokamak is depicted in Figure 1.2. Particles are confined along the encircled strong toroidal magnetic field line but consequent outward forces are induced by the toroidal magnetic field. To cancel out the forces, poloidal magnetic field produced by plasma current should be added to toroidal magnetic field making helical magnetic field lines. Great success of T-10 (~ 1 keV by ohmic heating) at Soviet and PLT (multi-keV by NBI) at USA in 1975 [3] made the tokamak concept become a main stream in fusion research all over the world. Performance of the fusion device can be simply evaluated by the triple product, $n\tau T$, and it shows remarkable advances in tokamak research as presented in Figure 1.3. Built on operation of major devices such as TFTR [4], JET [5] and JT-60 [6] with various tokamak researches, international cooperation started to construct the largest facility in the world to demonstrate the feasibility of tokamak scheme as a fusion reactor. International Thermonuclear Experimental Reactor (ITER) [7] project has been running from the year of 1988 under the auspices of the IAEA. Present ITER members are the European Union, China, India, Japan, Korea, Russia and the United States.

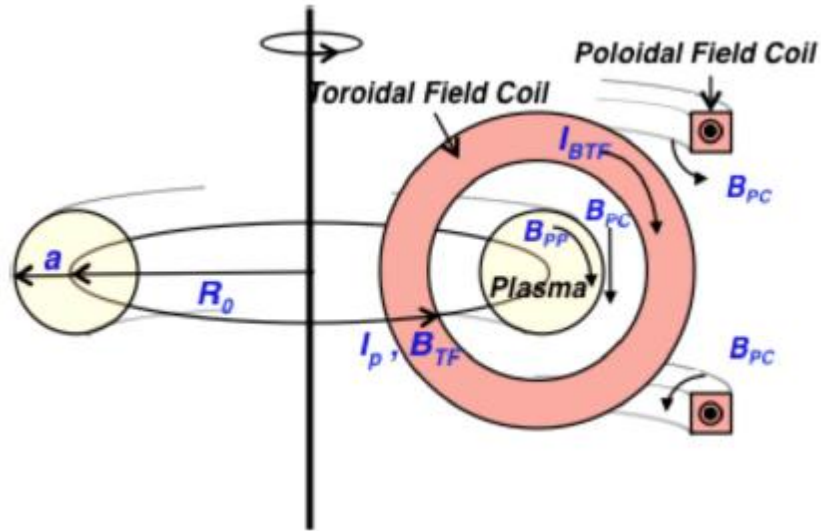


Figure 1.2 Schematic diagram of tokamak geometry [8].

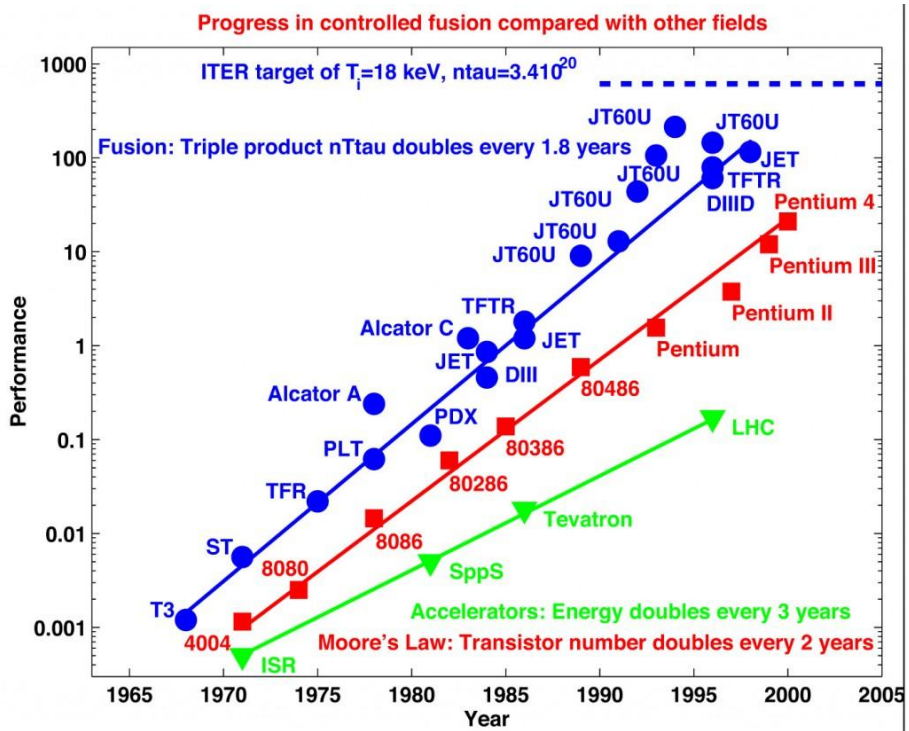


Figure 1.3 Progress in plasma confinement performance of tokamaks [9].

1.3. Spherical Torus (ST)

Spherical Torus (ST) came from concept of a low aspect ratio tokamak geometry. The aspect ratio (A) is the ratio of major radius (R_0) to minor radius (a) as following:

$$A = \frac{R_0}{a} \quad (1.2)$$

Generally, conventional tokamaks have $A \geq 2.5$ and ST have $A \leq 2.0$ with compact geometry. Geometry of ST is depicted in Figure 1.4. One of the great advantages of ST is high beta ($\sim 1/A$) plasma compared to the conventional tokamaks. Ideal tokamak beta, β , is defined as the ratio of plasma pressure to magnetic pressure indicating degree of plasma confinement at a given magnetic field as following:

$$\beta = \frac{p}{B^2 / 2\mu_0} \quad (1.3)$$

Toroidal beta, β_t , is often used for the efficiency of plasma confinement. Fusion power is proportional to $\beta_t^2 B_t^4$. Figure 1.5 presents high beta regime of STs reaching to $\sim 40\%$ while maximum beta of conventional tokamaks is about 10 %. Since the pioneering results of high beta operation in START [10], two mega-ampere class ST facilities, NSTX [11] and MAST [12], have been operated from 2000's. Geometrical compactness and high performance make STs be considered as attractive candidate for the fusion reactor and also efficient fusion neutron source in future.

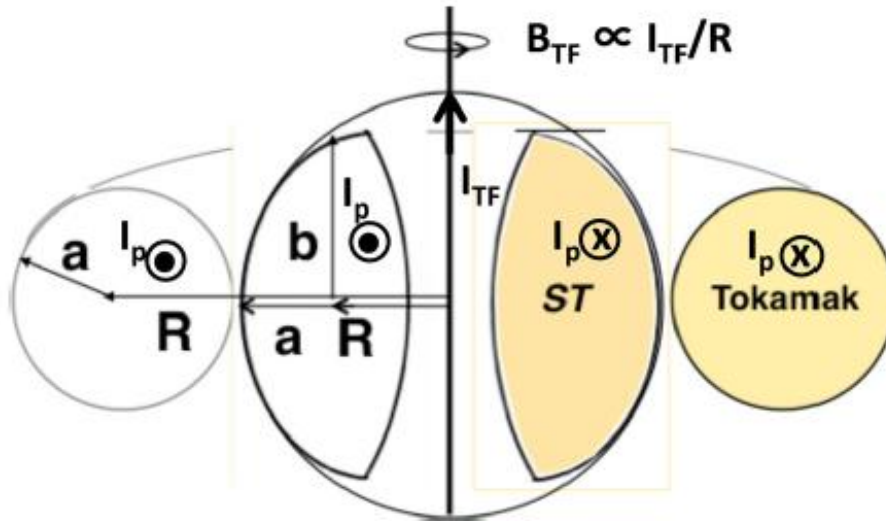


Figure 1.4 Schematic diagram of ST geometry compared to that of tokamak [8].

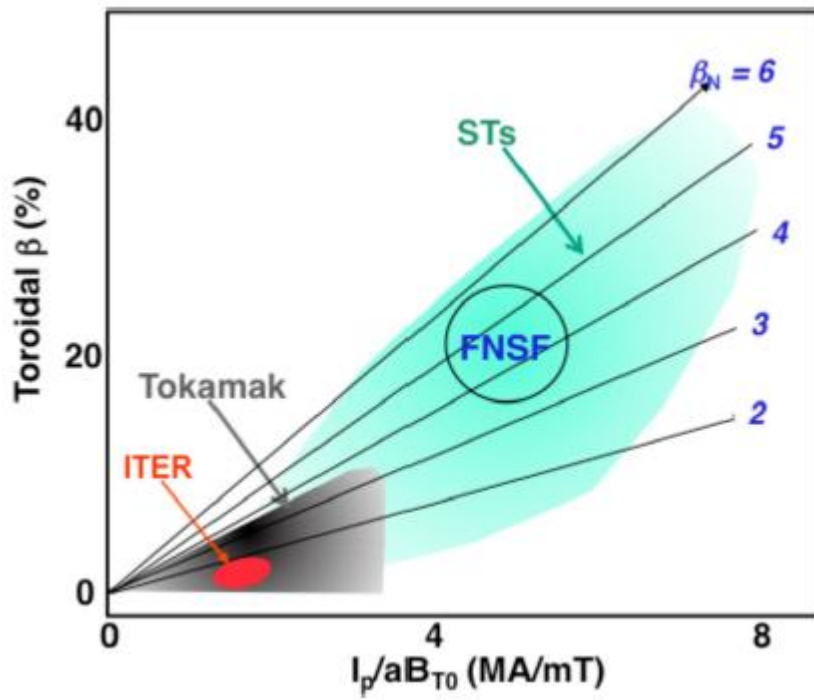


Figure 1.5 High beta operation for STs [8].

1.4. Non-Inductive Current Drive by RF Waves

To avoid the severe mechanical fatigue of structures in machine and to maximize economics of a reactor, continuous operation of tokamak is the most challenging issue. Tokamak is intrinsically pulsed operation device due to its inductive current drive method by transformer action of coils. It is expected that most of plasma heating and current drive will be fulfilled with self-heating by alpha particles and self-generated bootstrap current in a reactor grade plasmas but still shortages of the heating and current drive should be filled up with other non-inductive method. RF waves have been researched for the heating and current drive method in wide range of frequencies from several MHz to hundreds GHz. Especially, current drive by asymmetry heating on electrons is widely utilized according to the driving frequency range such as lower hybrid current drive (LHCD), electron cyclotron current drive (ECCD) and fast wave current drive (FWCD).

RF waves transfer energy to selective particles by collisionless wave-particle interactions which can be classified as Landau damping and magnetic pumping for parallel acceleration and cyclotron damping for perpendicular acceleration. Landau damping and magnetic pumping push resonant particles, which satisfy the relation $\omega - k_{\parallel}v_{\parallel} = 0$, along to magnetic field by parallel electric field (E_z) of the wave and by compressional component ($(\mu \cdot \nabla)B$ force) of the wave, respectively. Absorption power for Maxwellian distribution is expressed as follows [13]:

$$P_{LD}^{\alpha} \cong \frac{\omega}{8\pi} \frac{\omega_{p\alpha}^2}{\omega^2} \cdot 2\sqrt{\pi} \frac{\omega^3}{|k_{\parallel}|^3 v_{th\alpha}^3} e^{-\frac{\omega^2}{k_{\parallel}^2 v_{th\alpha}^2}} \cdot |E_z|^2 \quad (1.4)$$

$$\begin{aligned}
P_{MP}^\alpha &\cong \frac{\omega}{8\pi} \frac{\omega_{p\alpha}^2}{\omega^2} \frac{k_\perp^2 v_{th\alpha}^2}{\Omega_{c\alpha}^2} \cdot \sqrt{\pi} \frac{\omega}{|k_\parallel| v_{th\alpha}} e^{-\frac{\omega^2}{k_\parallel^2 v_{th\alpha}^2}} |E_y|^2 \\
&= \frac{\omega}{8\pi} \beta_\alpha \left| \frac{c}{\omega} \vec{k}_\perp \times \vec{E}_\perp \right|^2 \cdot \sqrt{\pi} \frac{\omega}{|k_\parallel| v_{th\alpha}} e^{-\frac{\omega^2}{k_\parallel^2 v_{th\alpha}^2}}
\end{aligned} \tag{1.5}$$

Landau damping conditions are easily satisfied by electrons rather ions and strong damping occurs at high frequency range of lower hybrid wave (LHW) with slow wave polarization. Magnetic pumping is considerable only at low frequency range such as high harmonic fast wave (HHFW). RF heating is simply possible using these wave-particle interactions but current drive can be achieved by asymmetry heating on resonant electrons. LHW directly deposit toroidal momentum into fast electrons which have much lower collisionality than thermal electrons. Physical picture of the current drive on the fast electrons can be described by relations as follows [14]:

$$\frac{J}{P_d} = -\frac{q}{mv_\parallel v(v)} \left(\Delta j = \Delta \varepsilon \frac{q}{mv_\parallel}, P_d = v \Delta \varepsilon \right) \tag{1.6}$$

$$\frac{J}{P_d} \propto v_\parallel^2 \quad (\text{for fast electrons, } v_\parallel \gg v_T, v \sim 1/v_\parallel^3) \tag{1.7}$$

where Δj is an incremental current and $\Delta \varepsilon$ is an incremental energy. The efficiency expressed by driven current per dissipated power is proportional to square of parallel velocity of resonant electrons leading to utilization of the high parallel velocity LHW ($\omega = k_\parallel v_\parallel$) for current drive scheme.

1.4.1. Lower Hybrid Slow Wave (LHSW)

From the Fisch's theoretical background in 1978 [15], LHCD using the slow wave branch in LHW range have been the most efficient non-inductive current drive scheme for various tokamak plasmas. Steady-state current was driven up to nearly 0.5 MA level at PLT [16] device in the early 1980's. JET [17] utilized 3 MA LHCD and TRIAM-1M

[18] achieved 19,000 s LHCD discharge. Drawback of the LHCD scheme is related to density limit and too strong electron Landau damping in high temperature plasmas. It was reported that current drive efficiency declined drastically in high density plasmas deviating from n_e^{-1} scaling [19]. Too efficient absorption of LHW will also be severe problem in high temperature reactor plasmas preventing wave penetration to core region and dissipating available heating power in edge region.

1.4.2. Lower Hybrid Fast Wave (LHFW)

Density limit for propagation and strong electron Landau damping for absorption of the slow wave make it hard to penetrate into the core plasma region in reactor-grade plasmas. Thus, alternative central or off-axis current drive method should be explored for high density and high temperature plasmas. Fast wave in LHW range has less favorable polarization (E_z) for the electron Landau damping than that of the slow wave, but it is still non-negligible and could be good candidate for the current drive scheme of reactor-grade plasmas. Especially, the fast wave branch in frequency range higher than $2\omega_{lh}$ has been proposed and it is called as Lower Hybrid Fast Wave (LHFW) [20, 21]. LHFW is known to have advantages of high E_z component and of avoiding parametric instability in rather higher frequency range than other fast waves such as High Harmonic Fast Wave (HHFW) [22] and Helicons [23] with lower ion cyclotron harmonic numbers as shown in Figure 1.6. In fact, fast wave current drive experiment in similar frequency range ($\omega \sim \omega_{lh}$) was attempted in PLT [24]. The results had no difference with the slow wave experiments due to poor absorption of the fast wave and mode conversion into slow wave. LHFW in higher frequency ($\omega > 2\omega_{lh}$) has higher E_z component than that of the fast wave in PLT and more strong Landau damping is expected.

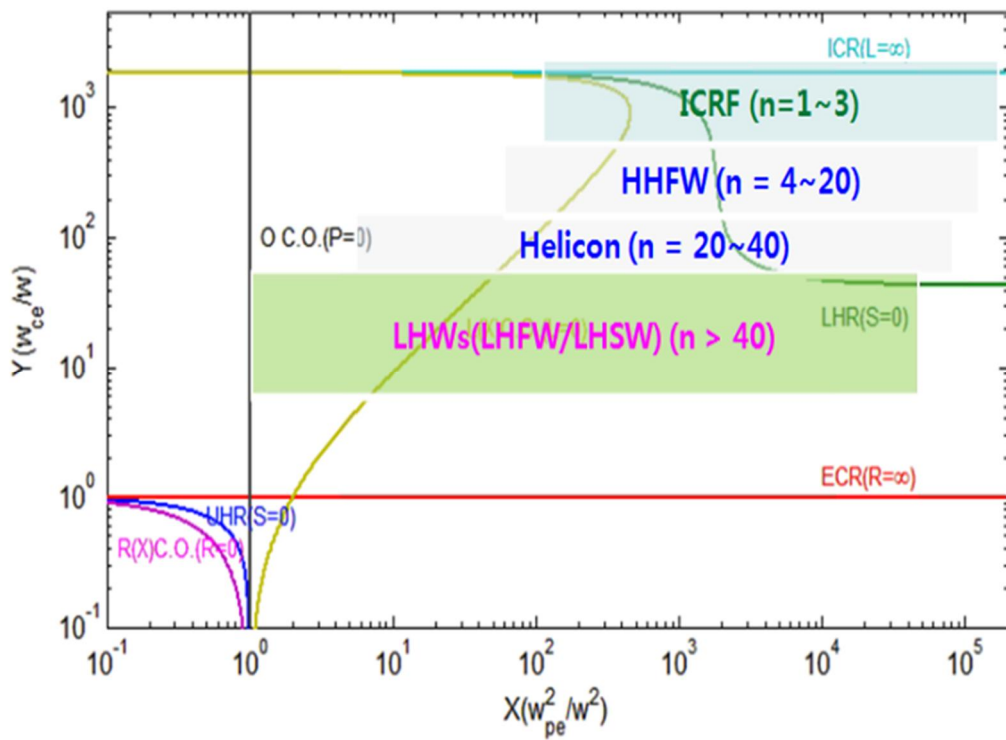


Figure 1.6 Fast waves for heating and current drive in fusion device (n : ion cyclotron harmonic number) [21].

1.4.3. Spectral Gap Problem

LHCD has been successfully utilized for the non-inductive current drive method in tokamak experiment and well understood by theory and various numerical codes. However, there is still unsolved issue about a gap in parallel refractive index n_{\parallel} between $n_{\parallel 0}$ determined by antenna and $n_{\parallel LD} (\equiv c/4v_T)$ described as strong Landau damping condition on a Maxwellian distribution. It is so called spectral gap ($n_{\parallel 0} < n_{\parallel} < n_{\parallel LD}$) problem in LHCD [25, 26, 27, 28]. Figure 1.7 shows regime for n_{\parallel} of several previous LHCD experiments and ITER plan. Absorption of lower hybrid waves and current drive have been successfully achieved despite of presence of the spectral gap. ITER will be the sole exception that has no spectral gap. It is assumed that n_{\parallel} is upshifted during propagation to bridge the gap for absorption. Explanations have been attempted to bridge the gap by geometrical effects of poloidal and toroidal magnetic field [29, 30] and certain edge physics such as parametric decay instability [31, 32, 33] and wave scattering by density fluctuation [34, 35, 36, 37]. Spectral gap is conventionally studied in perspective of absorption. However, n_{\parallel} determines not only absorption condition but also accessibility condition for propagation, as the property is analyzed in several theoretical and ray tracing research [36, 37]. It is believed that n_{\parallel} -upshift in plasma affects accessibility condition for lower hybrid waves, but experimental observation is rarely reported.

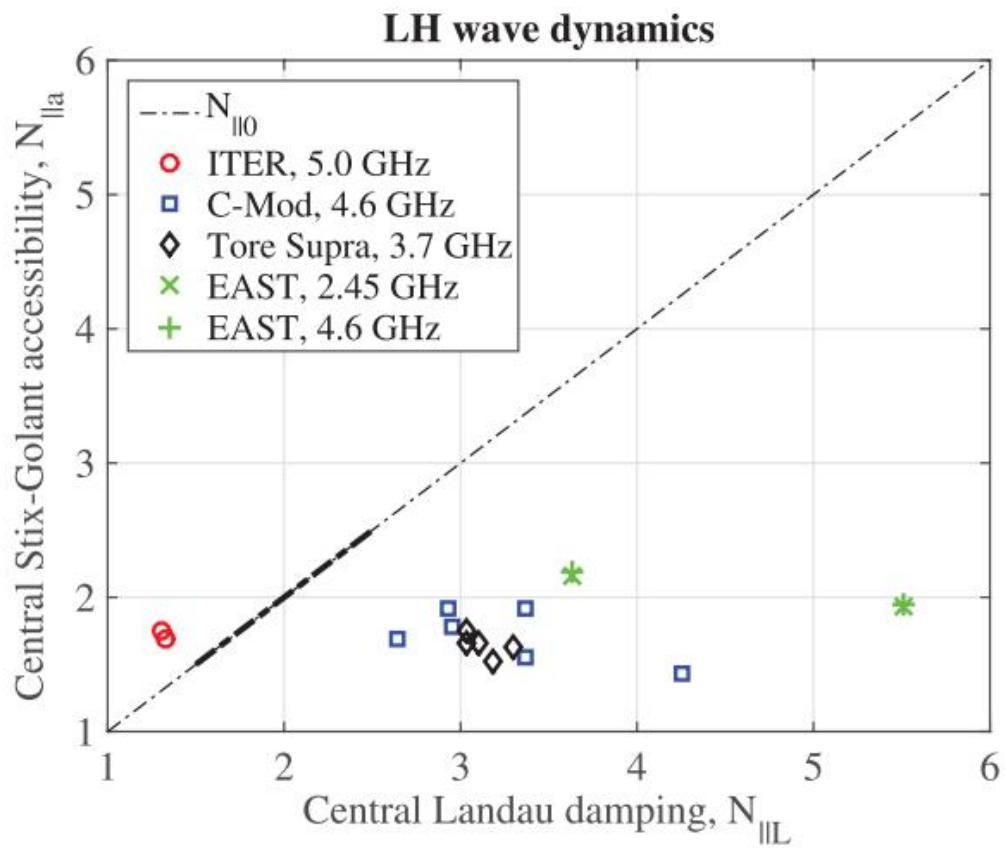


Figure 1.7 Parallel refractive indexes of tokamak devices [28].

1.5. Objective of Research

The chief objective of this study is the investigation on coupling and propagation of LHFW. The cutoff density for the LHFW launching is usually several hundred times more than that of the LHSW. And rather higher frequency of LHFW for high E_z than the other fast waves causes narrow coupling window. Therefore, the coupling issues including both physical and technical point of view will be a key factor for the feasibility of the LHFW. Accessibility conditions also can be significantly modified from the linear theory by n_{\parallel} -upshift in plasma. Intensive investigation on coupling and propagation is an essential starting point of the proof-of-principle of LHFW scheme for current drive.

There are three major works in this study. First, coupling characteristics are analyzed with antenna-plasma simulations and preliminary experiments in Versatile Experiment Spherical Torus (VEST). Coupling simulation is carried out using the COMSOL Multiphysics to predict precisely coupling efficiency and coupled power ratio of fast and slow waves in view of the linear theory. Second, RF conditioning of the antenna is conducted to maximize the coupling power mitigating dissipated power at the surface of the current straps in the antenna. It contributes to efficient and reliable power coupling from antenna to plasma in view of the technical issue. Third, fast wave coupling experiments are carried out with wave measurements using magnetic probe array in VEST. Especially, coupling experiments are conducted in the marginal ($n_e \geq n_{confluence}$) and prohibited ($n_e \gg n_{confluence}$) regime for the fast wave coupling to investigate the modified accessibility condition. The results of experiments are surprisingly modified propagation path with more radial penetration and expanded coupling regime in high density plasmas with the aid of n_{\parallel} -upshift via wave scattering contrary to the predictions by linear theory.

Chapter 2. Lower Hybrid Fast Wave (LHFV)

2.1. Dispersion Relation

Frequency range of LHFV is $2\omega_{lh} < \omega \ll \omega_{ce}$. Fast waves at these high frequencies tend to propagate nearly along the magnetic field lines [38]. Propagation of the LHW is given by the real part of the perpendicular refractive index derived from cold plasma dispersion relation as follows:

$$n_{\perp r,F} \cong \left[-\frac{(n_{\parallel}^2 - R)(n_{\parallel}^2 - L)}{n_{\parallel}^2 - S} \right]^{1/2}, n_{\perp r,S} \cong \left[-\frac{P(n_{\parallel}^2 - S)}{S} \right]^{1/2} \quad (2.1)$$

where n_{\parallel} is a parallel refractive index and S, P, R and L are Stix parameters ($S = 1 - \sum_{\alpha} \frac{\omega_{p\alpha}^2}{\omega^2 - \Omega_{c\alpha}^2}$, $P = 1 - \sum_{\alpha} \frac{\omega_{p\alpha}^2}{\omega^2}$, $R = 1 - \sum_{\alpha} \frac{\omega_{p\alpha}^2}{\omega^2} \frac{\omega}{\omega + \Omega_{c\alpha}}$, $L = 1 - \sum_{\alpha} \frac{\omega_{p\alpha}^2}{\omega^2} \frac{\omega}{\omega - \Omega_{c\alpha}}$, α : species (ion or electron)). Figure 2.1 shows contour plots of perpendicular refractive index in CMA diagram. Propagating region of waves is much broad for the slow wave. It is more helpful to discuss the perpendicular refractive index as a function of density as presented in Figure 2.2.

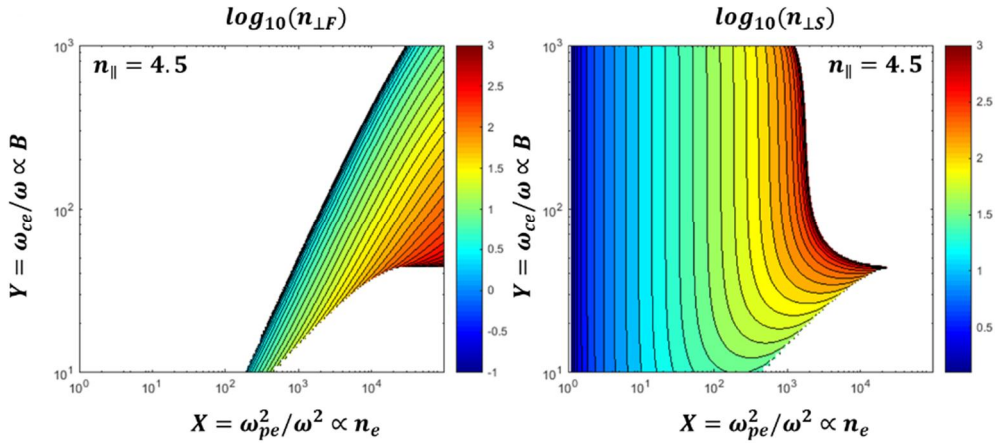


Figure 2.1 Perpendicular refractive indexes of the fast and slow wave in CMA diagram.

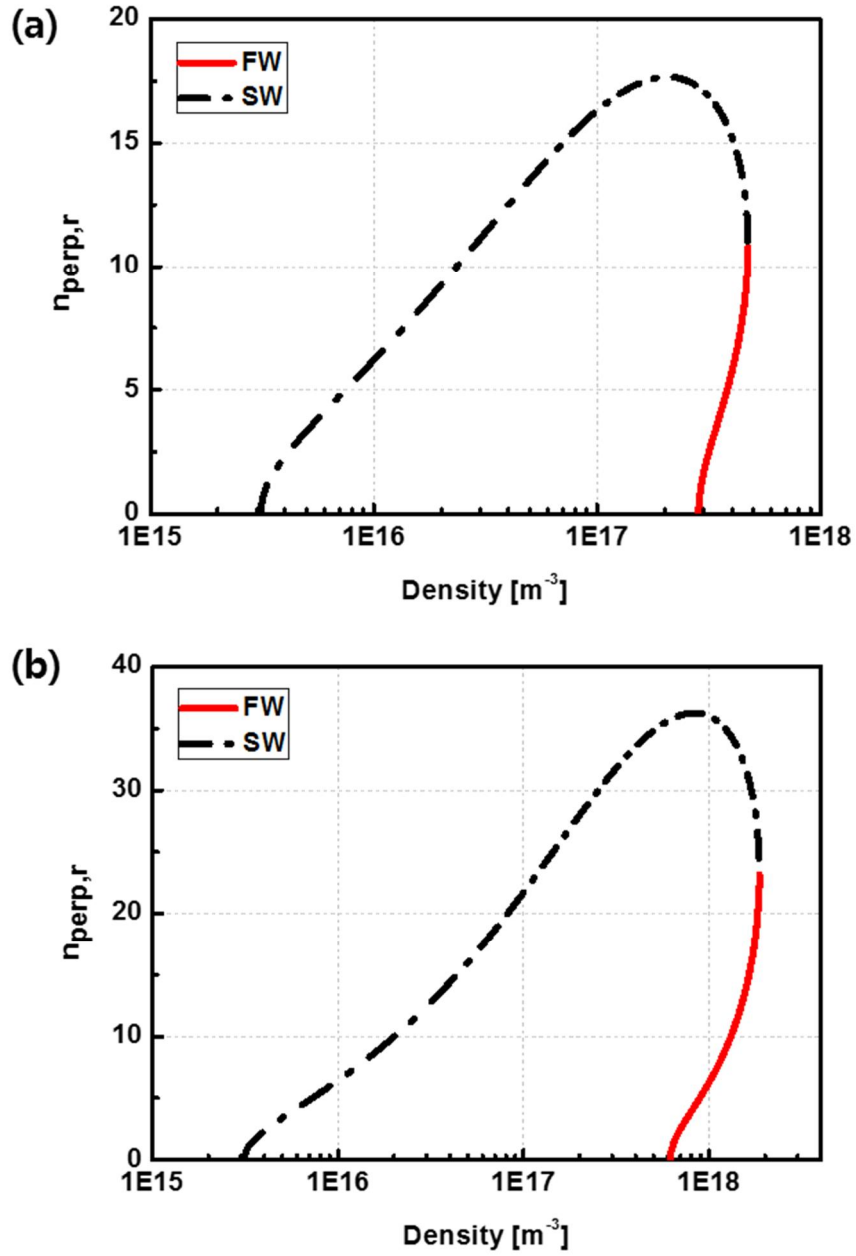


Figure 2.2 Real part of the perpendicular index of the fast and slow wave as a function of plasma density when (a) $B_0 = 0.1 \text{ T}$ and (b) $B_0 = 0.2 \text{ T}$.

Waves can propagate when the perpendicular refractive index is larger than 0 and cutoff density for launching the fast wave (order of 10^{17}m^{-3}) is about a hundred times higher than that of the slow wave (order of 10^{15}m^{-3}). When the quadratic equation for the perpendicular refractive index has equal root, the solution is same for the fast and slow wave and it is called confluence where both slow and fast waves are merged and propagate backwards with the same accessibility condition. Accessibility condition for the fast wave coupling can be described with the plasma density as $n_{cutoff,fast} < n_e < n_{confluence}$. Cutoff density and confluence density can be approximately expressed as follows:

$$n_{cutoff,slow} \cong \frac{m_e \epsilon_0}{e^2} \omega^2 \propto \omega^2 \quad (2.2)$$

$$n_{cutoff,fast} \cong \frac{m_e \epsilon_0}{e^2} (n_{\parallel}^2 - 1) \omega \omega_{ce} \propto n_{\parallel}^2 \omega B \quad (2.3)$$

$$n_{confluence} \cong \frac{1}{4} \frac{m_e \epsilon_0}{e^2} n_{\parallel}^2 \omega_{ce}^2 \propto n_{\parallel}^2 B^2 \quad (2.4)$$

Note that cutoff density for slow wave in equation (2.2) is only a function of wave frequency regardless of magnetic field strength and parallel refractive index prescribed by the antenna while cutoff density for fast wave in equation (2.3) is linearly proportional to wave frequency and magnetic field strength. Confluence density in equation (2.4) is proportional to square of magnetic field strength. When the toroidal magnetic field strength of device increases, cutoff density for the fast wave increases linearly and coupling window is widened by increase of confluence density faster than the cutoff density as shown in Figure 2.2 (b). Also, since wave frequency of LHF_W is rather higher than the other fast waves as discussed in section 1.4.2, coupling window is narrow compared to the other fast waves as well as LHSW.

Absorption of the LHW is given by imaginary part of the perpendicular refractive index derived from the warm plasma dispersion relation as follows [20, 21];

$$n_{\perp i, F} \cong n_{\perp r, F} \frac{\pi^{1/2} \eta^3 \exp(-\eta^2)}{\frac{\omega_{ce}^2 n_{\parallel}^2}{\omega_{pe}^2} - 1}, n_{\perp i, S} \cong n_{\perp r, S} \pi^{1/2} \eta^3 \exp(-\eta^2) \quad (2.5)$$

where η is the ratio of wave phase velocity to electron thermal velocity. Generally, absorption of the slow wave is mainly a function of electron temperature while absorption of the fast wave is roughly proportional to electron beta including electron density. Strong absorption of HHFW and helicons in high beta plasmas were calculated from analytic [22] and GENRAY [23] study.

2.2. Coupling and Absorption of LHF in ST

For the proof-of-principle, ST device has advantages in view of the fast wave coupling and absorption. Cutoff density for the fast wave is moderated with low magnetic field strength of ST compared to that of conventional tokamak. At least cutoff density in ST is one order lower than that of conventional tokamak. Absorption by Landau damping of the fast wave is much weaker than that of wave as noted in section 1.4. It is the reason that the fast wave could be a good candidate for reactor grade plasmas in future but experiments for proof-of-principle might be difficult in present plasmas. Equation (2.5) implies that the damping rate of fast wave is strong in high beta plasmas. Generally, imaginary part of the perpendicular refractive index of fast wave is two orders lower than that of the slow wave. From the equation (2.5), relative fraction of imaginary part of the perpendicular refractive indexes can be obtained as $\frac{n_{\perp i, F}}{n_{\perp i, S}} \cong \frac{n_{\perp r, F}}{n_{\perp r, S}} \cdot \frac{1}{\omega_{ce}^2 n_{\parallel}^2 / \omega_{pe}^2 - 1}$.

With the plasma dielectric constant, $\epsilon \equiv \left(\frac{\omega_{pe}}{\Omega_{ce}}\right)^2 \propto \frac{\beta_e}{T_e}$, absolute value of the fraction is

expressed by $\left| \frac{1}{\omega_{ce}^2 n_{\parallel}^2 / \omega_{pe}^2 - 1} \right| \propto \left| \frac{\epsilon}{n_{\parallel}^2 - \epsilon} \right|$. It can be easily shown that absorption of the fast wave can be comparable to that of the slow wave for large ϵ plasmas, i.e. ST plasmas. Usually conventional tokamaks have $\epsilon \sim 1$ and STs have $\epsilon \sim 50-100$ [22]. The ratio $\left| \frac{\epsilon}{n_{\parallel}^2 - \epsilon} \right|$ can be scaled to order of 1/10 for a small ϵ and order of 1 for a large ϵ indicating efficient absorption of the fast wave in STs. For VEST, using the parameters $B_0 = 0.1$ T and $n_0 = 5 \times 10^{18} \text{ m}^{-3}$, $\epsilon \sim 51$. Figure 2.3 shows calculation of $\frac{n_{\perp,i,F}}{n_{\perp,i,S}}$ as a function of density with the VEST parameters. Imaginary part of the perpendicular refractive index of the fast wave is approximately approaching to about 30 % compared to that of the slow wave as plasma density increases. Accordingly, STs with characteristics of low magnetic field strength and high beta plasma are able to make favorable conditions for the study of LFW coupling and absorption.

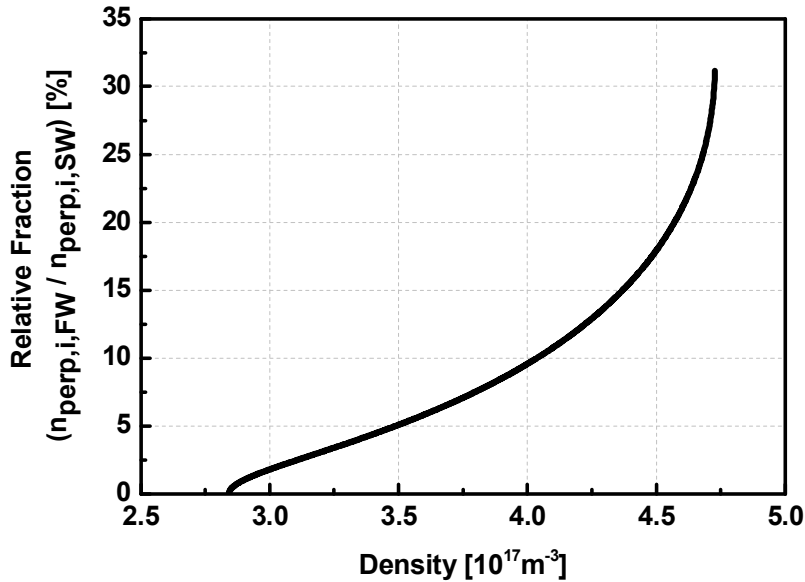


Figure 2.3 Ratio between imaginary part of the refractive index of the fast and slow wave as a function of plasma density.

Chapter 3. Experimental Setup

3.1. RF System

RF system for the LHFV experiment consists of comb-line antenna, directional couplers, coaxial transmission lines, circulator, dummy load and klystron power system. Development of the antenna and klystron power system is accomplished by collaboration with Korea Atomic Energy Research Institute (KAERI) and Kwangwoon University. Comb-line antenna to launch the fast wave polarization has frequency range from 468 MHz to 506 MHz and consequently $n_{\parallel 0}$ is varied from 3 to 4.7. Comb-line antenna is installed through two ports and located at $R = 0.745$ m and $Z = 0$ m with tungsten limiters at $R = 0.74$ m. Klystron and comb-line antenna have been commissioned up to 10 kW of injected power at 500 MHz.

3.1.1. Comb-line Antenna

A comb-line antenna has been commonly used to excite the fast wave in plasmas [39, 40, 41, 42, 43, 44]. Moeller [39] proposed to use the comb-line filter structure as a fast-wave antenna. Comb-line filter was commercially available bandpass filter. Comb-line antenna consists of quarter-wavelength resonant straps, which is inductively coupled to each other, and Faraday shield to eliminate electrostatic coupling between the current straps and plasmas. Figure 3.1 shows a picture of comb-line antenna made by General Atomics (GA) for JFT-2M [42] experiment and Figure 3.2 shows equivalent circuit for the comb-line antenna. Waves are radiated into plasmas between mutual inductive couplings of each current straps. Most remarkable advantage of the comb-line antenna as a travelling wave antenna (TWA) is intrinsic good impedance matching without additional matching system like tuner. If resistive impedance is much smaller than mutual reactance ($R \ll \omega M$), the input impedance is nearly independent of resistive

loading as follows [41]:

$$Z_{in} = \frac{V_{in}}{I_{in}} = \omega M \left[1 - \frac{1}{8} \left(\frac{R}{\omega M} \right)^2 + \dots \right] \quad (3.1)$$

It means that coupling and reflection of fast wave are almost independent of time varying plasma loading. It is suitable for dynamic environments such as pulsed operation plasma discharge.

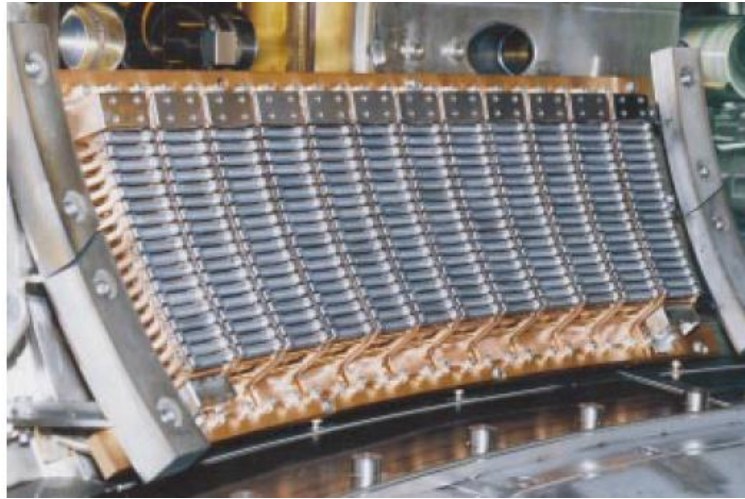


Figure 3.1 Picture of a comb-line antenna designed and built by GA and installed on JFT-2M [42].

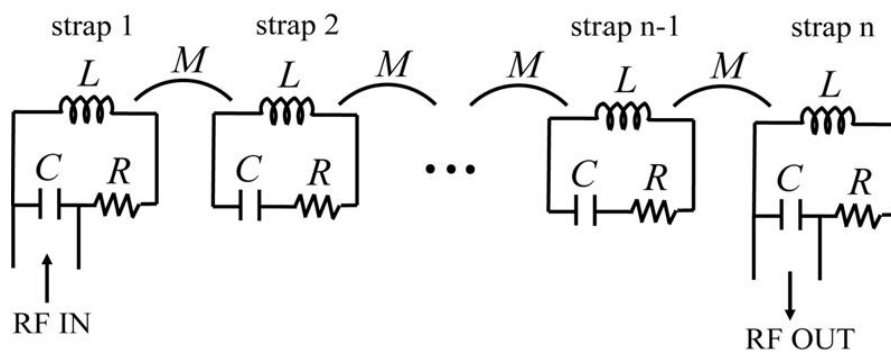


Figure 3.2 Equivalent circuit of the comb-line antenna [44].

A comb-line antenna is designed and fabricated by Kwangwoon University for VEST benchmarking the precedent antenna. The proposed antenna is composed of copper to reduce ohmic loss. It consists of two tapered coaxial cables, two exciting straps of the folded-monopole structure, 12 radiating straps, 11 field isolators, and the Faraday shield [45]. Figure 3.3 presents fabricated comb-line antenna and installation of the antenna in VEST device. Figure 3.4 shows peak value of parallel refractive index, $n_{||0}$, at available frequency range of the antenna.

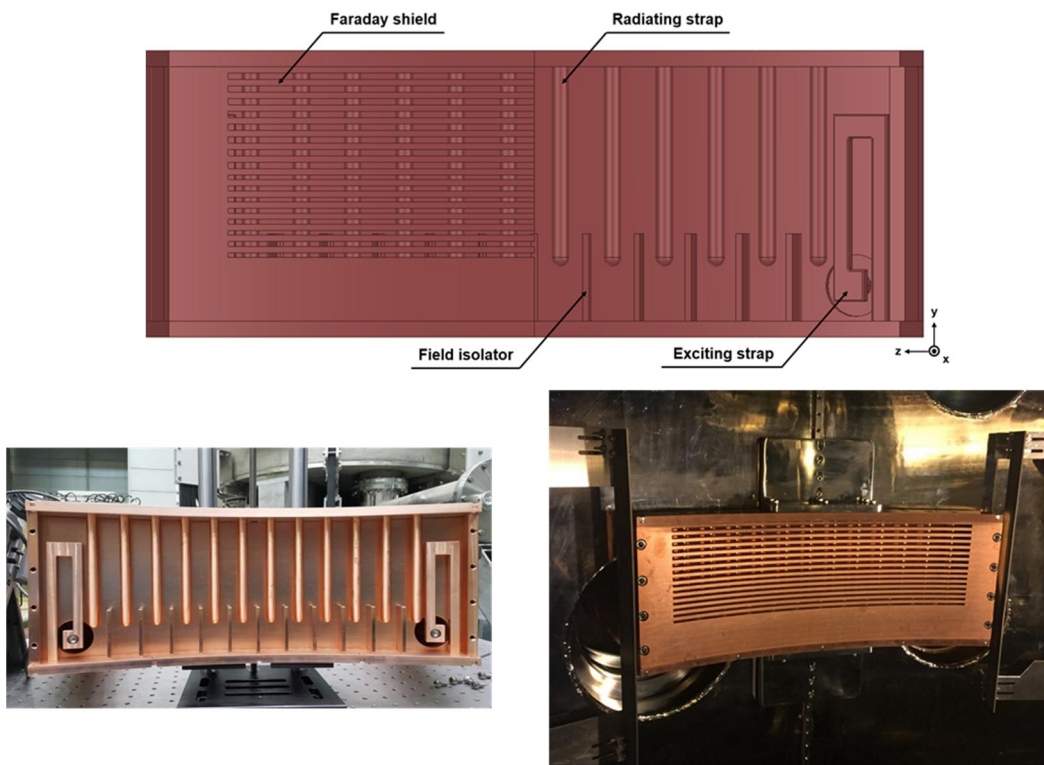


Figure 3.3 A comb-line antenna fabricated and installed in VEST chamber.

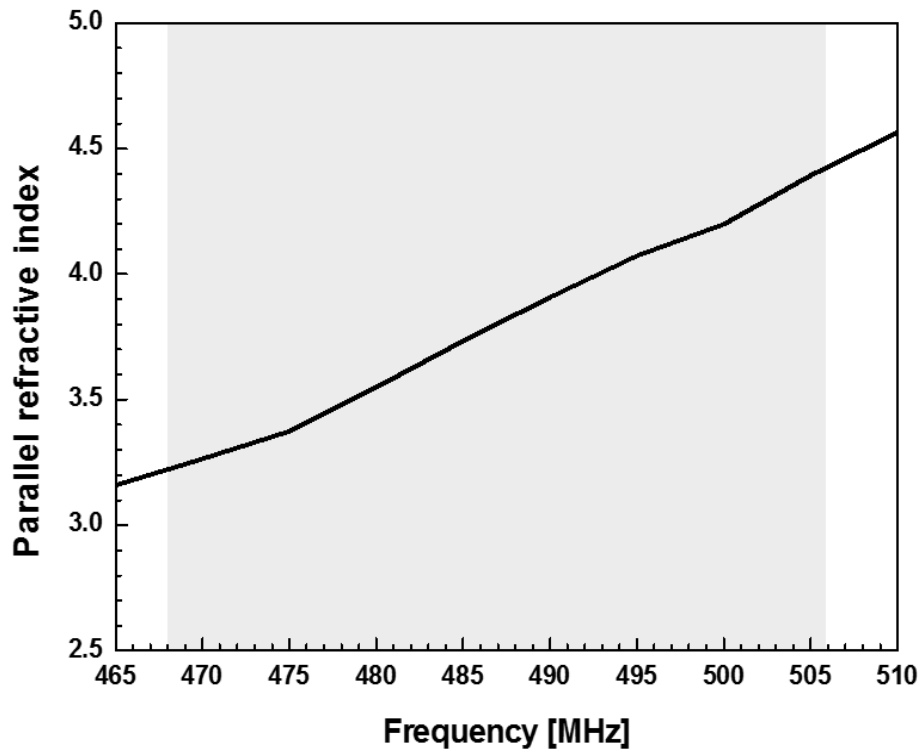


Figure 3.4 $n_{\parallel 0}$ of designed comb-line antenna.

S-parameters of the combline antenna are measured by using network analyzer as shown in Figure 3.5 to check the coupling characteristics of the antenna installed in VEST before RF injection test. RF experiment is mainly conducted at the frequency of 500 MHz, which shows 83% of transmission and 7% of reflection coefficients. Sum of the coefficients is 90% indicating that the dissipation is about 10%. The dissipation in this measurement can be regarded as radiation loss by neglecting resistive loss at copper current straps of the antenna since outgassing does not take place for low power experiments with network analyzer. Detailed description about outgassing rate and RF conditioning is presented in appendix.

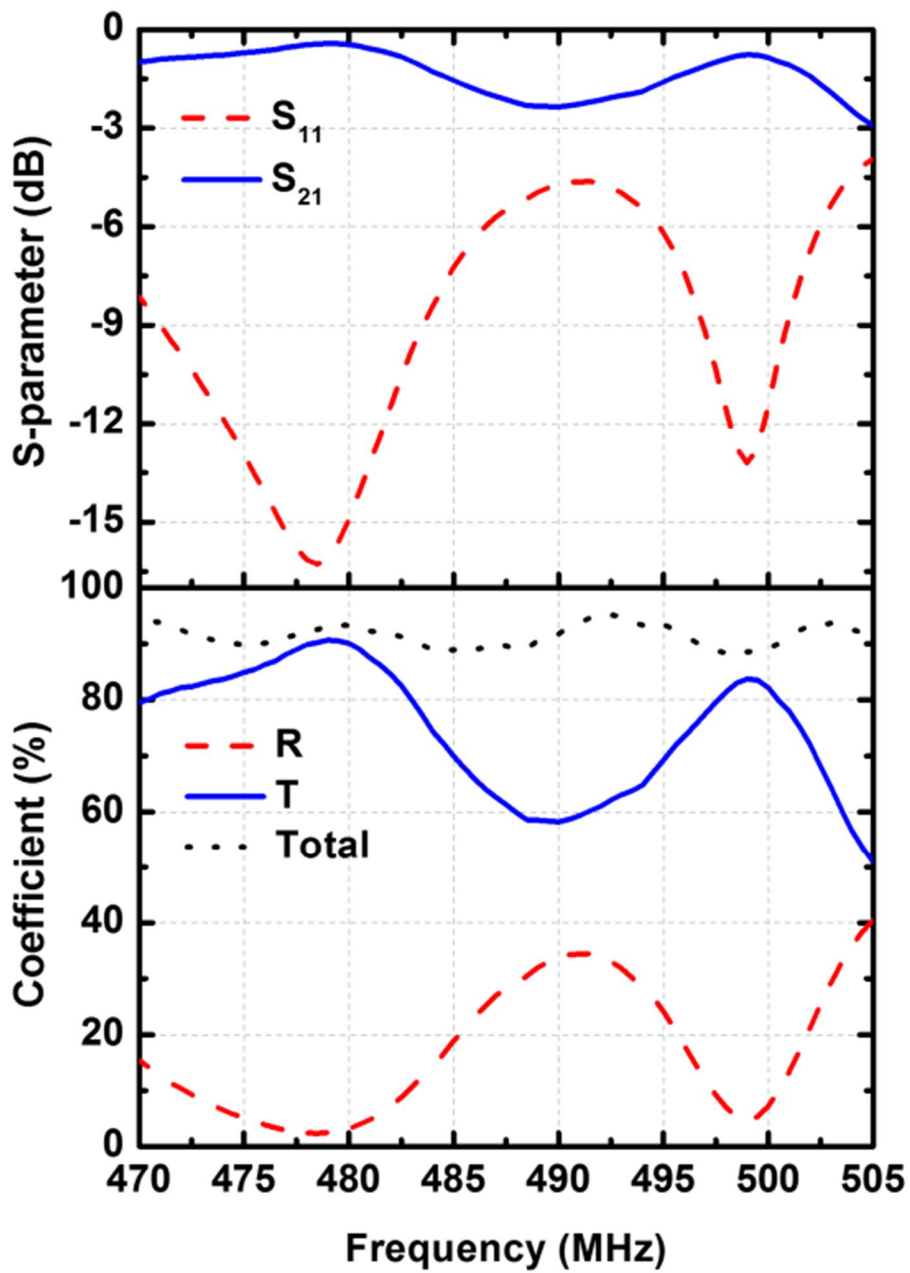


Figure 3.5 S-parameters (S_{11} , S_{21}) and coefficients (R, T, and R+T) of combline antenna installed in VEST [46].

3.1.2. Klystron System

Klystron system is designed based on an old 10kW UHF broadcasting system at Seoul National University (SNU) by KAERI [20]. Figure 3.6 shows schematic diagram of LHFV RF system. Input signal amplified by solid state amplifier (SSA, HM0225-05A, RFHIC) is applied to klystron and output RF power is transmitted through coaxial transmission line (line loss < 5 %) to comb-line antenna. Figure 3.7 shows pictures of klystron, high voltage power supply, circulator, transmission line and dummy load. Frequency response of the klystron is measured using the frequency sweep function of network analyzer. Maximum power is amplified at central frequency of 498 MHz as shown in Figure 3.8. First RF injection is conducted into dummy load through connected transmission lines and the antenna. Figure 3.9 presents stable operation without severe reflection up to 7 kW of injected RF power. Klystron system is synchronized with control and DAQ system of VEST device using LABVIEW. Figure 3.10 shows operation procedures for RF experiment in VEST. VEST trigger 1 turns on high voltage power supply for 7 s. And then DC relay switch to bias high voltage and RF generator to apply input signal to klystron are automatically turned on by LABVIEW programming. VEST trigger 2 activates function generator that connects RF generator with klystron through frequency mixer at desired timing for RF injection. Function generator determines pulse length of RF injection by preset pulse length of waveform.

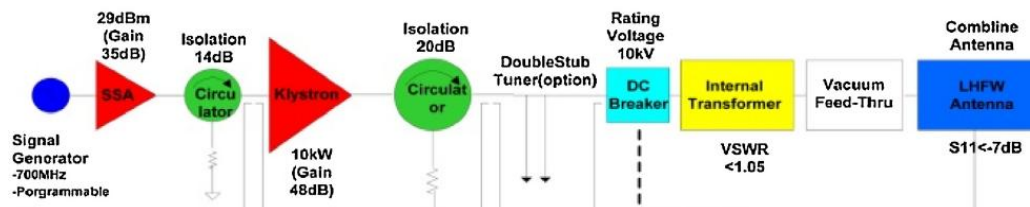


Figure 3.6 Schematic diagram of RF system [20].



Figure 3.7 Pictures of LHFV RF system (klystron, high voltage DC power supply, transmission line and dummy load) installed in VEST device.

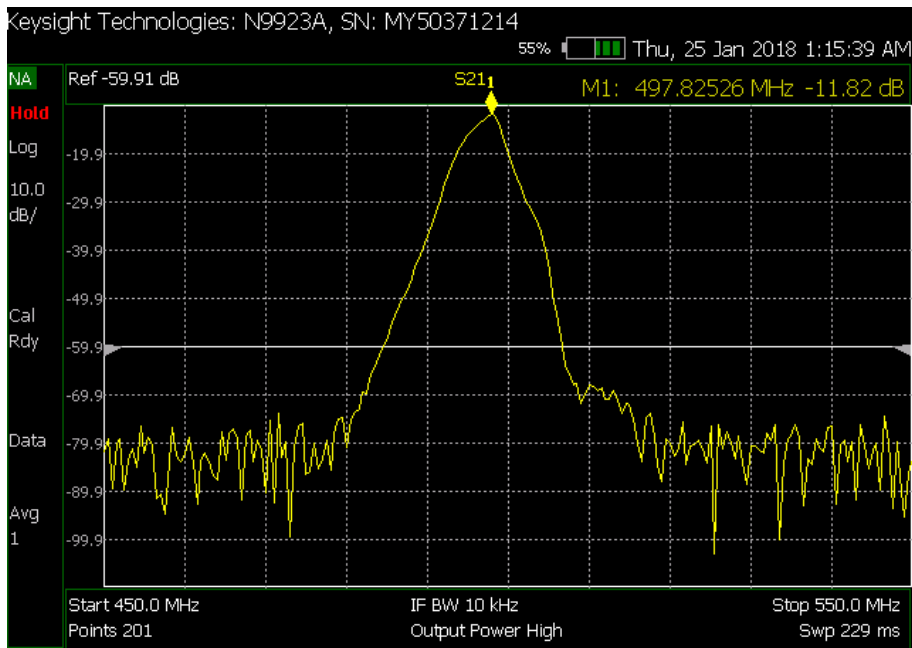


Figure 3.8 Frequency response of klystron.

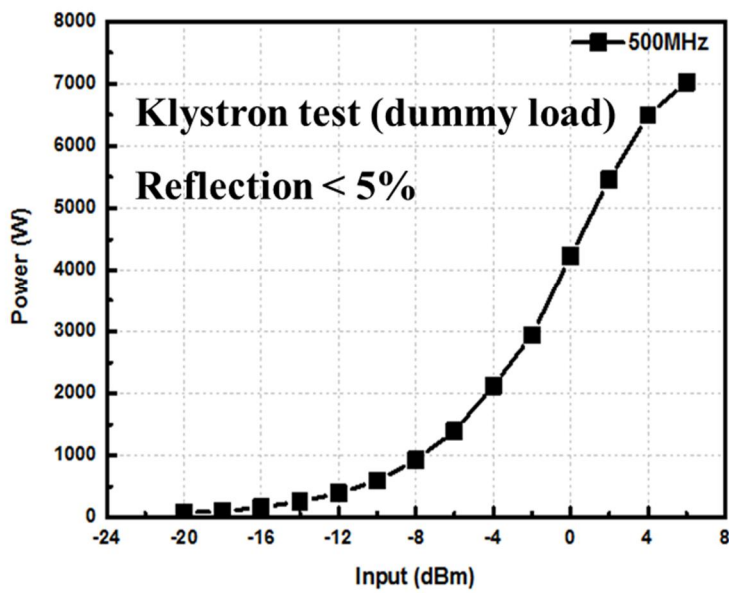


Figure 3.9 RF injection into dummy load for klystron test.

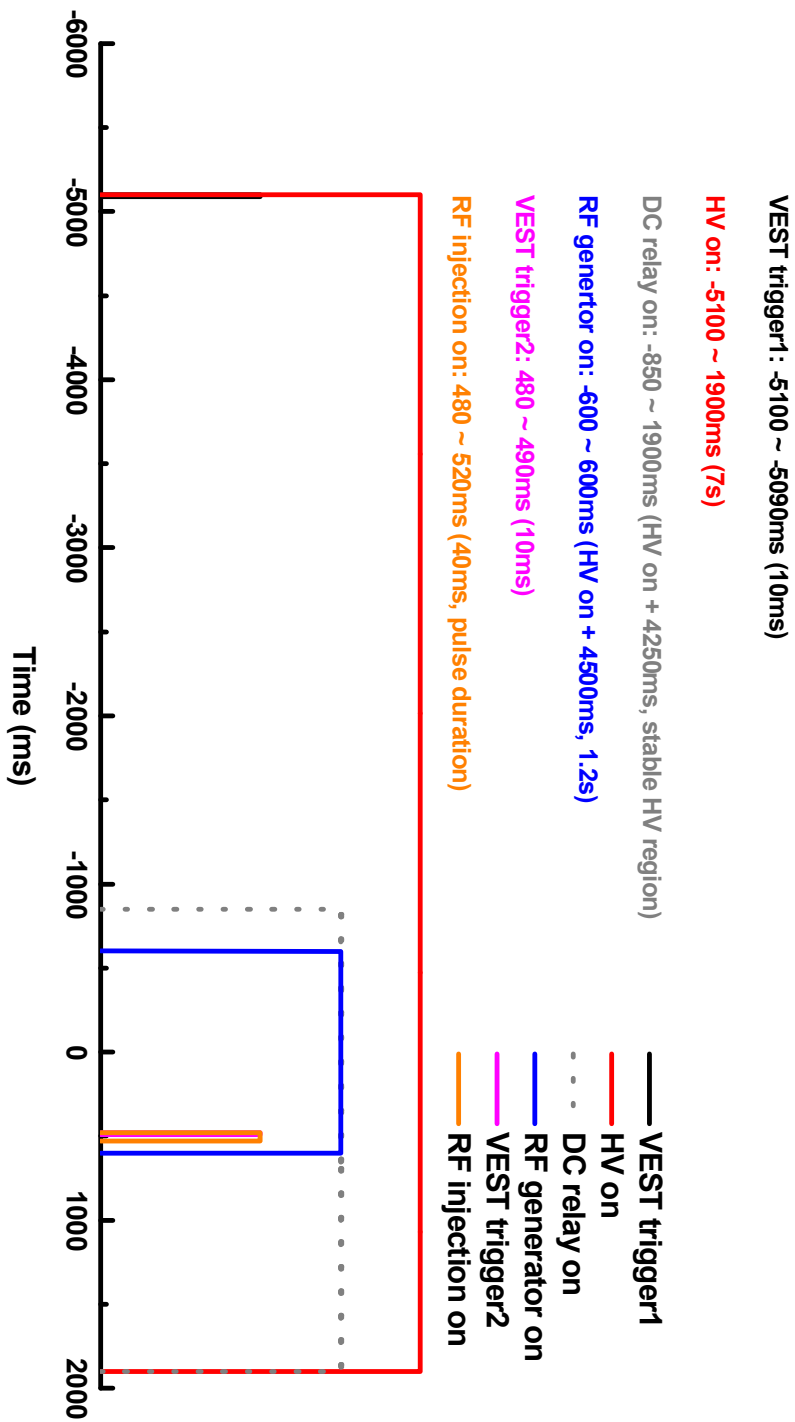


Figure 3.10 Operation procedures of RF system for VEST experiment.

3.2. Diagnostics

Diagnostics for the LHFV experiment consist of RF diagnostics, Langmuir probe and magnetic probe array. RF diagnostics measures coupling and reflection power of injected RF by directional couplers positioned in front of the antenna ports. Langmuir triple probe and single probe measure time varying electron density, temperature and ion saturation current in scrape off layer (SOL) region. Magnetic probe array measures power spectrum and parallel refractive index of LHFV in plasma.

3.2.1. RF Diagnostics

Directional couplers to measure RF power and coefficients of transmission, reflection and coupling are positioned in front of the antenna ports as depicted in Figure 3.11. Input and output ports of the antenna are connected to a klystron system and dummy load respectively through the coaxial transmission lines. Directional couplers detect injected power (P_{in}) and reflected power (P_r) at the input port and transmitted power (P_t) to dummy load at the output port. Transmission coefficient, $T = P_t / P_{in}$, and reflection coefficient, $R = P_r / P_{in}$, are directly calculated from voltage measurements at the directional couplers. Remainder power fraction, $100-(R+T)$ [%], can be regarded as dissipation in the antenna in case of vacuum operation as discussed in appendix and can be regarded as coupling efficiency in case of plasma discharges.

Power detector and phase detector (ZX47-50LN+, AD8302) are prepared to convert high frequency signals of RF power and phase difference into DC signals. Calibrations are conducted with known RF power and phase difference using RF signal generator at 500 MHz as presented in Figure 3.12.

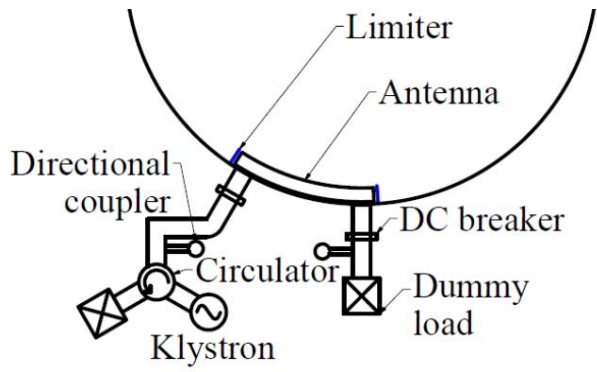


Figure 3.11 Schematic diagram of RF system with VEST chamber.

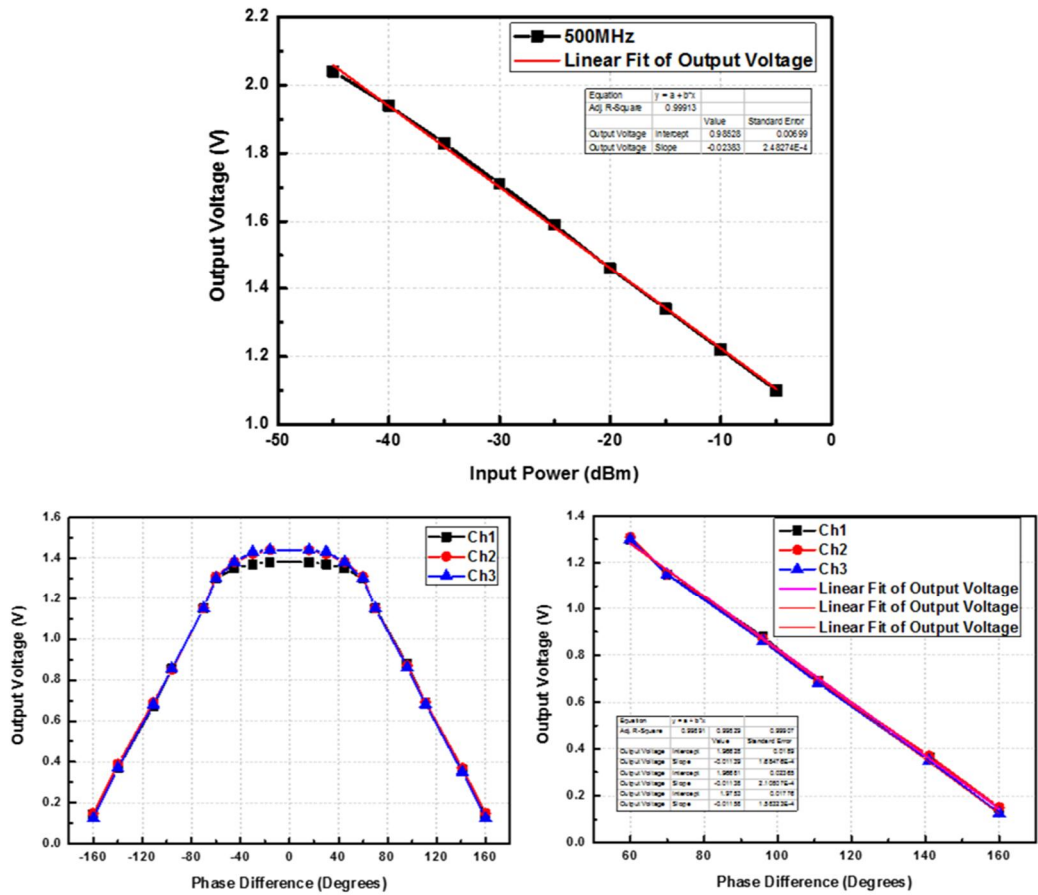


Figure 3.12 Calibration results of power detector and phase detector at 500 MHz.

3.2.2. Langmuir Probe [47]

Triple probe can diagnose the time varying electron density and temperature during discharges. It was well developed in reference [48] and basic principles of the scheme is briefly summarized in this section. The triple probe consists of three tips at different potentials. Figure 3.13 (a) shows the schematic diagram of the potential at three tips. The triple probe is combination of floating probe and double probe. Figure 3.13 (b) shows the schematic diagram of the triple probe circuit. The potential difference and current between each tip is measured using the isolation amplifier AD210AN. The relation of the currents and potentials can be expressed as follows;

$$\begin{aligned} 0 &= SJ_i(V_f) - SJ_e \exp(-\phi V_f) \\ -I &= SJ_i(V_+) - SJ_e \exp(-\phi V_+) \\ I &= SJ_i(V_-) - SJ_e \exp(-\phi V_-) \end{aligned} \quad (3.2)$$

where S is surface area of the probe tips, J_e is the electron saturation current, J_i is the ion saturation current and $\phi \equiv e/kT_e$. If the variation of the ion saturation current is negligible compared with that of the electron current, the ion saturation current is given as follows;

$$J_i(V_f) = J_i(V_+) = J_i(V_-) = J_i \quad (3.3)$$

Then, equation (3.2) and (3.3) yield;

$$\frac{1 - \exp(-\phi V_{d2})}{1 - \exp(-\phi V_{d3})} = \frac{1}{2} \quad (3.4)$$

where $V_{d2} = V_+ - V_f$ and $V_{d3} = V_+ - V_-$. The electron temperature can be obtained from the equation (3.4) by iteration. The elimination of the electron saturation current from the equation (3.2) and equation (3.4) leads to;

$$J_i = \frac{I}{S} [\exp(\phi V_{d2}) - 1] \quad (3.5)$$

and ion saturation current is given by;

$$J_i = \frac{S'}{S} J_{is} \cong J_{is} = en_{is} v_{is} = en_e \exp\left(-\frac{1}{2}\right) \cdot \left(\frac{kT_e}{m_i}\right)^{\frac{1}{2}} \quad (3.6)$$

The equation (3.5) and (3.6) gives the electron density as follows;

$$n_e = \left(\frac{(m_i)^{\frac{1}{2}}}{S} I\right) \cdot \frac{\exp\left(\frac{1}{2}\right)}{e(kT_e)^{\frac{1}{2}} [\exp(\phi V_{d2}) - 1]} \quad (3.7)$$

The electron temperature and density is given from the equation (3.4) and (3.7). V_{d2} and I is measured quantity and V_{d3} is a bias voltage that can be controlled. V_{d2} determines the electron temperature and then the electron density can be calculated from I and the electron temperature. Figure 3.14 is a picture of fabricated triple probe which consists of tungsten wire for probe tips and alumina tube for electrical insulation. Triple probe is mounted on linear guide to scan radial profile of electron density and temperature. Ion saturation current can be measured using the floating tip of the triple probe with sufficient high bias voltage of negative potential to prevent entrance of high energy electrons.

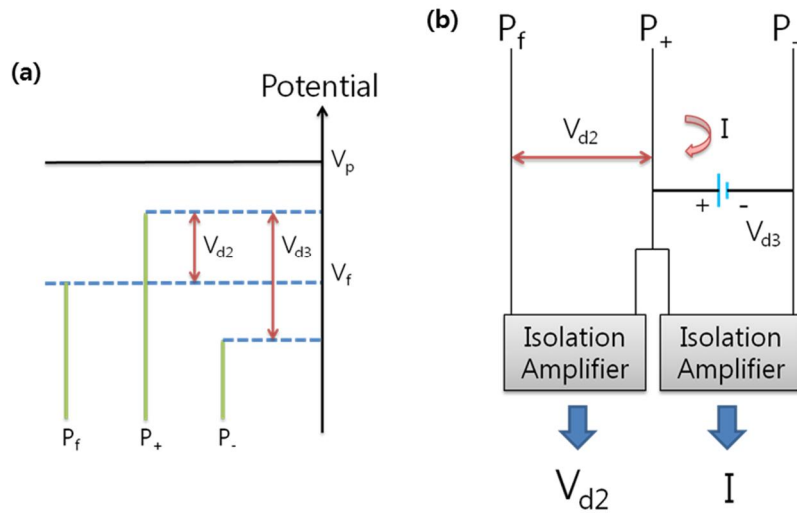


Figure 3.13 Schematic diagram of (a) potential at each tips and (b) measurement circuit of

triple probe.



Figure 3.14 Fabricated triple probe.

3.2.3. Magnetic Probe Array

Magnetic probes are designed and fabricated with references of precedent researches [49, 50, 51] to measure power spectrum and refractive indexes (n_{\parallel} & n_{\perp}) of B_{ϕ} and B_y fields separately at outboard. Figure 3.15 shows two magnetic probe arrays (MP1 & MP2) which consist of one turn loop coil ($D = 8$ mm) orthogonal to a thin linear slit (10×1 mm), a half inch SUS tube and an alumina tube. Six magnetic probes are arranged by two rows and three columns of coils. Those are separated by 2 cm in toroidal direction in order to measure parallel wavenumber. The slits of upper and lower array are orthogonally configured in order to measure B_{ϕ} and B_y fields respectively. COMSOL simulations are conducted to check the effect of slit with WR1800 waveguide geometry and TE10 mode wave as illustrated in Figure 3.16 (a). Figure 3.16 (b) presents simulation results that the slit allows the parallel magnetic field to penetrate into coil with attenuation of about 40 % and rejects almost completely the perpendicular polarization.

One turn loop coils are tested with Helmholtz coil before installation in the VEST chamber to check linearity between measured voltages and known magnetic field strength at 500 MHz as shown in Figure 3.17. Signal amplitude is higher than 10 mV with magnetic field strength higher than 0.02 G.

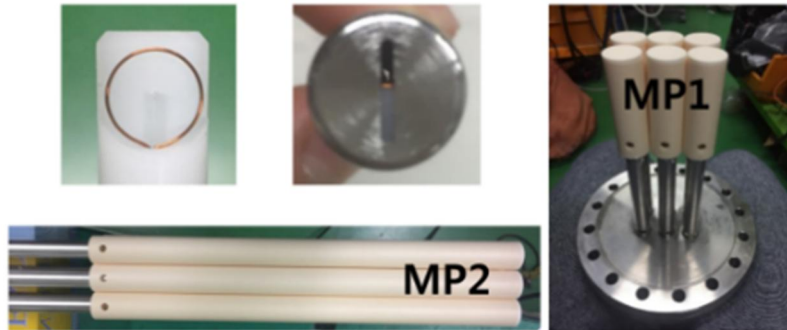


Figure 3.15 Pictures of fabricated magnetic probes.

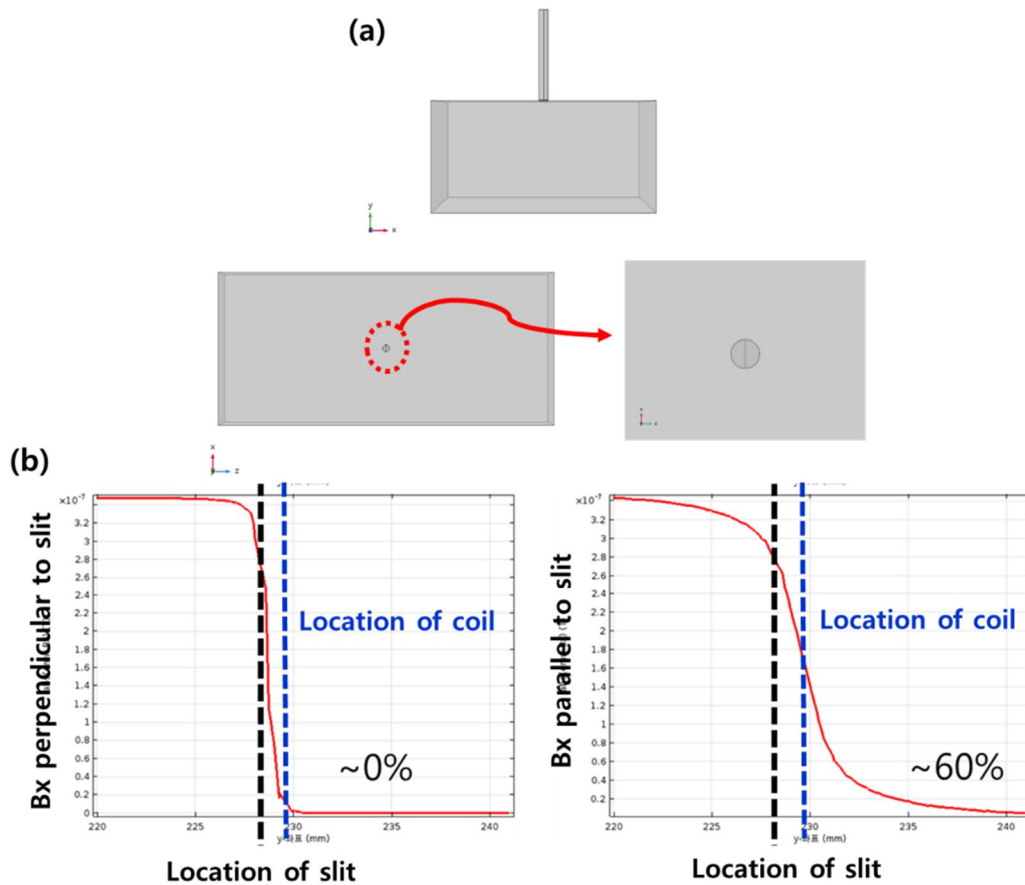


Figure 3.16 COMSOL simulation to verify slit effect for separating orthogonal polarization of magnetic fields. (a) Simulation domain and (b) Simulation results.

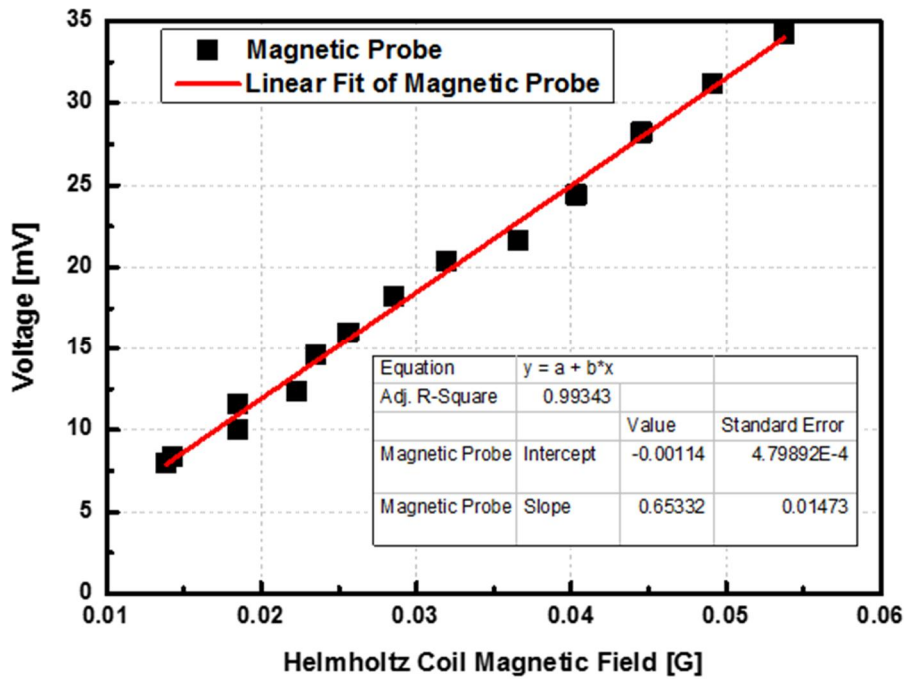


Figure 3.17 Calibration results of one turn loop coils at 500 MHz using Helmholtz coil for known magnetic field source [52].

MP1 is installed below the antenna port 1, and MP2 is 105° toroidally away from MP1 as shown in Figure 3.18. Location of the MP2 is determined in consideration of magnetic field line with pitch angle produced by ~ 30 kA of plasma current. While MP1 is at fixed location ($R = 0.73$ m, $Z = -0.346$ m), MP2 is mounted on linear guide to scan radially from $R = 0.55$ m to $R = 0.8$ m. Linear guide can reach $R = 0.5$ m, but it is usually positioned up to $R = 0.55$ m or $R = 0.6$ m to avoid unwanted plasma perturbation. Coils are connected to 50 ohm vacuum coaxial cables and vacuum BNC flange. Probe signals are digitized using an oscilloscope (2.5 GS/s for 400 us) and phase difference between adjacent probes is calculated from the zero-crossing detection code. Magnetic probes are able to measure n_ϕ in single shot and n_R by shot-to-shot radial scanning. When pitch angle of magnetic field line is small enough, it is reasonable to assume that

n_ϕ and n_R are analogous to n_\parallel and n_\perp , respectively. n_\parallel is obtained from phase difference $\Delta\phi$ and distance Δx between adjacent probes by following relation

$$n_\parallel = \frac{c\Delta\phi}{\omega\Delta x}.$$

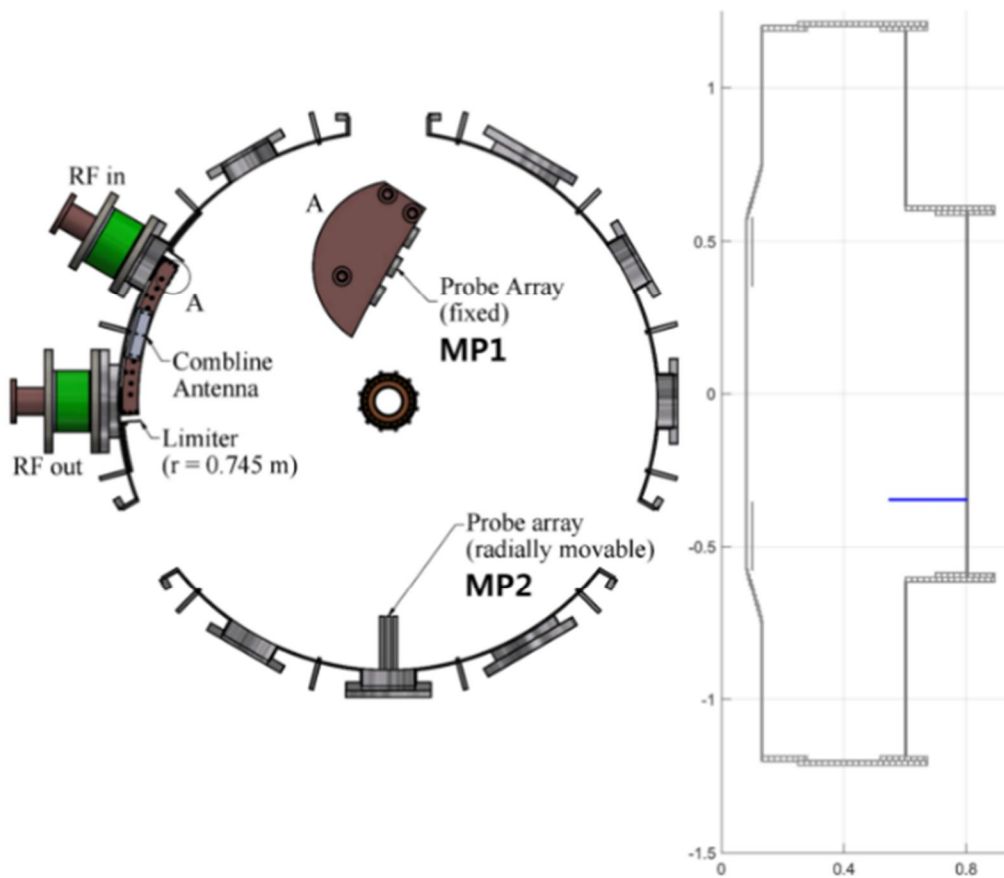


Figure 3.18 Location of magnetic probes installed in VEST chamber [52].

Chapter 4. Antenna-Plasma Coupling Simulation [53]

In this section, antenna-plasma simulations and preliminary experiments are carried out to investigate the coupling characteristics of the fast wave in VEST. Coupling simulation is conducted using the COMSOL Multiphysics [54] to predict precisely coupling efficiency and coupled power ratio of fast and slow waves. Plasma and fast wave launcher are modeled using three dimensional cold magnetized plasma dielectric tensor and developed comb-line antenna. Preliminary experiments are performed by transmitting low power with a signal generator and coupling efficiency is measured by using directional couplers. In section 4.1, details of the coupling simulations are described. Simulation results with effect of wave frequency, gap size and electron density on coupling are presented and discussed in section 4.2. Especially, electron density for the coupling study is categorized according to the characteristic densities, $n_{cutoff,slow}$, $n_{cutoff,fast}$ and $n_{confluence}$, as described in equation (2.2), (2.3) and (2.4). To understand the characteristics of coupling for different density cases more clearly, simulation study in this section is mainly carried out for $B_0 = 0.2T$ where coupling window is wider than that of 0.1 T and the characteristic densities are obviously distinguished from each other. And then the results are compared with the case of $B_0 = 0.1T$ where present VEST discharges are operated. In section 4.3, preliminary experimental results are presented and discussed with measurement of coupling efficiency, edge electron density profile and the simulation results.

4.1. COMSOL Multiphysics Modelling

Three-dimensional cold magnetized plasma modelling is attempted using the commercial full wave FEM solver, COMSOL Multiphysics. It was successfully utilized for the analysis of electron cyclotron heating (ECH) pre-ionization plasmas in VEST

[55]. The same COMSOL RF module is used to solve the Maxwell equation as follows:

$$\nabla \times \mu_r^{-1}(\nabla \times \bar{E}) - k_0^2(\bar{\epsilon}_r - i\bar{\sigma}/\omega\epsilon_0) \cdot \bar{E} = 0, \quad (4.1)$$

where μ_r is the relative permeability, \bar{E} is the electric field, k_0 is the wave number of free space, $\bar{\epsilon}_r$ is the relative dielectric tensor, $\bar{\sigma}$ is the conductivity tensor, ω is the angular wave frequency, and ϵ_0 is the permittivity of vacuum. Plasma medium is modeled by the conductivity tensor derived from dielectric tensor in inhomogeneous plasma. The dielectric tensor for toroidal geometry is derived from the Hermitian tensor [55] including collision terms. It can be expressed with a multiplication factor $(\omega + iv)/\omega$ for m_e terms as follows:

$$\begin{aligned} K_{xx} &= 1 - A\omega_{pi}^2(\omega^2 - \omega_{cix}^2) - B[\omega^2 - \omega_{cex}^2/(1 + iZ)^2], \\ K_{yy} &= 1 - A\omega_{pi}^2(\omega^2 - \omega_{ciy}^2) - B[\omega^2 - \omega_{cey}^2/(1 + iZ)^2], \\ K_{zz} &= 1 - A\omega_{pi}^2(\omega^2 - \omega_{ciz}^2) - B[\omega^2 - \omega_{cez}^2/(1 + iZ)^2], \\ K_{xy} &= A(\omega_{cix}\omega_{ciy} - i\omega\omega_{ciz}) + B[\omega_{cex}\omega_{cey}/(1 + iZ)^2 + i\omega\omega_{cez}/(1 + iZ)], \\ K_{yx} &= A(\omega_{cix}\omega_{ciy} + i\omega\omega_{ciz}) + B[\omega_{cex}\omega_{cey}/(1 + iZ)^2 - i\omega\omega_{cez}/(1 + iZ)], \\ K_{xz} &= A(\omega_{cix}\omega_{ciz} + i\omega\omega_{ciy}) + B[\omega_{cex}\omega_{cez}/(1 + iZ)^2 - i\omega\omega_{cey}/(1 + iZ)], \\ K_{zx} &= A(\omega_{cix}\omega_{ciz} - i\omega\omega_{ciy}) + B[\omega_{cex}\omega_{cez}/(1 + iZ)^2 + i\omega\omega_{cey}/(1 + iZ)], \\ K_{yz} &= A(\omega_{ciy}\omega_{ciz} - i\omega\omega_{cix}) + B[\omega_{cey}\omega_{cez}/(1 + iZ)^2 + i\omega\omega_{cex}/(1 + iZ)], \\ K_{zy} &= A(\omega_{ciy}\omega_{ciz} + i\omega\omega_{cix}) + B[\omega_{cey}\omega_{cez}/(1 + iZ)^2 - i\omega\omega_{cex}/(1 + iZ)], \end{aligned} \quad (4.2)$$

where $\omega_{cjk} = \frac{|q_j|B_k}{m_j}$ ($j = i, e, k = x, y, z$), $\omega_{cj}^2 = \sum_k \omega_{cjk}^2$, $Z = \frac{v}{\omega}$, $A = \frac{\omega_{pi}^2}{\omega^2(\omega^2 - \omega_{ci}^2)}$

and $B = \frac{[\omega_{pe}^2/(1+iZ)]}{\omega^2(\omega^2 - \omega_{ce}^2/(1+iZ)^2)}$. For the proper simulation, ad hoc collision term is set to

artificially large value to describe the energy loss by power absorption in cold plasma.

Schematic drawings of the combline antenna and simulation domains are depicted in Figure 4.1. The antenna size is 42cm \times 20cm and curved suitably for the VEST device.

The antenna consists of exciting strap, radiating strap, field isolator and Faraday shield.

Two tungsten limiters are located on both side of the antenna. Radial position of the Faraday shield and limiters are $R = 74.5\text{cm}$ and $R = 74\text{cm}$ respectively. Simulation domains include the antenna structure and edge plasma region. Radial thickness of plasma medium is set to be 15cm and the combine antenna faces the plasma domain. Plasma density ranges from the cut-off density of slow wave to beyond confluence density depending on the study case. Toroidal magnetic field B_ϕ has $1/R$ radial gradient and it can be expressed in the Cartesian coordinate as $B_x = B_\phi \sin\theta$, $B_y = 0$, $B_z = B_\phi \cos\theta$ and $\tan\theta = \frac{z}{R_0+a-x}$. Perfectly matched layer (PML) is applied to make sure of absorbing the outgoing waves without reflections and the remainder surfaces surrounding plasma domain are set to periodic boundary condition. Input parameters for the simulation are summarized in Table 4.1.

Table 4.1 Summarized input parameters for the coupling simulations.

Input Parameters	Values
TF strength (B_0)	0.2 / 0.1 T
Input power	10 kW
Wave frequency	480 / 485 / 490 / 495 / 500 / 505 / 510 MHz
Gap size	0.5 / 1.0 / 1.5 / 2.0 cm
Electron density profile	Case 1: $n_{\text{cutoff, slow}} < n_e < n_{\text{cutoff, fast}}$
	Case 2: $n_{\text{cutoff, fast}} < n_e < n_{\text{confluence}}$
	Case 3: $n_e \sim n_{\text{confluence}}$
	Case 4: $n_e \gg n_{\text{confluence}}$

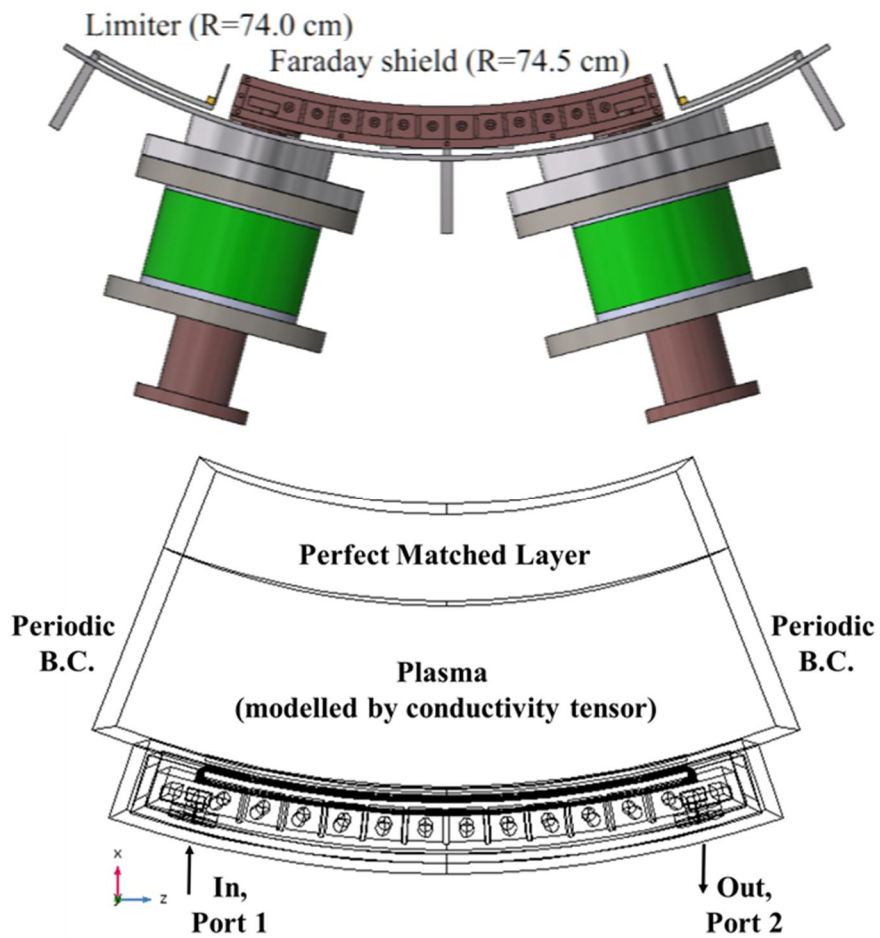
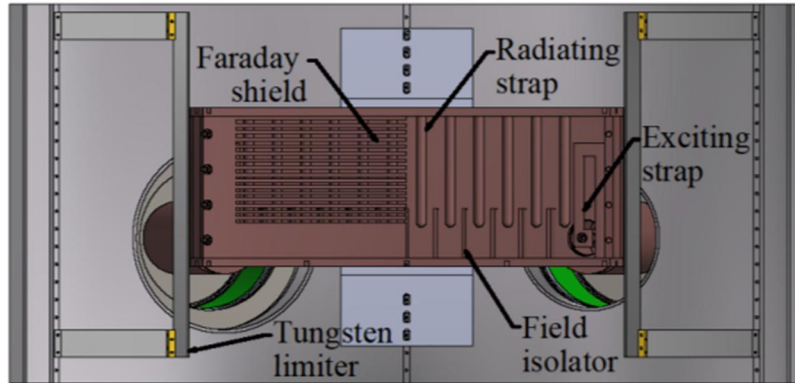


Figure 4.1 Schematic drawings of the antenna and simulation domains for the antenna-plasma coupling simulation.

Output parameters of the simulation are S-parameters, field patterns and coupled power ratio of fast and slow waves. Transmission coefficient (T) is defined as the ratio of output power at port 2 to input power at port 1 in the Figure 4.1 and represented as an S-parameter S_{21} . Reflection coefficient (R) is defined as the ratio of reflected power to input power at port 1 and represented as an S-parameter S_{11} . Coupling coefficient (C) can be obtained from the relation $T + R + C = 1$ to fulfill the energy conservation.

Field propagation patterns of E_y and E_ϕ show the coupling of the fast wave and slow wave, respectively. Quantitative coupled power ratio of the fast and slow wave can be calculated from surface integral of each Poynting vector, $P_{r,F} = \frac{1}{2} \text{Re}[E_y^* H_\phi]$ and $P_{r,S} = \frac{1}{2} \text{Re}[-E_\phi^* H_y]$, in front of the antenna. Before the parameter study described in section 4.2, energy conservation is checked to validate the simulation by comparing the sum of surface integral of Poynting vectors with total coupling power from S-parameters. Coupled powers are shown in Figure 4.2 when the gap is varied to be 0.5, 1.0, 1.5 and 2.0cm, respectively. The plasma density profile is the Case 2 of the Table I and the frequency is 500 MHz. As shown in the Figure 4.2, total coupled power is equal to the sum of coupled powers of each wave branch.

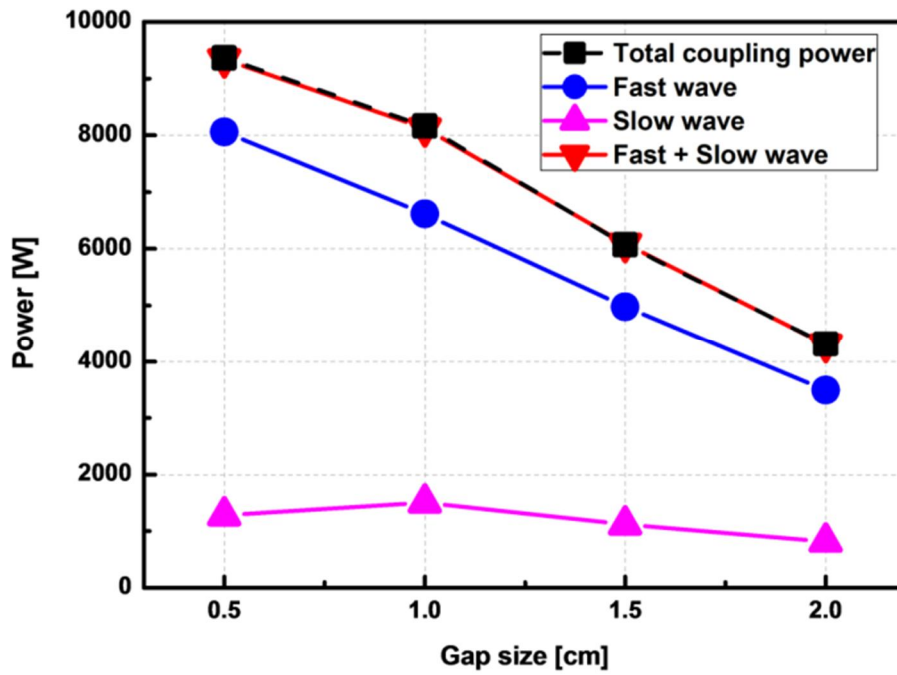


Figure 4.2 Total coupling power and the coupled power of fast wave and slow wave calculated from the surface integral of each Poynting vector. B_0 is 0.2T, wave frequency is 500MHz, gap size is varied from 0.5cm to 2cm and $n_{\text{cutoff, fast}} < n_e < n_{\text{confluence}}$.

4.2. Coupling Study

4.2.1. Wave Frequency Effect

For the analysis of coupling in various plasma conditions, wave frequency and gap size scans are conducted at $B_0 = 0.2\text{T}$ and electron density profile ($n_{\text{cutoff, fast}} < n_e < n_{\text{confluence}}$) in which the fast wave can propagate.

Firstly, frequency is scanned from 480MHz to 510MHz with the bandwidth of the combline antenna to find the operating frequency that has the most efficient fast wave power coupling characteristics. Figure 4.3 (a) and (b) show the S-parameters and power flow coefficients depending on the wave frequency. In all frequency cases, reflection is less than 10% and the coupling is almost more than 80%. Maximum power coupling of $\sim 90\%$ occurs near the 500MHz with $n_{\parallel 0} \sim 4.5$ as shown in Figure 4.4. The coupling efficiency increases with frequency until 505MHz in spite of increasing k_{\parallel} wave number as shown in Figure 4.4 (b), which usually reduces the coupling. It might be due to the vacuum load [45] of the developed antenna and the increase of perpendicular refractive index with input density level in proportion to wave frequency. Figure 4.3 (c) and (d) show the relative fraction and absolute input power fraction of fast and slow wave, respectively. The relative and absolute fractions of two wave branches are similar since overall fast wave coupling efficiency with frequency is high due to the suitable fast wave coupling density. At 500MHz, 80% and 10% in total input power are coupled to fast and slow wave branches, respectively.

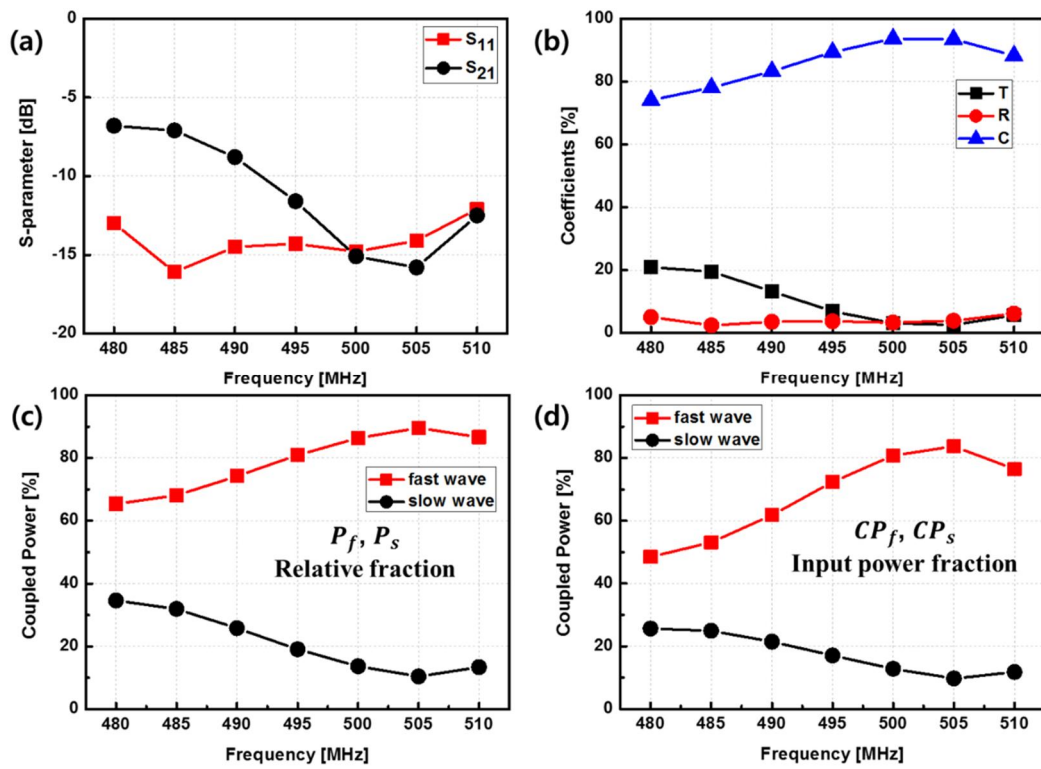


Figure 4.3 (a) S-parameter, (b) transmission (T), reflection (R) and coupling (C) coefficient, (c) relative fraction of coupled fast wave and slow wave, and (d) input power fraction of coupled fast wave and slow wave depending on wave frequency. B_0 is 0.2T, gap size is 0.5cm and $n_{\text{cutoff, fast}} < n_e < n_{\text{confluence}}$

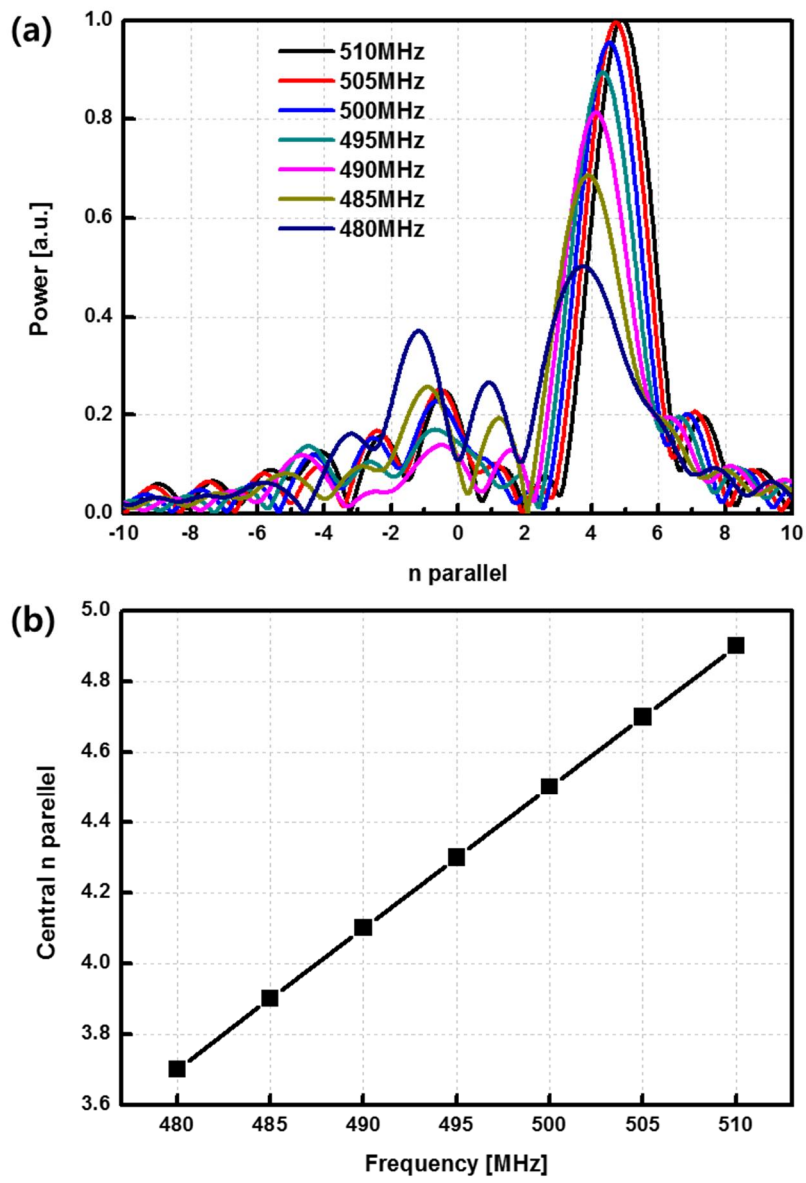


Figure 4.4 (a) Spectrum of n_{\parallel} and (b) $n_{\parallel 0}$ of excited wave from the comb-line antenna depending on wave frequency.

4.2.2. Gap Size Effect

Gap size scan is performed from 0.5cm to 2.0cm at the frequency of 500MHz that has the most efficient fast wave coupling efficiency. Gap size is defined as the distance between outer surface of the antenna, i.e. Faraday shield, and plasma domain indicating radial thickness of edge vacuum region in the chamber. The gap sizes are estimated by calculating e-folding length $d = \frac{1}{2ik_0 n_{\perp}}$ for the following relation of wave power, $P \propto E^2 \propto \exp(-2ik_0 n_{\perp} x)$. It can be described by the perpendicular refractive index of fast wave expressed in equation (2.1). The perpendicular refractive index $n_{\perp F}^2$ can be expressed by $-(n_{\parallel}^2 - 1)$ in case of zero electron density, which gives Stix notation $R = L = S = 1$, and the e-folding length is expressed by $d = \frac{\lambda}{4\pi \sqrt{n_{\parallel}^2 - 1}}$. With $n_{\parallel 0} \sim 4.5$ at 500MHz, e-folding length for wave power is about 1cm. The shortest gap size is 0.5cm by considering the radial position of limiters located at both ends of the antenna as shown in Figure 4.1. The coupled power varies from 90% to 60% with gap size between 0.5cm and 1.5cm as shown in Figure 4.5 (b). Relative fraction of fast wave is consistently larger than 80% since that of slow wave decreases as well with the gap size. However, it slightly decreases with the increase of gap size as shown in Figure 4.5 (c) due to larger cutoff density and evanescent layer thickness than slow wave. The absolute coupled power of the fast wave decreases with the gap size, so the gap size should be kept shorter than 1.5cm to couple more than 50% of input power as shown in Figure 4.5 (d).

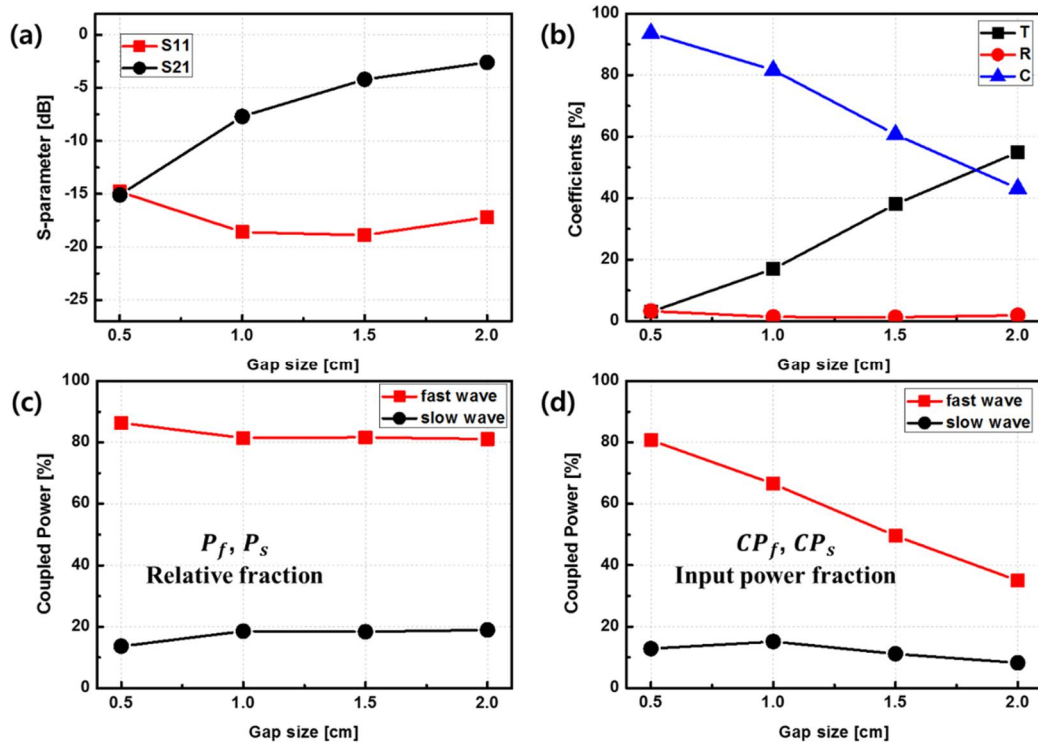


Figure 4.5 (a) S-parameter, (b) transmission (T), reflection (R) and coupling (C) coefficient, (c) relative fraction of coupled fast wave and slow wave, and (d) input power fraction of coupled fast wave and slow wave depending on gap size. B_0 is $0.2T$, wave frequency is 500MHz and $n_{\text{cutoff, fast}} < n_e < n_{\text{confluence}}$.

4.2.3. Electron Density Effect

Wave frequency of 500 MHz and gap size of 0.5cm which is the shortest length constrained by limiter size in VEST are shown to be suitable for efficient fast wave coupling in the previous section. With these parameters, the effect of electron density profile on fast wave coupling is investigated. Considering cutoff and confluence densities, four cases are classified for input electron density profiles as summarized in Table 4.1. The cutoff density of slow wave, cutoff density of fast wave, and confluence density are expressed in equation (2.2), (2.3) and (2.4), respectively. Case 1 represents electron density range between slow wave cutoff density and fast wave cutoff density, $n_{\text{cutoff, slow}} < n_e < n_{\text{cutoff, fast}}$, to describe fast wave cutoff case. Case 2 means the fast wave coupling window between fast wave cutoff density and confluence density, $n_{\text{cutoff, fast}} < n_e < n_{\text{confluence}}$, to describe fast wave coupling case. Case 3 and Case 4 have confluence density that plays a role as high density limit for the propagation of fast wave and slow wave by mode conversion and backward propagation. Case 3 gives electron density profile similar to confluence density, $n_e \sim n_{\text{confluence}}$, which is expected to be a marginal case for coupling and confluence. Case 4 describes much higher density about 10 times the confluence density, $n_e \gg n_{\text{confluence}}$, where waves are strongly evanescent.

Figure 4.6 (a) shows the radial profile of cutoff density and confluence density at 500MHz and 0.2 T in VEST. Cutoff density of slow wave is much lower than that of fast wave and it is about $3 \times 10^{15} m^{-3}$. Figure 4.6 (b) shows the E_y and E_ϕ field patterns plotted for each density profile cases. Case 1, low density limit for fast wave launching, shows that E_y field is attenuated in front of antenna indicating that fast wave is rarely launched and strongly evanescent while E_ϕ field of slow wave appears inside the bulk plasma in spite of weak field due to low total coupled power. Case 2 shows that both waves are coupled to plasma in rather different regions. Fast wave can propagate in even more dense plasma region, inward region, than slow wave. It is the main feature of the

fast wave current drive scheme compared to the slow wave scheme in high density plasmas of reactor grade. Case 3 describes the situation that coupled fast wave shortly encounters confluence density region in the edge plasma without further propagation. Case 4 also shows the evanescent fields with very low coupling efficiency.

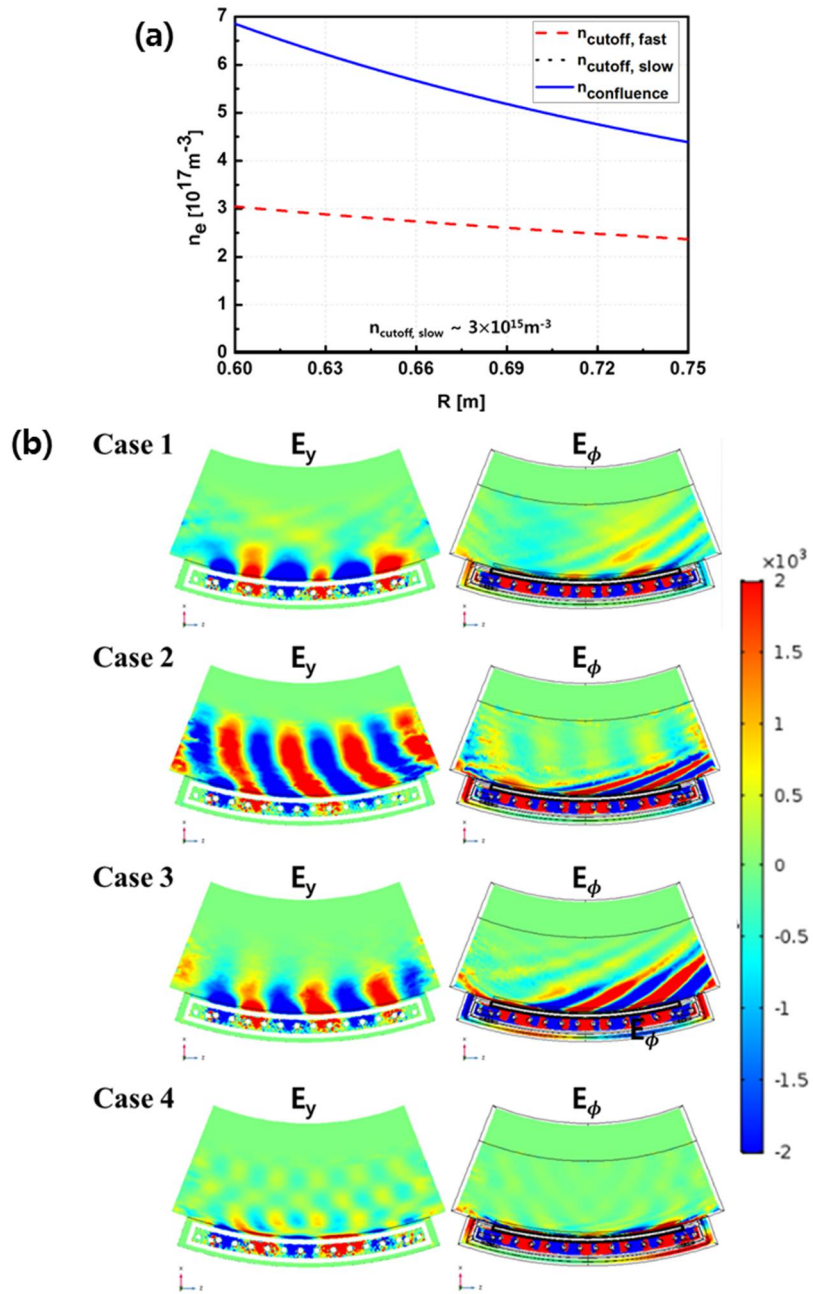


Figure 4.6 Radial density profiles of (a) cutoff density for fast wave and slow wave and confluence density, and (b) field patterns of fast wave (E_y) and slow wave (E_ϕ) depending on density profiles. B_0 is 0.2T, wave frequency is 500MHz and gap size is 0.5cm.

Transmission, reflection, and coupling coefficients (T, R, and C), relative and absolute coupled power fraction of fast and slow waves for those four cases are summarized in Table 4.2 and plotted in Figure 4.7. As edge electron density is lower than the fast wave cutoff density (Case 1), 93% of the wave power is transmitted to antenna output port without power coupling to plasmas. Higher relative coupled power to slow wave is due to its much lower cutoff density. In fast wave coupling case noted by Case 2, coupling efficiency increases up to about 90% and most power is coupled to the fast wave as expected. With higher density noted by Case 3 and 4, confluence density region exist in front of antenna and coupling efficiency decreases with the increase of transmission and reflection.

Table 4.2 Summarized coefficients of each electron density profile cases (unit: %).

Electron density profiles	T	R	C	P_f	P_s	CP_f	CP_s
Case 1 (cutoff)	93	2	5	12	88	1	4
Case 2 (coupling)	3	3	94	86	14	81	13
Case 3 (coupling + confluence)	26	2	72	72	28	51	21
Case 4 (confluence)	63	17	20	80	20	16	4

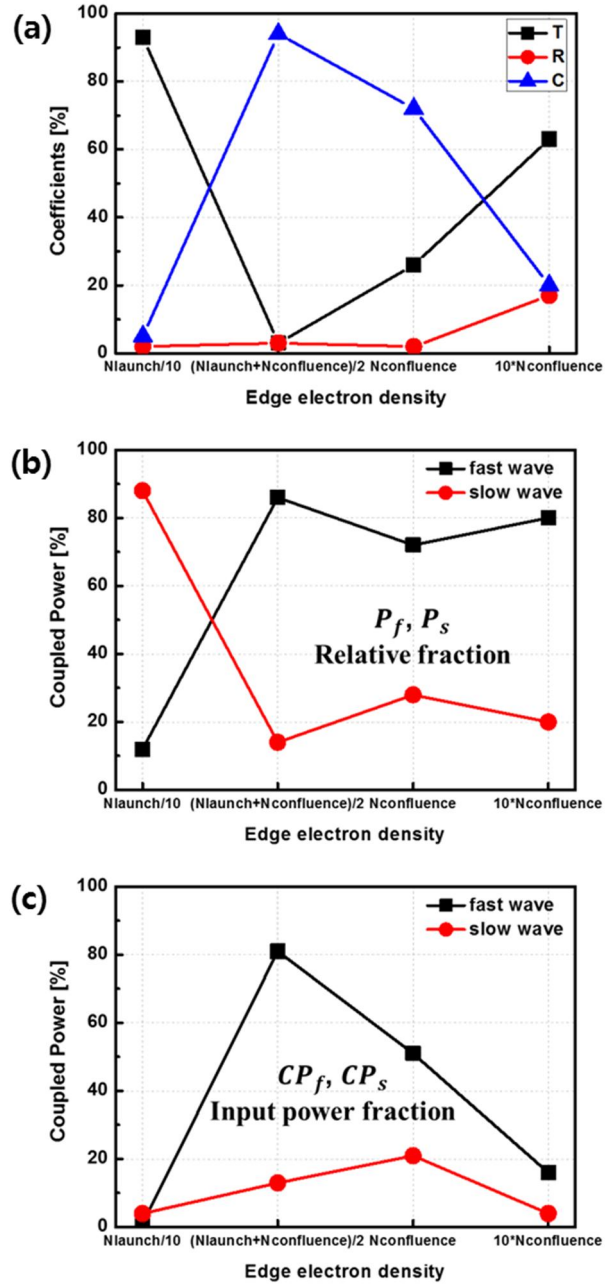


Figure 4.7 (a) Transmission (T), reflection (R) and coupling (C) coefficients, (b) relative fraction of fast and slow wave, and (c) input power fraction of fast and slow wave depending on edge electron density. $B_0 = 0.2\text{T}$, $f = 500\text{MHz}$ and gap size is 0.5cm .

Actually, VEST discharges are operated at the magnetic fields of $B_0 = 0.1\text{T}$, where cutoff density is almost the same as confluence density of fast wave ($n_{\text{cutoff, fast}} \sim n_{\text{confluence}} \sim 10^{17}\text{ m}^{-3}$). As shown in Figure 4.8, the fast wave coupling under $B_0 = 0.1\text{T}$ can be meaningful only in Case 3 ($n_e \sim n_{\text{confluence}}$) and cannot be classified clearly for different electron density cases. The field patterns of E_y and E_ϕ for the Case 2 and Case 3 under $B_0 = 0.1\text{T}$ show mode conversion into the slow wave similar to the Case 3 of $B_0 = 0.2\text{T}$ with narrow propagation window for the fast wave.

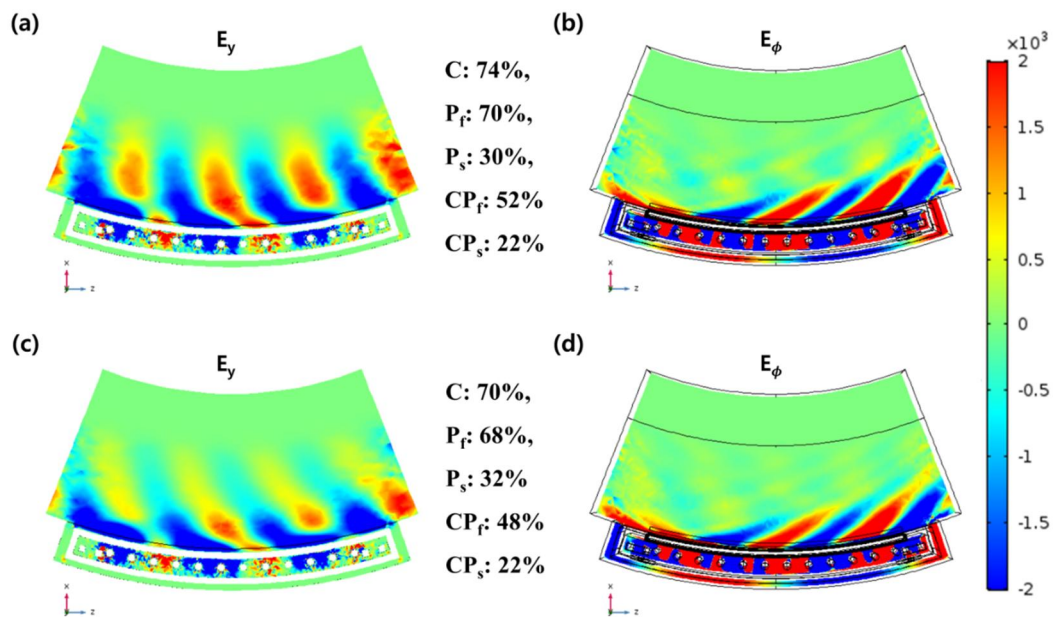


Figure 4.8 Field patterns of fast wave (E_y) and slow wave (E_ϕ) depending on edge density under $B_0 = 0.1\text{T}$. (a) E_y , (b) E_ϕ field in case of $n_{\text{cutoff, fast}} < n_e < n_{\text{confluence}}$, and (c) E_y , (d) E_ϕ field in case of $n_e \sim n_{\text{confluence}}$. Wave frequency is 500MHz and gap size is 0.5cm.

4.3. Comparison with Preliminary Experiment

Preliminary coupling experiments using a low power signal generator (-8dBm, 500MHz) have been carried out to obtain the coupling characteristics before high power experiment. Power transfer by signal generator from antenna port 1(in) to port 2(out) is done with and without plasma discharges. Square of transmitted voltage ratios measured from port 2 in both cases of vacuum and plasma give the transmission coefficient $T = \left| \frac{V_{T,plasma}}{V_{T,vacuum}} \right|^2$ because the two-port combine antenna configuration has rare reflections regardless of vacuum or plasma load except extremely high edge electron density, which is already confirmed with previous simulation results. The coupling efficiency C could be obtained from the relation $1 - T = R + C \approx C$. To adjust the edge electron density level for fast wave launching as investigated by simulations in section 4.2, ohmic discharges with plasma current of about 35 kA are produced as target plasmas with edge electron density of $\sim 10^{17} \text{ m}^{-3}$ which is comparable to the fast wave cutoff density in the present VEST operation at $B_0 \sim 0.1\text{T}$.

Coupling of fast wave is crucially dependent on the edge electron density profile as discussed in the simulation for four cases. Experimental results also show similar correlation between edge electron density and coupling efficiency. Figure 4.9 (a) shows spatial electron density profiles at four temporal points during the discharge including the cutoff density for fast wave plotted with dashed line. Figure 4.9 (b) shows the discharge information such as plasma current, toroidal magnetic field, vertical magnetic field, H-alpha line intensity, antenna limiter current for monitoring the contact with plasma, electron density measured with triple probe and coupling efficiency (C). As noted, the ohmic discharge is operated at $B_0 \sim 0.1\text{T}$ and the cutoff density for fast wave is about 10^{17} m^{-3} . Coupling efficiency (C) starts to increase as electron density in front of antenna ($R=0.745\text{m}$) attains the level of the cutoff density. It varies from 30% to 90 %

correlated with the evolution of edge electron density during entire discharge. In Figure 4.9, $t = 302\text{ms}$ is matched with the Case 1 which describes the cutoff density, $t = 304\text{ms}$ and $t = 312\text{ms}$ are matched with the Case 3 which shows the marginal fast wave propagation window with the electron density comparable to confluence density, and $t = 308\text{ms}$ is matched with the Case 4 which describes strongly decaying evanescent wave in a very high density plasma. So, it is expected that coupling efficiency decreases with higher edge electron density than confluence density, but, at $t = 308\text{ms}$, measured coupling efficiency keeps on increasing to 90% with edge electron density contrary to the prediction of simulation results.

To analyze experimental results, the coupling simulation is carried out with input parameter of measured electron densities at $t = 304\text{ms}$ and $t = 308\text{ms}$ under $B_0 = 0.1\text{T}$, wave frequency of 500MHz and gap size of 0.5cm . Figure 4.10 (a) and (b) show E_y and E_ϕ field, respectively at $t = 304\text{ms}$. The coupling efficiency is 68%, which is similar to 60% coupling of measurement. Narrow propagation window for the fast wave under $B_0 = 0.1\text{T}$ makes E_y field of the fast wave be less clear than $B_0 = 0.2\text{T}$ as shown in the previous section and more than 30% of the slow wave is coupled to edge plasma. Figure 4.10 (c) and (d) show the evanescent fields in high density plasma at $t = 308\text{ms}$ and the coupling efficiency is about 40% unlike the measurements of 90% in Figure 4.9 (b).

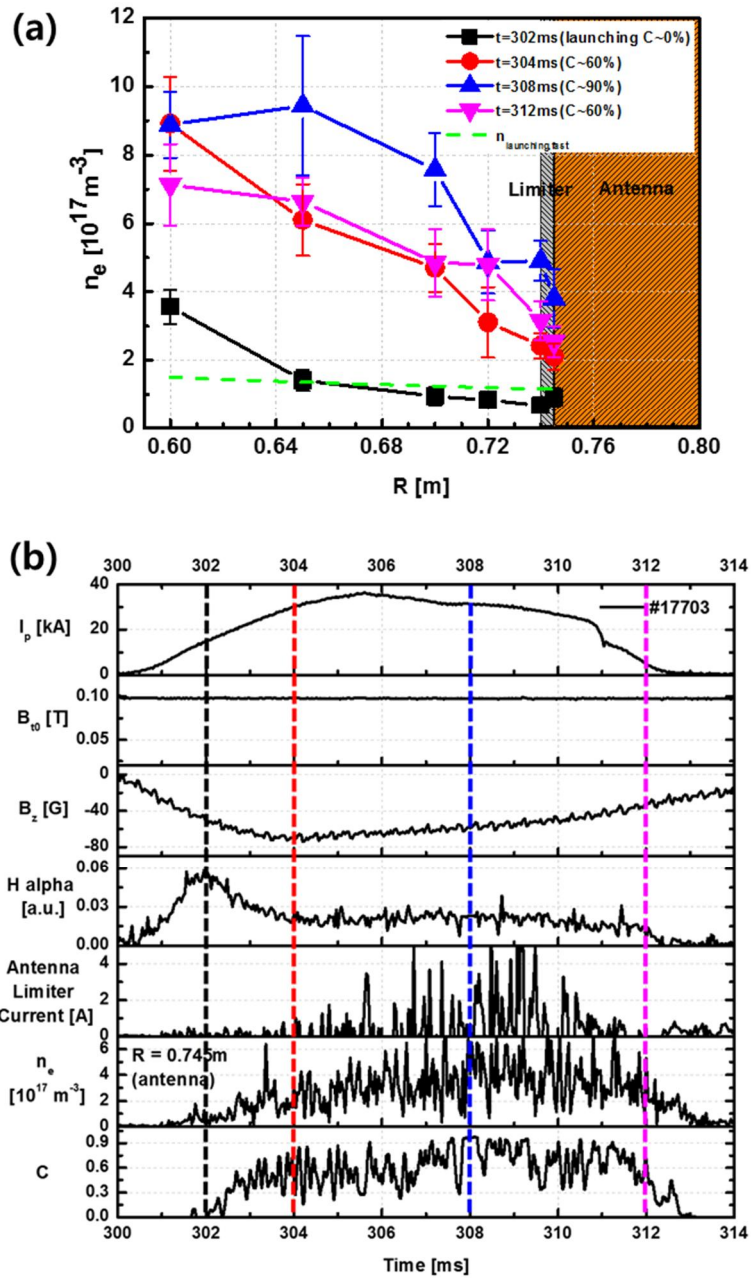


Figure 4.9 (a) Radial profiles of electron density for four temporal points, and (b) time evolution of discharge #17703.

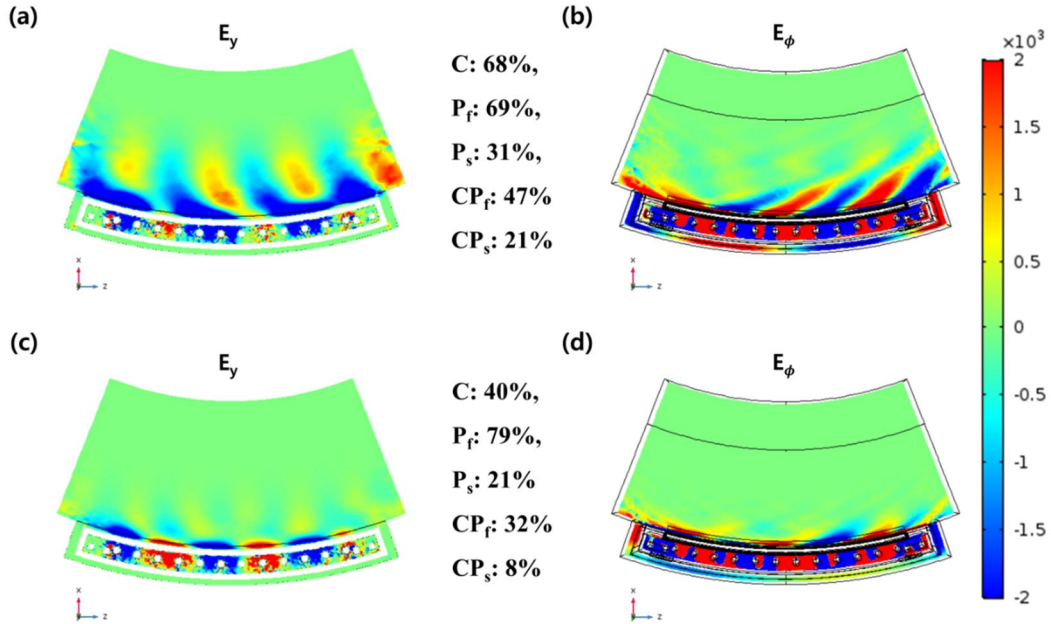


Figure 4.10 (a) Field patterns of fast wave (E_y) and slow wave (E_ϕ) depending on measured edge electron density of #17703. (a) E_y , (b) E_ϕ field at $t = 304$ ms, and (c) E_y , (d) E_ϕ field at $t = 308$ ms. B_0 is 0.1T, wave frequency is 500MHz and gap size is 0.5cm.

In summary, experimental results are consistent with coupling simulation in rather low density plasma ($n_{cutoff,fast} < n_e < n_{confluence}$), but fast wave coupling is enhanced contrary to the prediction in high density plasma ($\geq n_{confluence}$) where accessibility condition is not satisfied. The discrepancy between experiment and coupling simulation implies that another factor can play a major role in high density plasma overcoming the accessibility limit. Especially, it is expected that $n_{||}$ -upshift causes modification of coupling and propagation conditions. To identify cause for the discrepancy between experimental results and coupling simulation, wave measurement in plasma is desired for more information on coupling and propagation of fast wave.

Chapter 5. Fast Wave Coupling Experiments [52]

In this section, experimental investigation on propagation and coupling of lower hybrid fast wave (LHFW) is carried out with wave measurement utilizing magnetic probes in VEST. Especially, several coupling experiments are conducted in marginal ($n_e \geq n_{confluence}$) and prohibited ($n_e \gg n_{confluence}$) regime for fast wave coupling to investigate the modified accessibility condition. Magnetic probes are capable of measuring power spectrums and refractive indexes (n_{\parallel} & n_{\perp}) of B_{ϕ} and B_y fields. Radial profiles of the refractive indexes, pump wave power and broadening width of B_{ϕ} field, which is the most dominant magnetic field of fast wave polarization, are measured from fast wave coupling experiments. Experimental results of wave measurements are presented in section 5.1 and 5.2. Enhanced coupling of LHFW in high density plasmas are presented in 5.3 and it is discussed with n_{\parallel} -upshift via wave scattering in section 5.4.

5.1. Detection of n_{\parallel} -upshift and Modified Propagation Path

Fast wave coupling experiments are conducted with target plasma produced by ohmic discharges at B_0 (@ $R = 0.4$ m) = 0.1 T. Plasma current is approximately 25 kA and electron density at $R = 0.745$ m in scrape-off-layer (SOL) behind the antenna limiter located at $R = 0.74$ m is $2\text{-}4 \times 10^{17} \text{ m}^{-3}$ from triple probe measurement. As electron density in SOL plasma is higher than the confluence density ($\sim 1.5 \times 10^{17} \text{ m}^{-3}$), it leads to narrow coupling window as discussed in the previous coupling study. Under the marginal regime ($n_e \geq n_{confluence}$), coupling experiments and wave measurements are conducted. Figure 5.1 (a) exhibits time evolution of shot #19526. As edge electron density measured by a triple probe exceeds the fast wave cutoff density in ohmic phase, coupling coefficient increases to 70 %. Signals of MP1 located below the antenna are

measured at $t = 304$ ms to analyze power spectrums and n_{\parallel} of B_{ϕ} and B_y fields as shown in Figure 5.1 (b) and (c). Pump wave frequency is detected to be 500 MHz of injected wave for both B_{ϕ} and B_y fields as expected. Pump wave power of B_{ϕ} field is roughly 10 times higher than that of B_y , indicating that most of launched wave from the comb-line antenna is fast wave. Dominant n_{\parallel} of B_{ϕ} field is 3.8 ± 0.7 similar to $n_{\parallel 0} \sim 4.5$ calculated from COMSOL simulation as demonstrated in Figure 5.1 (c).

Radial profiles of n_{\parallel} and n_{\perp} are obtained from shot-to-shot measurements of MP2 at $t = 304$ ms in ohmic discharges. Reproducibility of ohmic discharges is confirmed as shown in Figure 5.2 (a). Before analyzing the probe data, pitch angle of magnetic field line is accounted for slow wave coupling by misalignment between faraday shield, which is parallel to toroidal magnetic field, and helical magnetic field line. Figure 5.2 (b) shows radial profiles of toroidal field strength, poloidal field strength and pitch angle at plasma current of about 25 kA. Pitch angle is defined as $\alpha = \arctan(B_p/B_t)$. Small pitch angle ($5^{\circ} \leq \alpha \leq 10^{\circ}$) for all measurement positions of magnetic probes indicates negligible slow wave coupling effect [57] validates the assumption of $(n_{\phi}, n_R) \sim (n_{\parallel}, n_{\perp})$. Figure 5.2 (c) exhibits poloidal view of plasma boundary with additional MP2 location shown as blue solid line, which is displayed in reconstructed equilibrium with red dot line for $\psi_N = 0.95$ surface. Radial position of measurement covers from SOL to slightly inside of the last-closed-flux surface (LCFS) according to the reconstruction.

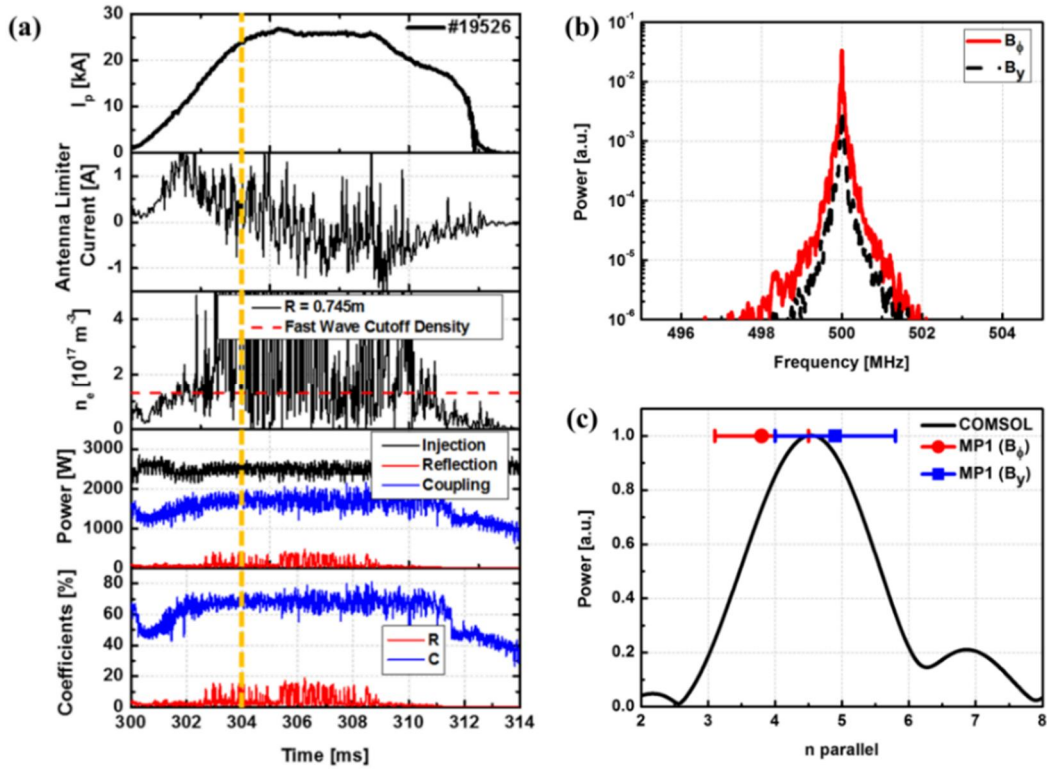


Figure 5.1 (a) Time evolution of plasma current, limiter current, edge electron density, RF power and coefficients of reflection and coupling in ohmic discharge (#19526) at $B_0 = 0.1 \text{ T}$. (b) Power spectrums of B_ϕ and B_y fields. (c) n_{\parallel} of B_ϕ field detected at MP1 and $n_{\parallel 0}$ spectrum of B_ϕ field calculated from COMSOL simulation. Measurement results of (b) and (c) are from MP1 at $t = 304 \text{ ms}$ in the shot # 19526.

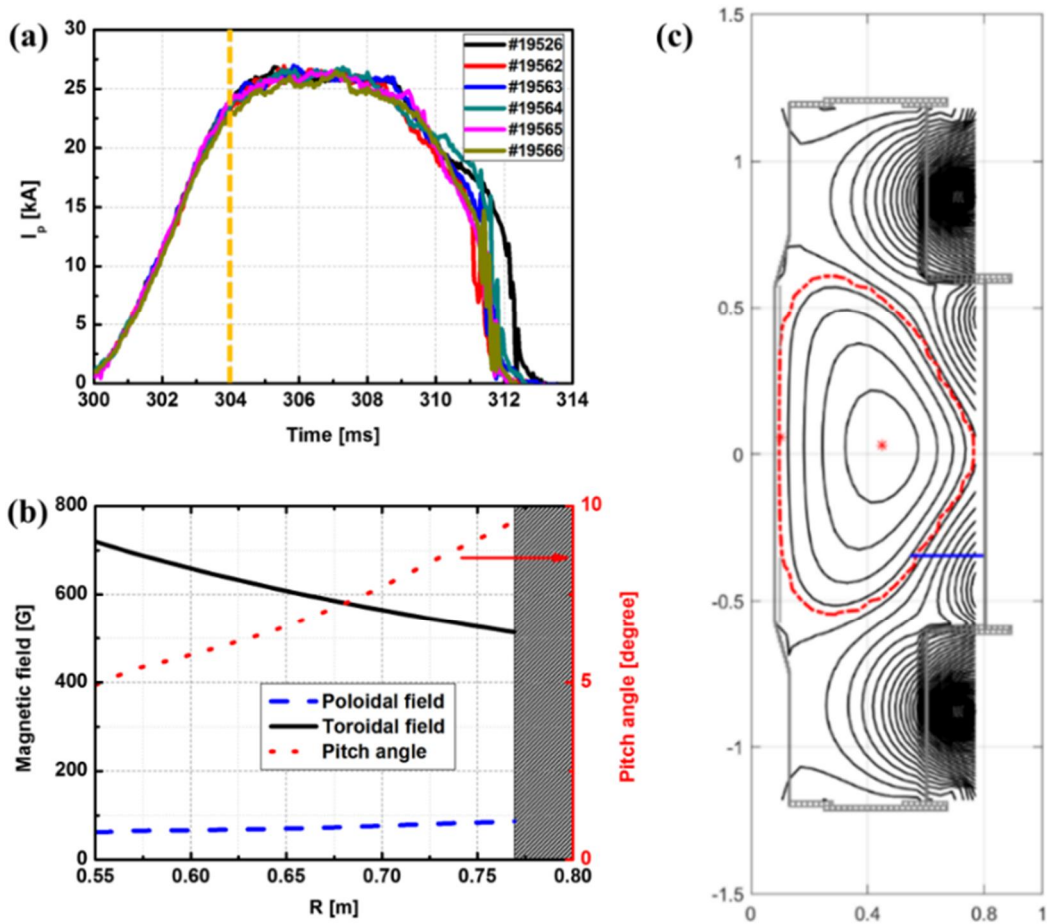


Figure 5.2 (a) Plasma current of reproduced ohmic discharges. (b) Radial profile of toroidal field strength, poloidal field strength and pitch angle at $I_p \sim 25$ kA. (c) Plasma boundary from equilibrium reconstruction of shot #19526 and location of magnetic probes (MP2) in poloidal plane of VEST. (Surface of $\psi_N = 0.95$ and position of MP2 are displayed as red dot line and blue solid line respectively.)

Measurement results by MP2 are shown in Figure 5.3 (a) and Figure 5.3 (b). Clear n_{\parallel} -upshift is observed, where n_{\parallel} of lower than 5 at MP1 location increases up to 6 – 10 at MP2 location. Toroidal effect, which is usually assumed as the most probable explanation for n_{\parallel} -upshift, is not sufficient to explain the upshift. Parallel wavenumber is expressed as follows:

$$k_{\parallel} = \frac{\vec{k} \cdot \vec{B}}{|\vec{B}|} = \frac{k_r B_r + \left(\frac{m}{r}\right) B_{\theta} + \left(\frac{n}{R}\right) B_{\phi}}{|\vec{B}|} \quad (5.1)$$

where m is poloidal mode number, n is toroidal mode number, r is minor radius and R is major radius. Toroidal mode number is conserved quantity in toroidally axisymmetric geometry approximately satisfying $n_{\parallel} \propto n_{\phi} \propto 1/R$. Figure 5.3 (a) demonstrates that significant n_{\parallel} -upshift occurs even at the same major radius indicating another effect except the toroidal effect. It is described in section 5.4 with wave scattering due to density fluctuation in SOL region.

To identify polarization of detected waves, n_{\perp} is also measured from radial scanning of MP2. Figure 5.3 (b) shows radial profile of n_{\perp} with the value between 4 and 9. Detected magnetic field at MP2 is identified as a component of the fast wave resulting from n_{\parallel} (< 10), n_e ($\geq 2 \times 10^{17} \text{ m}^{-3}$ from electron density of SOL and pre-ionization plasmas for typical ohmic discharges in VEST) and dispersion relation as demonstrated in Figure 5.3 (c). Propagating waves detected at various MP2 positions are the fast wave component despite the narrow range of accessibility condition for fast wave at $B_0 = 0.1$ T. The result is consistent with the coupling coefficient enhanced in ohmic phase up to 70%. n_{\parallel} -upshift is usually expected to be present in numerous studies to bridge the spectral gap. Nevertheless, direct measurement is rarely reported due to easier absorption of high n_{\parallel} component of waves with higher population of resonant electrons ($n_{\parallel LD} \equiv c/4v_T$). In the VEST experiment, target plasma for the fast wave coupling has

low temperature ($\sim 10\text{eV}$) in edge region. In addition, Landau damping of fast wave is known to be much weaker than that of slow wave. Therefore, absorption of fast wave by collisionless Landau damping is anticipated to be very low in this coupling experiment with large spectral gap and it is accordingly rather advantageous to see the behavior of propagating waves.

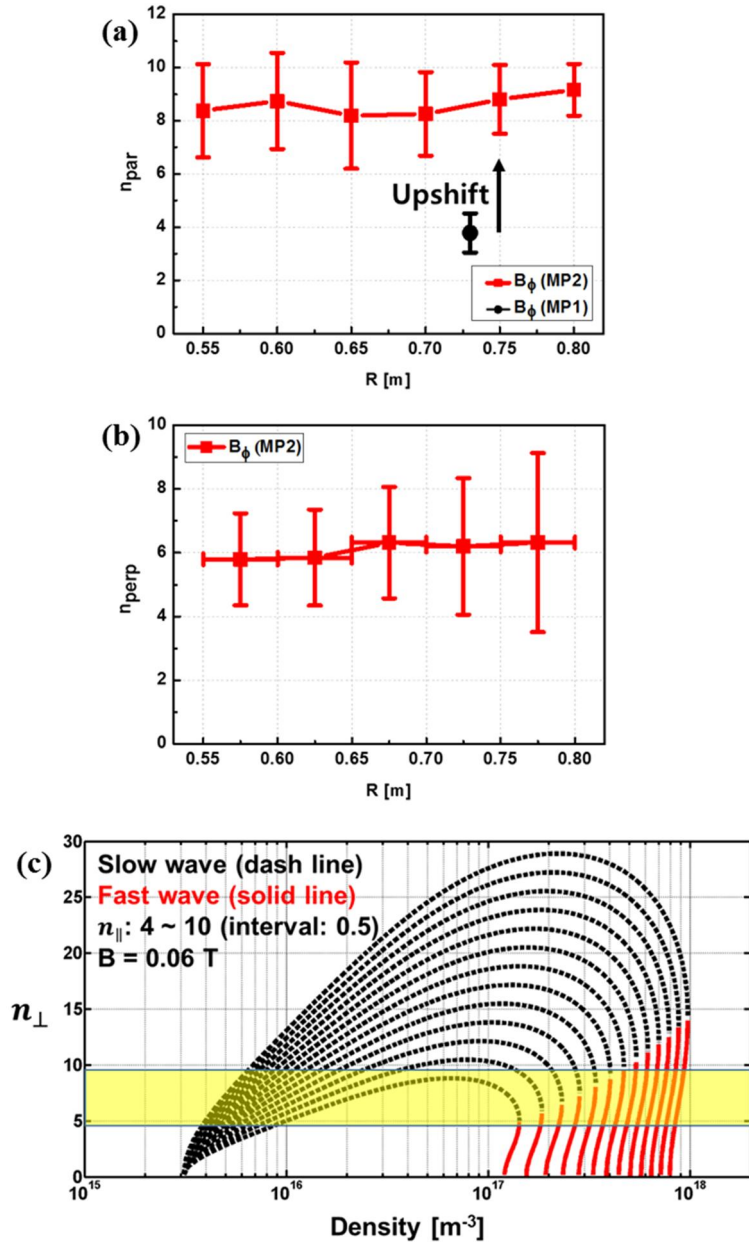


Figure 5.3 (a) Radial profiles of n_{\parallel} measured at MP1 and MP2. (b) Radial profiles of n_{\perp} measured at MP2. (c) n_{\perp} of slow wave and fast wave as a function of plasma density derived from dispersion relation. (Shaded region signifies the range of n_{\perp} measured at MP2 considering the range of n_{\parallel} and edge n_e).

Figure 5.4 indicates modification of wave propagation path. Although COMSOL simulation developed from the previous work [45, 53] provides edge localized coupling ($R > 0.7$ m) by unsatisfied accessibility condition, measurements of pump wave profiles at MP2 are deviated largely from the simulation results as demonstrated in Figure 5.4. Additional RF power from 670 W to 1550 W produces a difference in a strictly radially inward region ($R < 0.7$ m) indicating that most propagating waves detected at the magnetic probe show more radial penetration characteristics than the prediction of COMSOL simulation. The result is consistent with the $n_{||}$ -upshift which allows propagation of fast wave in higher density plasma.

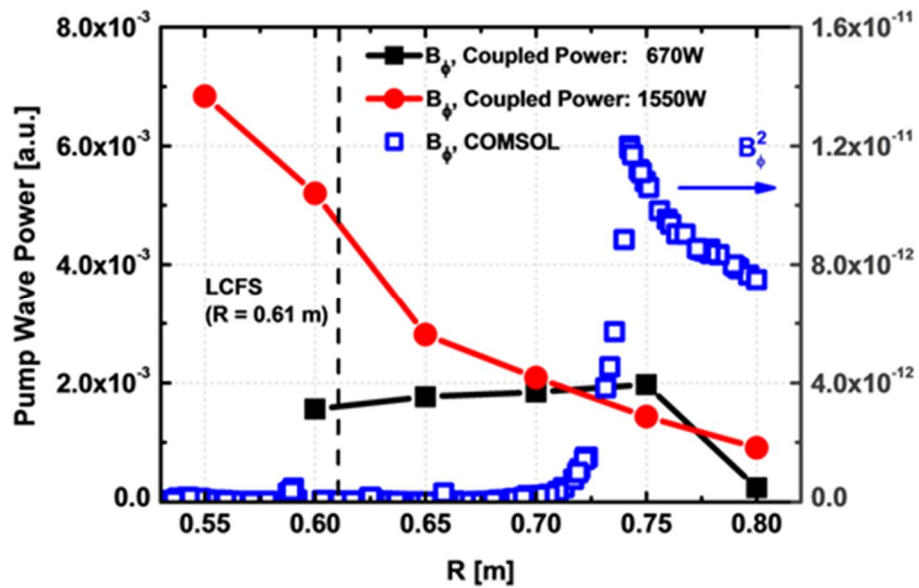


Figure 5.4 Radial profiles of pump wave power measured at MP2 and calculated from COMSOL simulation (Coupled wave power: 670 W and 1550 W).

5.2. Frequency Spectral Broadening by Wave Scattering

Broadening of power spectrums is observed as shown in Figure 5.5 (a). Broadening width at 20 dB below the spectrum peak is defined to quantify its degree of frequency spectral broadening. Figure 5.5(b) implies that frequency spectral broadening as well as n_{\parallel} -upshift (shown in Figure 5.3 (a)) occurs during fast wave propagation from near MP1 (i.e. near the antenna) to MP2. Broadening width at MP2 is 2-4 times larger than that of MP1 and increases toward inward region where electron density is higher.

It has been reported frequently that frequency spectral broadening of lower hybrid waves is related to parametric decay instability (PDI) or wave scattering in SOL region. PDI [31] indicates some characteristics of a threshold power (P_{th}), considerable frequency spread ($\Delta f/f \approx 0.3$) and frequency range ($\omega_0/\omega_{LH} \leq 2$) while wave scattering [34] indicates the absence of P_{th} and more narrow broadening spectrum than that of PDI. The degree of broadening and the frequency range of LHFWS ($\omega_0/\omega_{LH} \sim 15$) seem to signify wave scattering rather than PDI. Density fluctuation in the SOL and power dependency of the broadening width are investigated to clarify the main reason for spectral broadening. Density fluctuation ($\delta n_e/n_e$) is inferred from fluctuation of ion saturation current ($\delta I_{i,sat}/I_{i,sat}$) measured by a Langmuir probe. Figure 5.6 (a) demonstrates that broadening width measured at MP2 ($R = 0.6$ m) increases linearly with coupled wave power without P_{th} as reported in previous experimental study [34] on wave scattering while broadening width measured at MP1 is almost constant regardless of coupled wave power. Fluctuation of ion saturation current during discharge is exhibited in Figure 5.6 (b). Root mean square (RMS) value of the fluctuation during the entire discharge is 0.21, which is significantly large enough to affect the characteristics of lower hybrid wave propagation by wave scattering [35]. Therefore frequency spectral broadening is thought to be result from mostly wave scattering than

PDI in edge region.

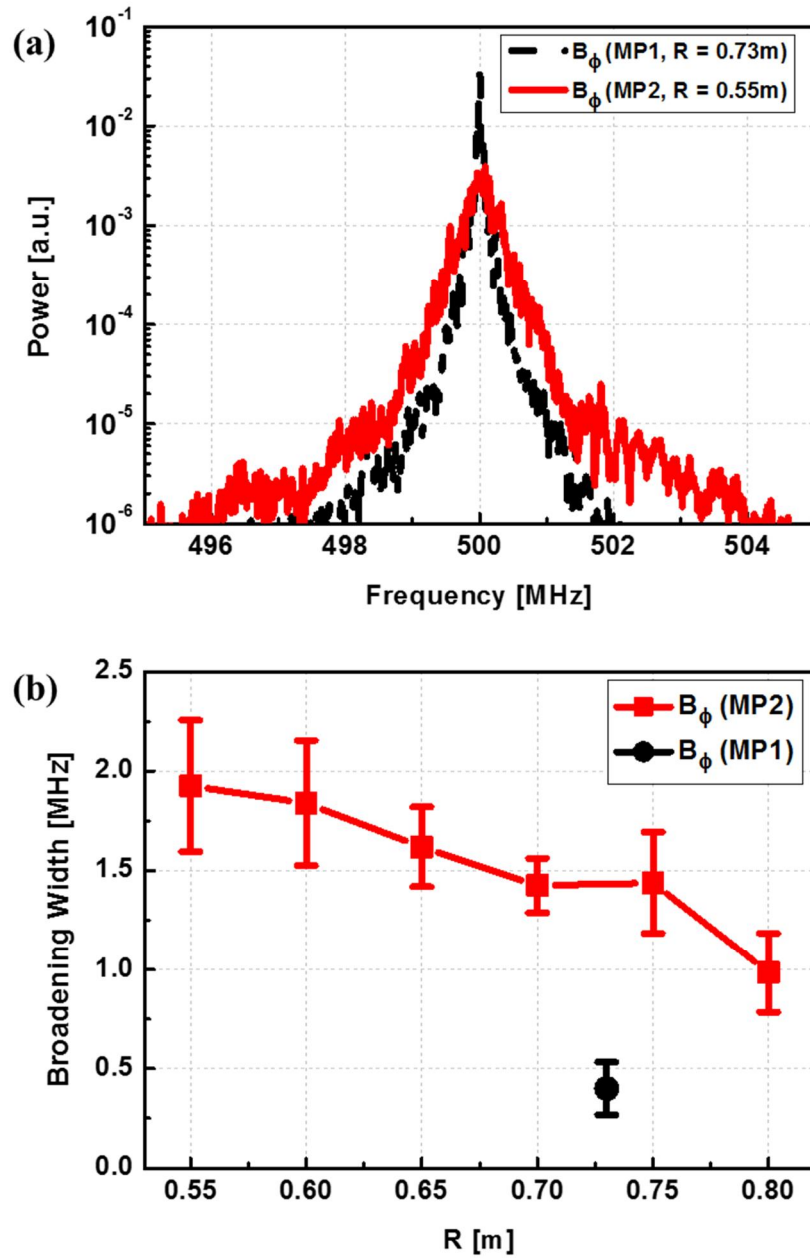


Figure 5.5 (a) Power spectra of B_ϕ field measured at MP1 and MP2. (b) Radial profile of broadening width of power spectra measured at MP1 and MP2.

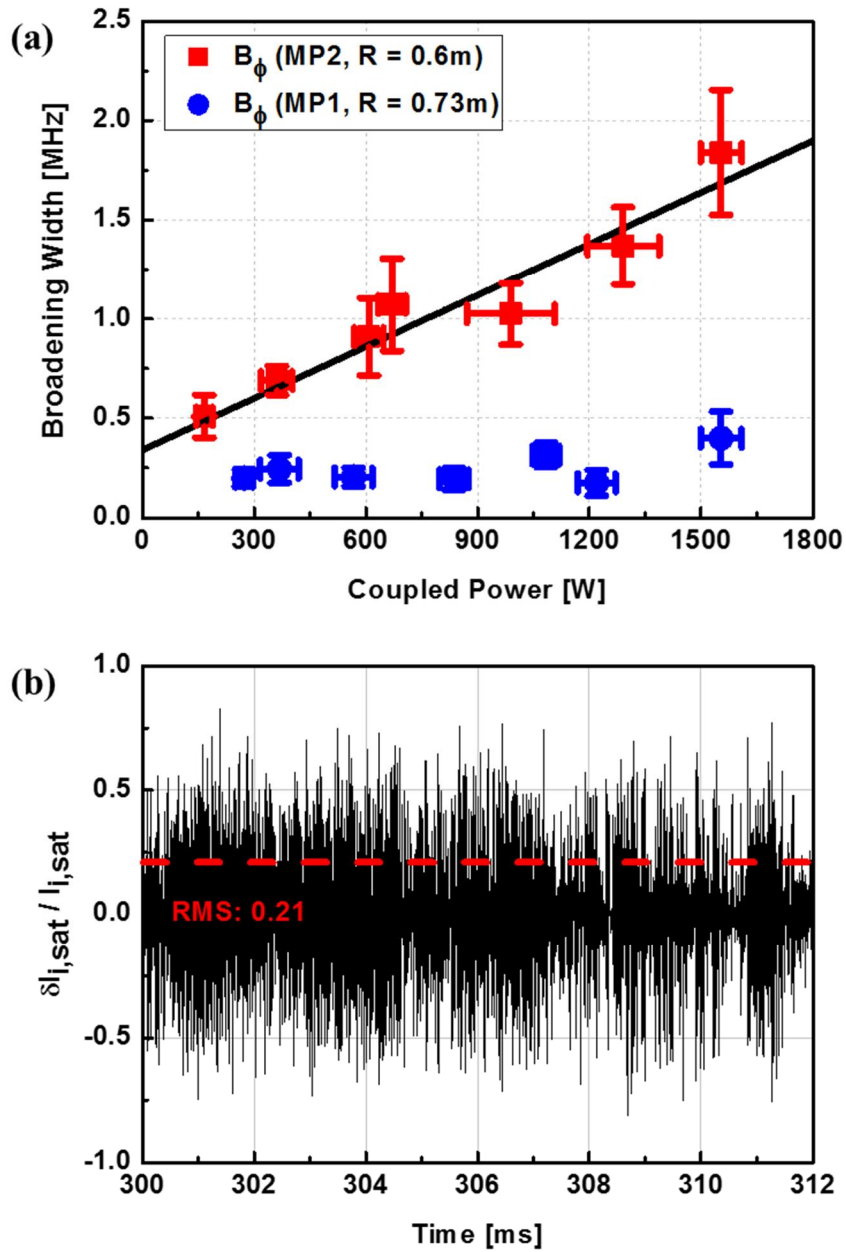


Figure 5.6 (a) Broadening width as a function of coupled wave power measured at MP1 and MP2 ($Z = -0.346$ m). (b) Fluctuation of ion saturation current during ohmic discharges in the SOL measured by a Langmuir probe ($R = 0.745$ m, $Z = 0$ m).

5.3. Enhanced Coupling of LHFV in High Density Plasmas

With the aid of n_{\parallel} -upshift via wave scattering, fast wave can propagate into the high density region where the accessibility condition is not satisfied. Further coupling experiments with plasma current of 100 kA are attempted to produce even higher density plasmas in prohibited regime ($n_e \gg n_{confluence}$) for the fast wave coupling. Outboard magnetic probes (MP2) cannot be used in these high current discharges due to high pitch angle of magnetic field line, which readily reaches inboard side at the toroidal location of the MP2. Figure 5.7 (a) exhibits time evolution of shot #20245. Coupling coefficient increases up to about 90% in ohmic phase with the increase of edge electron density. It can also partly contribute to the increased slow wave coupling by misalignment between faraday shield and magnetic field line. Pitch angle is in between 25° and 40° at plasma current of 100 kA as shown in Figure 5.7 (b) and consequently considerable slow wave coupling is expected. However, it is unable to explain the enhanced coupling entirely in high density plasma much higher than the confluence density. Accessibility condition of LHFV can be expressed as $n_{cutoff, fast} < n_e < n_{confluence}$, where $n_{cutoff, fast} \cong \frac{m_e \epsilon_0}{e^2} (n_{\parallel}^2 - 1) \omega \omega_{ce}$ and $n_{confluence} \cong \frac{1}{4} \frac{m_e \epsilon_0}{e^2} n_{\parallel}^2 \omega_{ce}^2$. Upper density limit, which is described as confluence density where both slow and fast waves are merged and propagate backwards with the same accessibility condition. Although edge electron density in front of the antenna ($R = 0.745\text{m}$) is about 10 times higher than the confluence density ($\sim 10^{17} \text{ m}^{-3}$) when $n_{\parallel 0} = 4.5$ is assumed, most of the injected power is coupled to plasma. It appears to be that modification of accessibility condition takes place in front of the antenna as well as in the radial path.

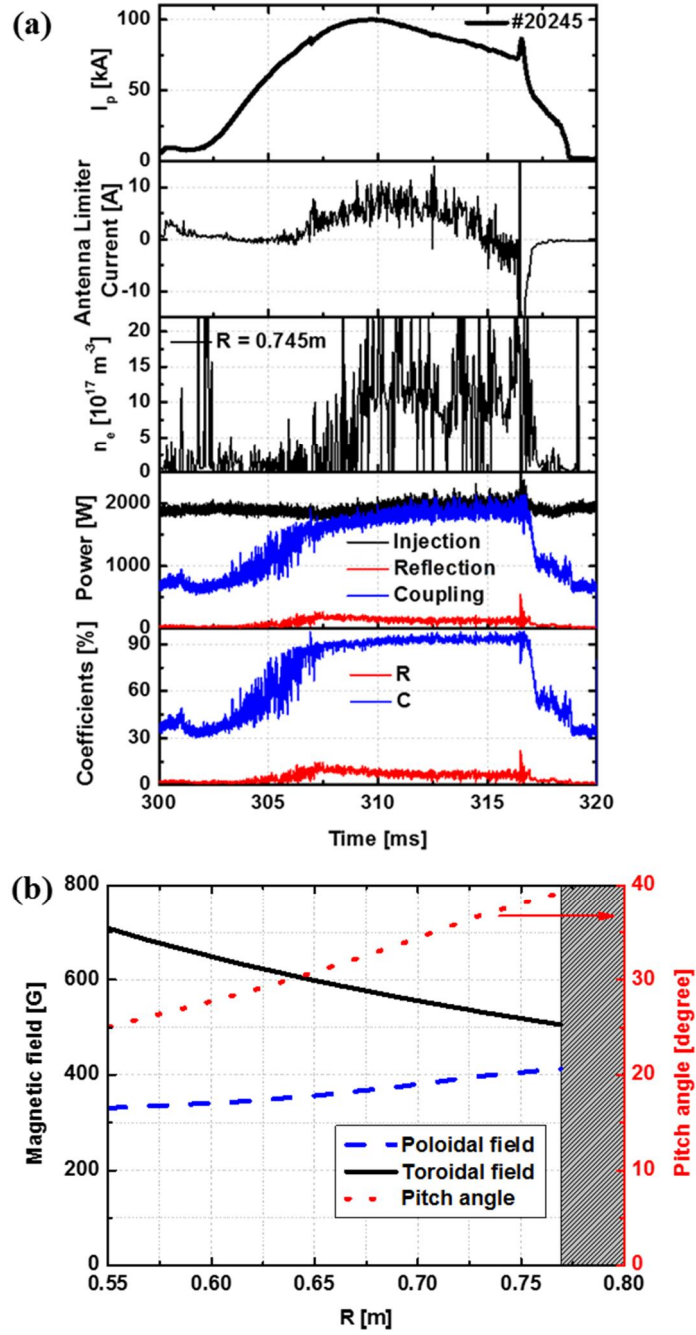


Figure 5.7 (a) Time evolution of plasma current, limiter current, edge electron density, RF power and coefficients of reflection and coupling in ohmic discharge (#20245) at $B_0 = 0.1 \text{ T}$.
 (b) Radial profile of B_t , B_p and pitch angle at $I_p \sim 100 \text{ kA}$.

Edge electron density at $R = 0.745$ m is measured at ohmic discharges to observe dependency of coupling coefficient with different edge electron density as shown in Figure 5.8. Confluence density for $n_{\parallel} = 4.5$ and $n_{\parallel} = 8.5$ is plotted in a dash dot line and a dash line respectively. Reflection coefficient (R) slightly increases with edge electron density and reflection is lower than 10% for the overall density regime. Coupling coefficient (C) continues to increase in high density plasma even though the accessibility condition in front of the antenna is not satisfied when n_{\parallel} is assumed to be the same as $n_{\parallel 0} = 4.5$. It additionally supports the idea that n_{\parallel} -upshift is present in front of the antenna. If n_{\parallel} is upshifted from $n_{\parallel 0} = 4.5$ to $n_{\parallel} = 8.5$, confluence density at the measurement position ($R = 0.745$ m) increases from $1.5 \times 10^{17} \text{ m}^{-3}$ to $8.3 \times 10^{17} \text{ m}^{-3}$, and then the accessibility condition is satisfied. Figure 5.8 illustrates expanded accessibility condition in high density plasma with n_{\parallel} -upshift.

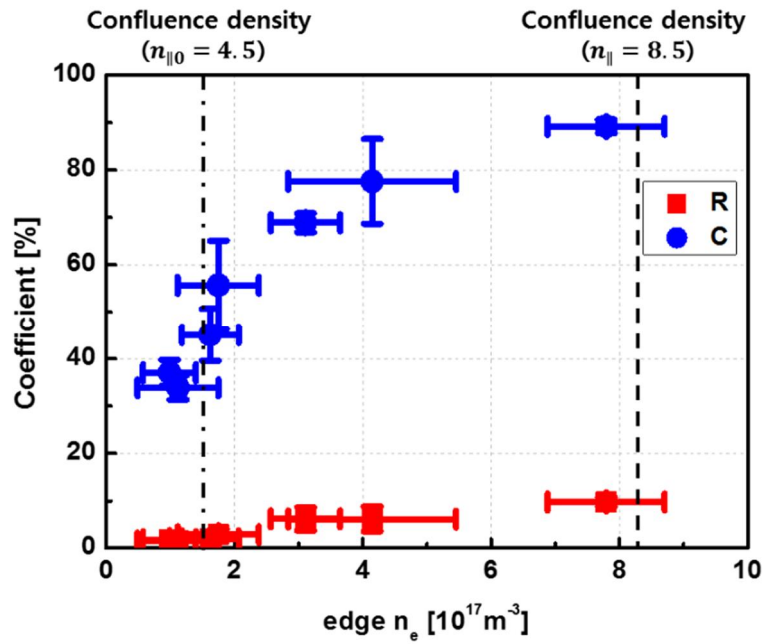


Figure 5.8 Coefficients of reflection (R) and coupling (C) as a function of edge electron density (R = 0.745 m). (Confluence density for $n_{\parallel 0} = 4.5$ and $n_{\parallel} = 8.5$ is displayed as dash dot line and dash line respectively.)

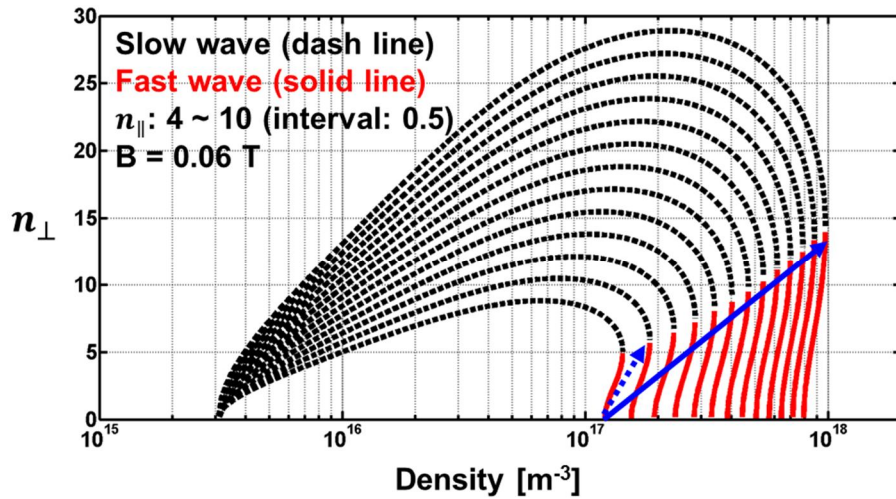


Figure 5.9 Expanded propagation region in high density plasma with n_{\parallel} -upshift.

5.4. Wave Scattering Effect on the Expanded Accessibility Conditions

The fluctuation $\delta I_{i,sat}/I_{i,sat}$ implies the density fluctuation ($\delta n_e/n_e$), and wave scattering intensity is mainly proportional to the density fluctuation squared [34, 35, 58]. Fluctuations measured in typical VEST ohmic discharges are not obviously varied by absolute value of plasma current while it is more strongly affected by the gap size defined as distance between the antenna and the LCFS. Figure 5.10 shows fluctuation of ion saturation current measured at radial position of the antenna as a function of the gap size in $I_p \sim 90$ kA discharge. Fluctuation is most evidently observed when the gap size is 2 cm, which is a typical gap size during ohmic discharges in VEST. RMS value of the fluctuation is not remarkably larger than lower plasma current case as shown in Figure 5.6 (b).

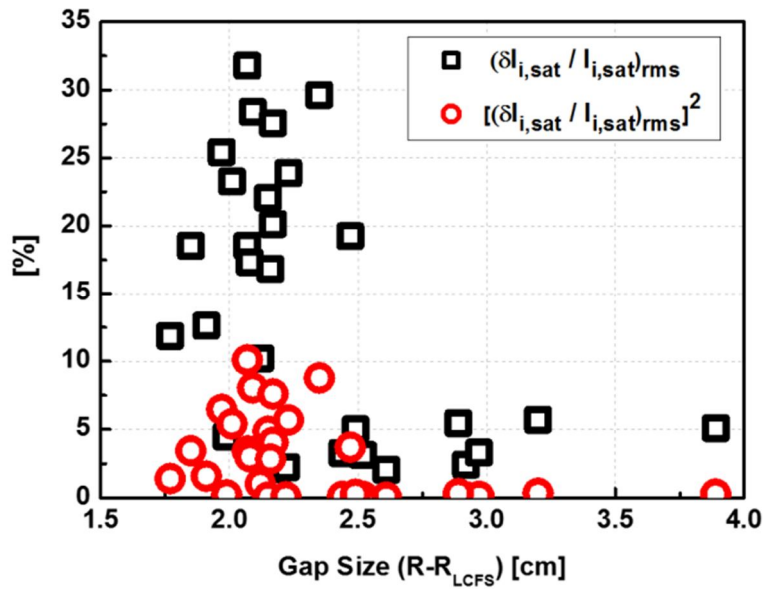


Figure 5.10 Fluctuation of ion saturation current and of square of ion saturation current in the SOL as a function of the distance between the radial position of antenna and the LCFS ($I_p \sim 90$ kA).

Scattering intensity based on linear scattering model is given by [34, 35, 58] as follows:

$$\frac{1}{l_s} = \frac{\sqrt{\pi}}{8} \left\langle \left(\frac{\delta n_e}{n_e} \right)^2 \right\rangle \xi_s \left[1 + \frac{3}{2} \left(M \frac{\xi_s}{k_0} \right)^2 \right] \quad (5.2)$$

where l_s is the scattering length, ξ_s is the poloidal wave vector of the density fluctuation, k_0 is the wave vector of the pump wave given by the dispersion relation, and $M = \frac{\langle \omega_{pe}^2 \rangle}{\omega_0 \Omega_{ce}}$. Equation 5.2 indicates that source for wave scattering is electron density fluctuation $\delta n_e/n_e$ and poloidal wave vector of density fluctuation ξ_s , which make the scattering intensity zero if $\delta n_e/n_e$ or ξ_s is zero. By putting aside the fluctuation-related terms $\delta n_e/n_e$ and ξ_s , intensity of the scattering is influenced by remaining term that can be described with a plasma dielectric constant ϵ as $\left(\frac{M}{k_0} \right)^2 \sim \left(\frac{\omega_{pe}}{\Omega_{ce}} \right)^2 = \epsilon$. Usually ST plasmas have a much higher plasma dielectric constant [22] than $\epsilon \sim 1$ of conventional tokamak, indicating the stronger scattering intensity. For VEST parameters in Figure 5.8, plasma dielectric constant is considerably high ($\epsilon \sim 4-20$) and likely to affect scattering intensity even when density fluctuation ($\delta n_e/n_e$) is not significantly varied. Enhanced coupling efficiency as a function of electron density as exhibited in Figure 5.8 is seemingly related with the enhanced scattering intensity.

Coefficients of coupling and reflection are measured with discharges at $B_0 = 0.05$ T to investigate regime in perspective of plasma dielectric constant ($\epsilon \sim n_e/B^2$) with changing magnetic field strength as well as electron density. Figure 5.11 shows coefficients of coupling and reflection as function of electron density and plasma dielectric constant. Figure 5.11 (a) exhibits that coupling efficiency for $B_0 = 0.05$ T is similar to that of $B_0 = 0.1$ T for the same electron density while reflection for $B_0 = 0.05$ T is about 2 times higher than that of $B_0 = 0.1$ T. For $B_0 = 0.05$ T, higher reflection may

be caused simply by the narrower accessibility range for fast wave propagation compared with the reflection for $B_0 = 0.1$ T. In addition, intensity of wave scattering is proportional to plasma dielectric constant as discussed so far. Therefore, plasma dielectric constant, which includes both electron density and magnetic field strength, more directly exhibits the relation between wave coupling and plasma parameters than the case with electron density only. Figure 5.11 (b) clearly demonstrates that the reflection increases with plasma dielectric constant and coupling efficiency at $B_0 = 0.1$ T is higher than coupling efficiency of $B_0 = 0.05$ T. It agrees with the accessibility determined by magnetic field strength; however, continuing increase of the coupling efficiency with plasma dielectric constant requires additional explanation such as n_{\parallel} -upshift via wave scattering. Plasma dielectric constant can be expressed in terms of confluence density as follows:

$$\epsilon \cong \frac{n_{\parallel}^2}{4} \frac{n_e}{n_{confluence}} \quad (5.3)$$

To explain continuing increase of the coupling efficiency, electron density must be lower than confluence density and from the equation 5.3 it is expressed by $n_{\parallel} \geq 2\sqrt{\epsilon}$. Therefore, $2\sqrt{\epsilon}$ is the minimum parallel refractive index for efficient coupling. Figure 5.12 indicates two regimes for $n_e < n_{confluence}$ and $n_e > n_{confluence}$ divided by the minimum parallel refractive index $2\sqrt{\epsilon}$. When plasma dielectric constant is 50, the minimum parallel refractive index is the 14, indicating minimum required n_{\parallel} -upshift. For the plasma dielectric constant of 10, which corresponds to shot # 19526 as shown in Figure 5.1 (a), the minimum parallel refractive index for coupling is about 6 while measured parallel refractive index is about 9, supporting high coupling efficiency as demonstrated in Figure 5.3 (a). As previously discussed, scattering intensity and required minimum n_{\parallel} for efficient coupling increase with plasma dielectric constant. If n_{\parallel} -upshift via wave scattering is enhanced sufficiently with the increase of plasma

dielectric constant, and is accordingly expanding and satisfying accessibility condition, then efficient coupling is possible in high density plasmas.

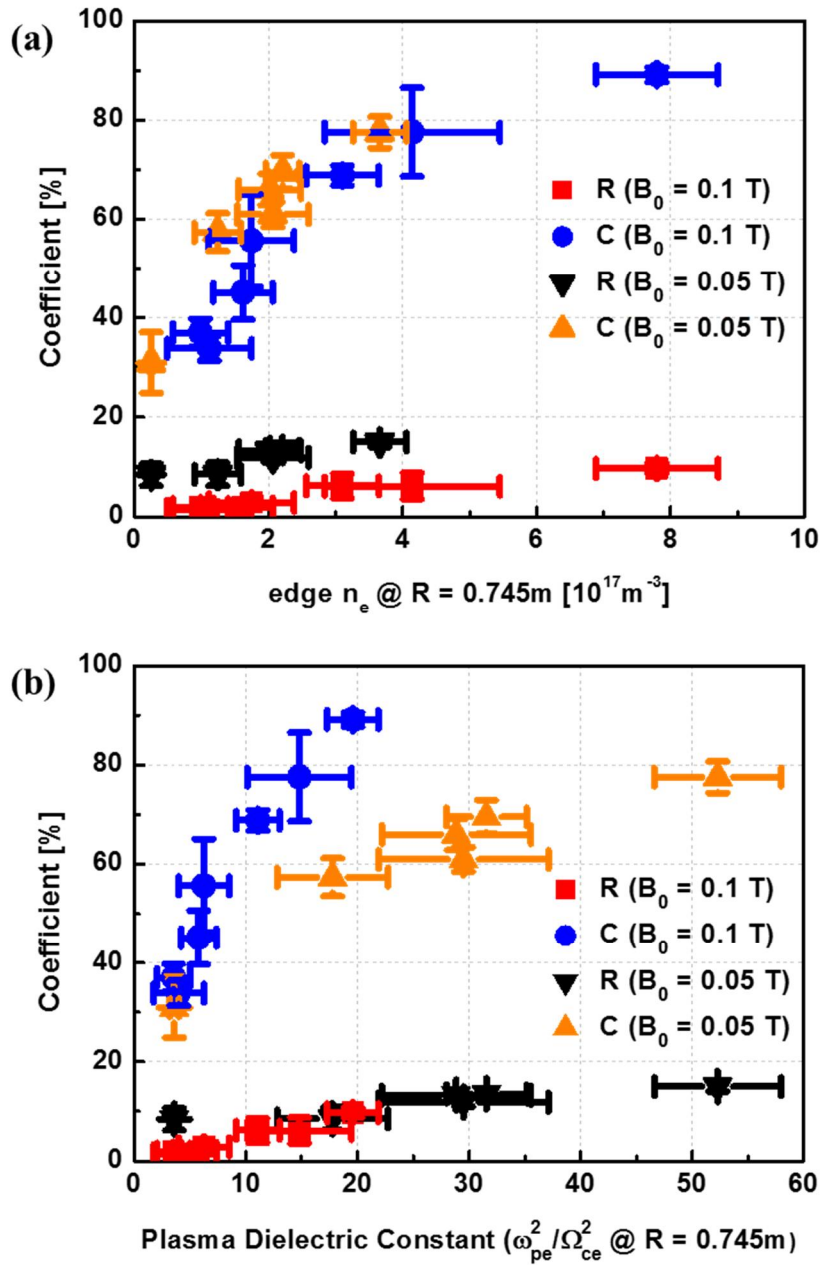


Figure 5.11 Coefficients of coupling and reflection under $B_0 = 0.1$ T and 0.05 T discharges as a function of (a) edge electron density and (b) plasma dielectric constant at $R = 0.745$ m.

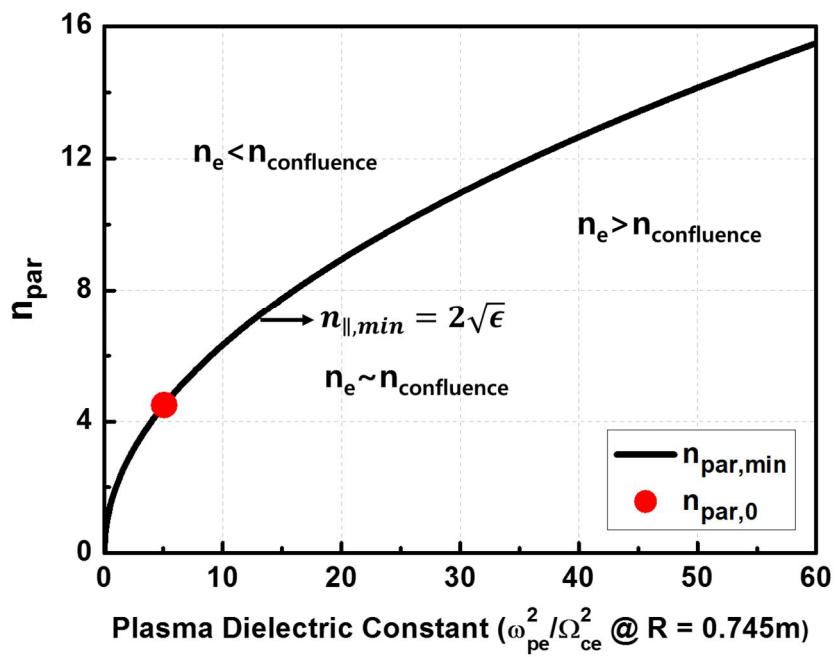


Figure 5.12 Minimum parallel refractive index in order to satisfy accessibility condition as a function of the plasma dielectric constant.

Chapter 6. Conclusion

6.1. Summary and Conclusion

LHFW scheme is proposed for central or off-axis current drive method in high density and high temperature plasmas. LHFW have advantages of relatively high E_z component contributing to Landau damping and of avoiding parametric instability in rather higher frequency range than other fast waves such as HHFW and Helicons. However, the coupling issues including both physical and technical point of view will be a key factor for the feasibility of the LHFW due to its narrow coupling window. Accessibility conditions also can be significantly modified from the linear theory by n_{\parallel} -upshift in plasma.

For the proof-of-principle, ST device has advantages in view of the fast wave coupling and absorption. Cutoff density for launching the fast wave is moderated with low magnetic field strength of ST compared to that of conventional tokamak. Absorption by Landau damping of the fast wave is much weaker than slow wave. It is the reason that the fast wave could be a good candidate for reactor grade plasmas in future but experiments for proof-of-principle might be difficult in present plasmas. Imaginary part of the perpendicular refractive index of the fast wave is comparable to that of the slow wave as plasma dielectric constant ($\epsilon \equiv \left(\frac{\omega_{pe}}{\Omega_{ce}}\right)^2 \propto \frac{\beta_e}{T_e}$) increases. Accordingly, STs with characteristics of low magnetic field strength and high beta plasma are able to make favorable conditions for the study of LHFW coupling and absorption.

Comb-line antenna and klystron power system are successfully commissioned for LHFW experiment. RF system for the LHFW experiment consists of comb-line antenna, directional couplers, coaxial transmission lines, circulator, dummy load and klystron power system. Development of the antenna and klystron power system is accomplished by collaboration with Korea Atomic Energy Research Institute (KAERI) and

Kwangwoon University. Comb-line antenna to launch the fast wave polarization has frequency range from 468 MHz to 506 MHz and consequently $n_{\parallel 0}$ varies from 3 to 4.7. Klystron and comb-line antenna have been commissioned up to 10 kW of injected power at 500 MHz. Diagnostics for the LHFV experiment are developed. RF diagnostics measures coupling and reflection power of injected RF by directional couplers which is positioned in front of the antenna ports. Langmuir triple probe and single probe measure time varying electron density, temperature and ion saturation current in scrape off layer (SOL) region. Magnetic probe array measures power spectrum and parallel refractive index of the fast wave in plasma.

Coupling of LHFV is investigated by antenna-plasma coupling simulations in 3D toroidal geometry and preliminary experiments in VEST. Simulation results show that the combline antenna for VEST has characteristics of maximum plasma coupling (~90%) at ~500MHz with $n_{\parallel 0} \sim 4.5$, and gap size should be kept less than 1.5cm to couple the fast wave more than 50% of input power. Field patterns show that fast wave can propagate in even more dense plasma region than slow wave, which is the main feature for the fast wave current drive scheme. Preliminary coupling experiments with low power signal generator in VEST show that fast wave launching is experimentally achieved and coupling efficiency is consistent with the edge electron density and the simulation results in rather low density plasma ($n_{cutoff,fast} < n_e < n_{confluence}$). Fast wave coupling is enhanced contrary to the prediction in high density plasma ($\geq n_{confluence}$) where accessibility condition is not satisfied. The discrepancy between experimental observation and coupling simulation implies that another factor can play a major role in high density plasma overcoming the accessibility limit. Coupling simulation will make it possible to give prediction and analysis of the coupling characteristics for experiment. Especially, calculation of coupled power fraction of fast wave and slow wave can be utilized to study on heating and current drive in these

frequency ranges where both fast wave and slow wave can propagate.

Wave measurements using magnetic probes are performed with coupling experiments to investigate the propagation and coupling of LHFV in VEST. Discharges are operated at $B_0 = 0.1$ T where accessibility condition of LHFV is predicted to be very narrow due to high density in SOL plasma ($2-4 \times 10^{17} \text{ m}^{-3}$) which is rather higher than the confluence density ($\sim 1.5 \times 10^{17} \text{ m}^{-3}$) calculated from the $n_{\parallel 0} = 4.5$. Nevertheless, efficient coupling with low reflection is observed experimentally. n_{\parallel} -upshift of the fast wave from about 4 to 9 is measured at MP2 which is positioned at different poloidal and toroidal locations from the antenna. Propagation path of fast wave is largely modified compared to full wave simulation. Propagating waves are primarily detected in radially inward region ($R < 0.7$ m) even where accessibility condition is not satisfied without n_{\parallel} -upshift. Broadening of power spectrum is mostly caused by wave scattering than PDI. Consequently, the spectral broadening implicates that n_{\parallel} -upshift can take place via wave scattering mechanism. Expanded coupling regime in high density plasma is observed, implying that n_{\parallel} is shifted up via wave scattering right in front of the antenna. Intense scattering is expected in ST plasmas due to high plasma dielectric constant. It is observed that plasma dielectric constant, which includes both electron density and magnetic field strength, more directly exhibits the relation between wave coupling and plasma parameters than the case with electron density only. Scattering intensity and required minimum n_{\parallel} for efficient coupling increase with plasma dielectric constant. If n_{\parallel} -upshift via wave scattering is sufficiently enhanced with the increase of plasma dielectric constant, and is accordingly expanding and satisfying accessibility condition, then efficient coupling is possible in high density plasmas.

In conclusion, practical window for propagation and coupling of LHFV, which is the first difficulty of the scheme, is widened with the aid of n_{\parallel} -upshift via wave scattering

even though the accessibility condition is not satisfied right in front of the antenna. Significant n_{\parallel} -upshift is measured by magnetic probe array for the first time. Wave measurements reveal that accessibility conditions are largely modified from full wave simulation based on linear model by the n_{\parallel} -upshift and wave scattering. This study give new evidences of the n_{\parallel} -upshift in edge plasma for lower hybrid waves.

6.2. Future Work

Further investigation on the SOL plasma and wave property in front of the antenna should be considered for more direct evidence for the expanded accessibility conditions by understanding how n_{\parallel} is shifted up. Since n_{\parallel} -upshift is inversely proportional to R by toroidal effect, it plays a major role in propagation of lower hybrid waves in low aspect ratio ST plasma. Thus, investigation of plasma further inside is desired. In near future, magnetic probes are in plan to be installed at various locations along wave propagation path in order to trace n_{\parallel} -upshift of propagating waves.

According to the study on coupling and propagation of LHFV, heating and current drive will be attempted at higher B_t (~ 0.2 T) operation. Maximum power of 10 kW will be injected into hot plasmas and heating effect will be evaluated by hard x-ray measurement.

APPENDIX A. Antenna Conditioning [46]

In the past LHCD experiments, outgassing of the grill antenna during the power injection has been reported and studied in terms of lowering the pressure rise for long pulse operation [59, 60, 61, 62]. However, performance of the antenna has not been quantitatively investigated with the outgassing phenomenon and decrease of outgassing after so called RF conditioning has not been analyzed intensively. To optimize coupling efficiency of the antenna, evaluation of the antenna performance depending on the RF conditioning should be preceded.

In VEST, it is easy to conduct analysis and optimization of RF conditioning without transmitting RF power into vacuum vessel for plasma breakdown due to two-port structure of the comb-line antenna. Injected RF power from input port of the antenna is either reflected at the input port or transmitted to output port which is connected to dummy load or dissipated within the antenna. This paper presents quantitative analysis on the optimization of the antenna performance through the conditioning.

A.1. Immediate antenna operations after vacuum closing

Figure A.1 depicts schematic drawings of RF system and vacuum chamber with two directional couplers, a turbo molecular pump (TMP), a pressure gauge and residual gas analyzer (RGA) system. Pressure gauge and RGA system in VEST [63] are used to measure an outgassing pressure and to identify the outgassing sources.

Since injected RF power of more than 500 W for the conditioning considerably heats up current straps and inner wall of the antenna contrary to the low power measurement, outgassing and interaction with high RF field in the antenna cavity can give rise to reduction of transmitted power via ohmic losses. Therefore, $100-(R+T)$ [%] can be regarded as power dissipation. RF conditioning described in this section is defined as

surface cleaning by RF surface heating. Effect of the RF conditioning on antenna performance is discussed with the dissipated power and outgassing rate in following sections.

Immediate operations after vacuum closing show considerable reflection and power dissipation while diminishing transmitted power with poor reproducibility as demonstrated in Figure A.2. Significant amount of outgassing occurs in highly contaminated surface after vacuum break, and then initial weakly-ionized plasmas can be easily transitioned to normal glow discharges accompanying heat deposition to the inner surface of the antenna again and resultant additional outgassing. Each data points in Figure A.2 indicate a pulse and the pulse length is 500 ms. In the worst case of input power of about 1.3 kW, the injected power is even completely reflected and dissipated without transmission. In this case, reflection coefficient is 30% and dissipation coefficient is 70%. Repetitive shots at input power of about 2.7 kW improve performance of the antenna with the increase of transmission coefficient while decreasing reflection and dissipation coefficients. On average, coefficients of transmission, reflection, and dissipation are about 50%, 15%, and 35%, respectively.

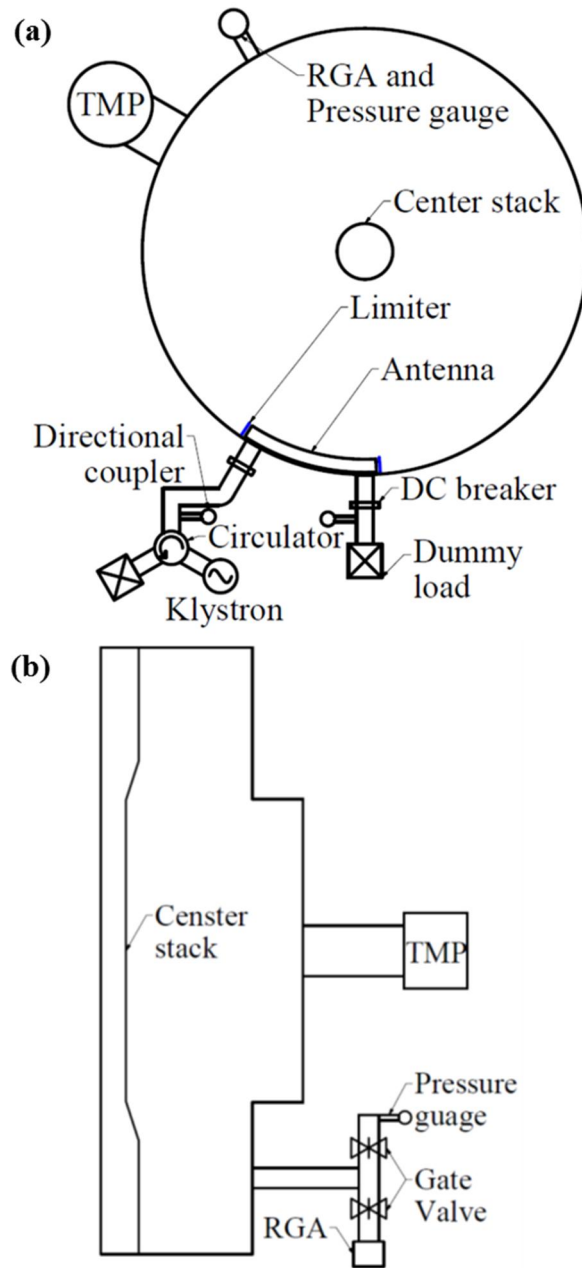


Figure A.1 Schematics of RF system, VEST chamber and diagnostic devices from (a) top and (b) side view.

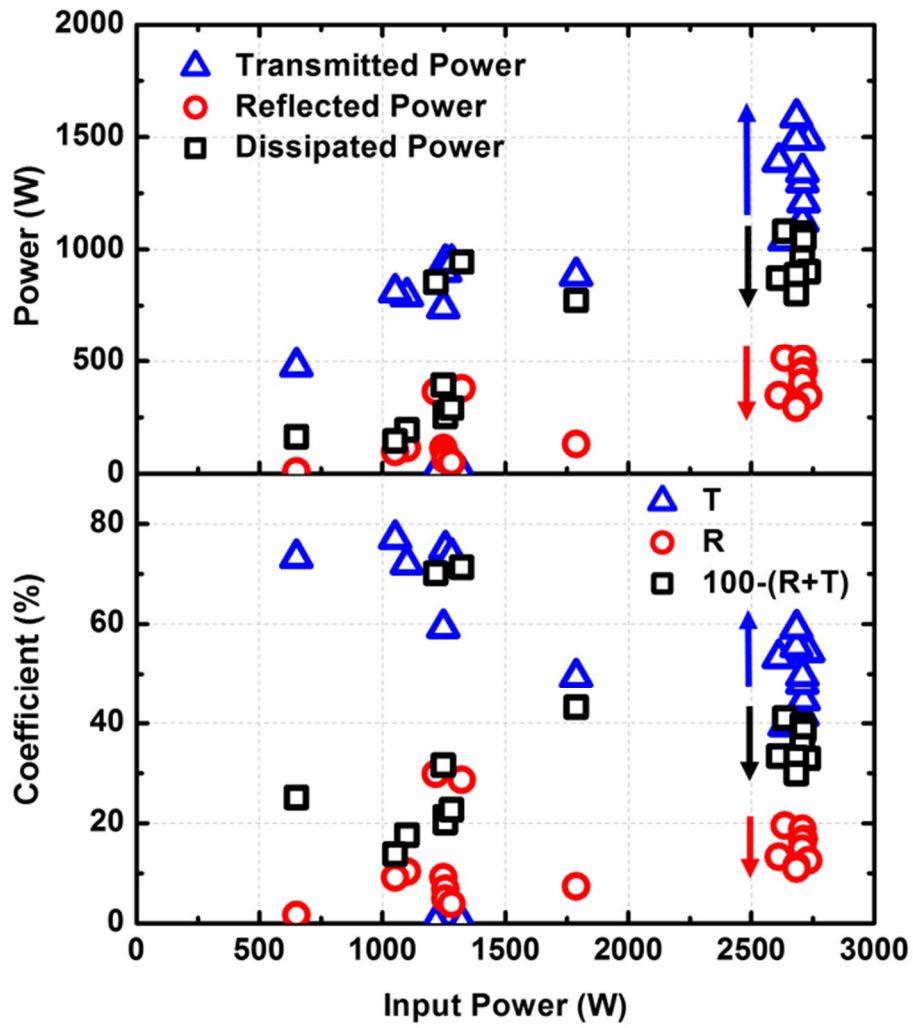


Figure A.2 Power and coefficients of transmission, reflection and dissipation in the antenna as a function of input power before the RF conditioning.

A.2. Analyses of Outgassing Characteristics

To identify outgassing spectrums, outgassing is monitored with RGA during RF conditioning which is performed by repetitively injecting pulse power of less than 8 kW with pulse length of 1 sec. Figure A.3 shows that water (18 amu) is the main outgassing source. The remaining sources, which are considered as hydrocarbons and carbon monoxide, seem to be produced by the water vapor and residual carbon from graphite structures such as reflector for interferometry in VEST chamber.

Outgassing rate (Q) during RF conditioning is obtained from the product of pressure rise (ΔP) and effective pumping speed (S_{eff}). To measure the effective pumping speed, leak rate (Q_{leak}) is calculated from pressure rise when vacuum chamber ($V = 3.7 \text{ m}^3$) is isolated ($S_{\text{eff}} = 0$) by closing valves between pumps and chamber. Effective pumping speed is calculated from the leak rate and ultimate pressure (P_u) in VEST chamber. $Q_{\text{leak}} = [VdP/dt]_{\text{close}} = 7.4 \times 10^{-5} [\text{Pa} \cdot \text{m}^3/\text{s}]$, $P_u = 7.4 \times 10^{-5} [\text{Pa}]$ and $S_{\text{eff}} = Q_{\text{leak}}/P_u = 0.97 [\text{m}^3/\text{s}]$. Outgassing rate during RF conditioning is measured as injected power varies from about 1 kW to 8 kW. Consequent dissipated power is lower than 3.2 kW as presented in Figure A.4. Figure A.4 shows that outgassing rate for the initial shots is almost proportional to dissipated power and slope (Q/P_d) displayed as dash lines decreases after shots. The slope (Q/P_d) means outgassing rate per dissipated power. Initial shots before RF conditioning are positioned in the steepest line indicating the largest amount of outgassing. After several shots, in conditioned stage, maximum dissipated power decreases from about 3200 W to 2000 W and slope declines by 90% indicating that outgassing rate per dissipated power is reduced to 10%.

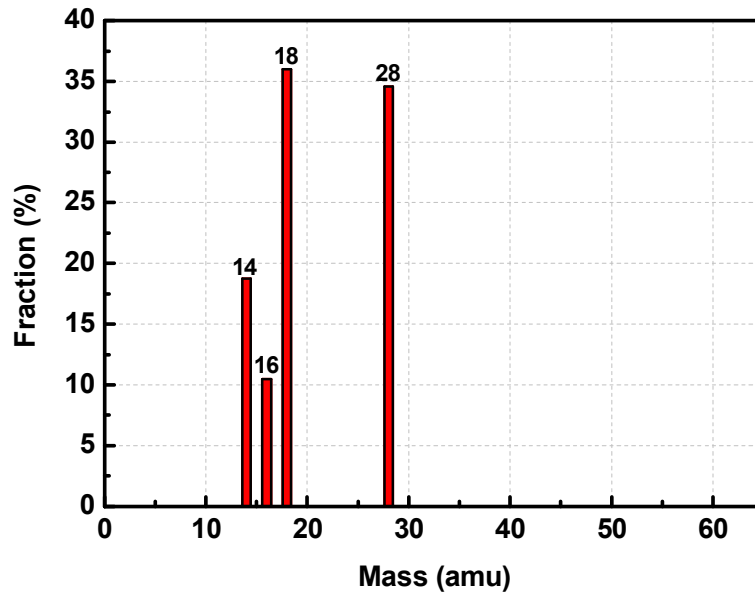


Figure A.3 Fraction of outgassing sources measured by RGA during RF conditioning for 1 hour (30 pulses).

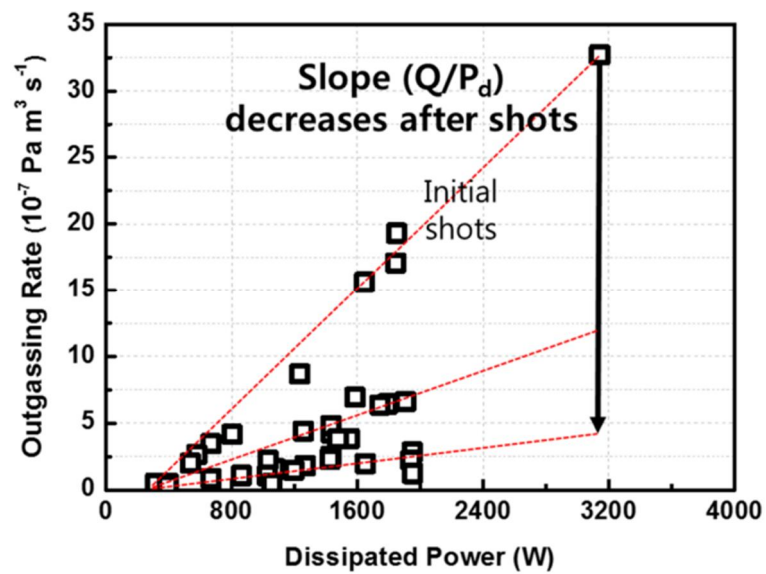


Figure A.4 Outgassing rate as a function of dissipated power.

A new dimensionless figure-of-merit (FM) to evaluate degree of the RF conditioning is defined by using the slope in Figure A.4 with dissipated power P_d and outgassing rate Q as following:

$$FM = \frac{Q}{P_d} \quad (A.1)$$

Low figure-of-merit means low outgassing rate at given dissipated power indicating well-conditioned stage as discussed above. Figure A.5 exhibits change of the figure-of-merit during RF conditioning shots. It is clearly shown that overall figure-of-merit decreases during the conditioning. It varies largely from order of 10^{-7} to 10^{-8} for the first two days and then it is reduced to the order of 10^{-9} in well-conditioned stage. In the conditioned stage (05. 28. ~ 05. 31.), figure-of-merit of each day decreases as shots are preceded by reducing the outgassing source at the surface and it is recovered to a certain level ($\sim 10^{-8}$) the next day by contamination of surface when the antenna is not running. Figure A.6 demonstrates that antenna performance, which is evaluated by the transmission, reflection, and dissipation coefficients, is improved with the decrease of FM value during RF conditioning.

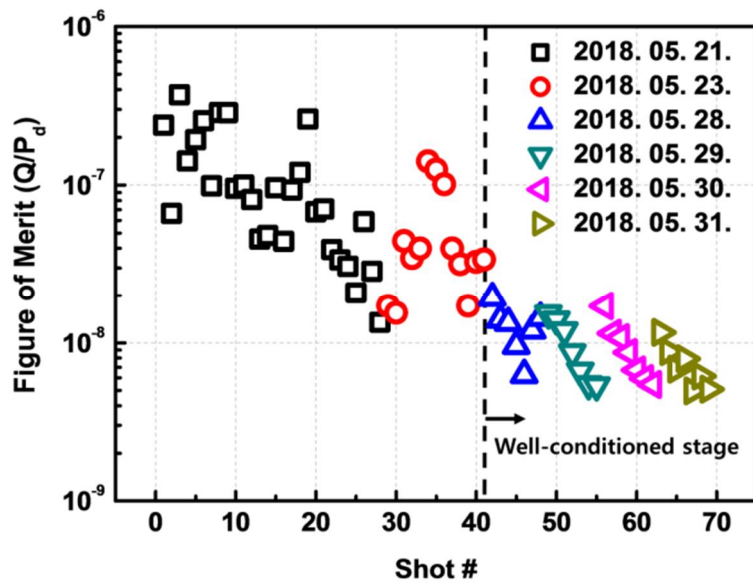


Figure A.5 Change of figure-of-merit during RF conditioning shots.

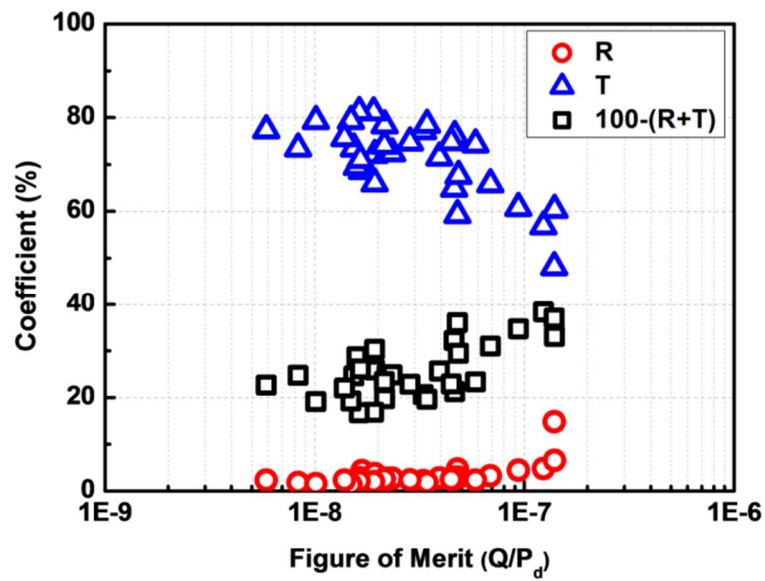


Figure A.6 Transmission, reflection and dissipation coefficients change depending on figure-of-merit (Q/P_d).

A.3. Improvement of Antenna Performance by RF conditioning

Transmission, reflection, and dissipation coefficients change before and after the RF conditioning at injected power of less than 10kW are summarized in the Figure A.7 (a). Before the conditioning, transmission coefficient clearly decreases depending on input power with the increase of reflection and dissipation coefficients as described in section A.1. After the conditioning, it is typically shown that overall dissipation coefficient is lower than 40% and transmission coefficient is higher than 60% with negligible reflection. Unlike the results before conditioning, power dependence of the coefficients is not observed indicating that surface of the antenna is sufficiently cleaned eliminating water within the injected power level.

Optimum performance of the antenna with low figure-of-merit is achieved after conditioning for 3 days a week (~40 shots). Under the optimized conditions, coefficients of transmission, reflection, and dissipation are about 80%, 2%, and 18%, respectively when the injected power is about 6 kW as shown in Figure A.7 (b). Transmission coefficient is almost doubled by intensive RF conditioning. Except the radiation loss of about 10% as noted in section A.1, power dissipation is reduced to below 10%. In this stage, dissipated power is almost saturated to about 1 kW regardless of increased input power leading to the decrease of dissipation coefficient in higher input power region. Achieved optimum FM value is about 5×10^{-9} as demonstrated in Figure A.5.

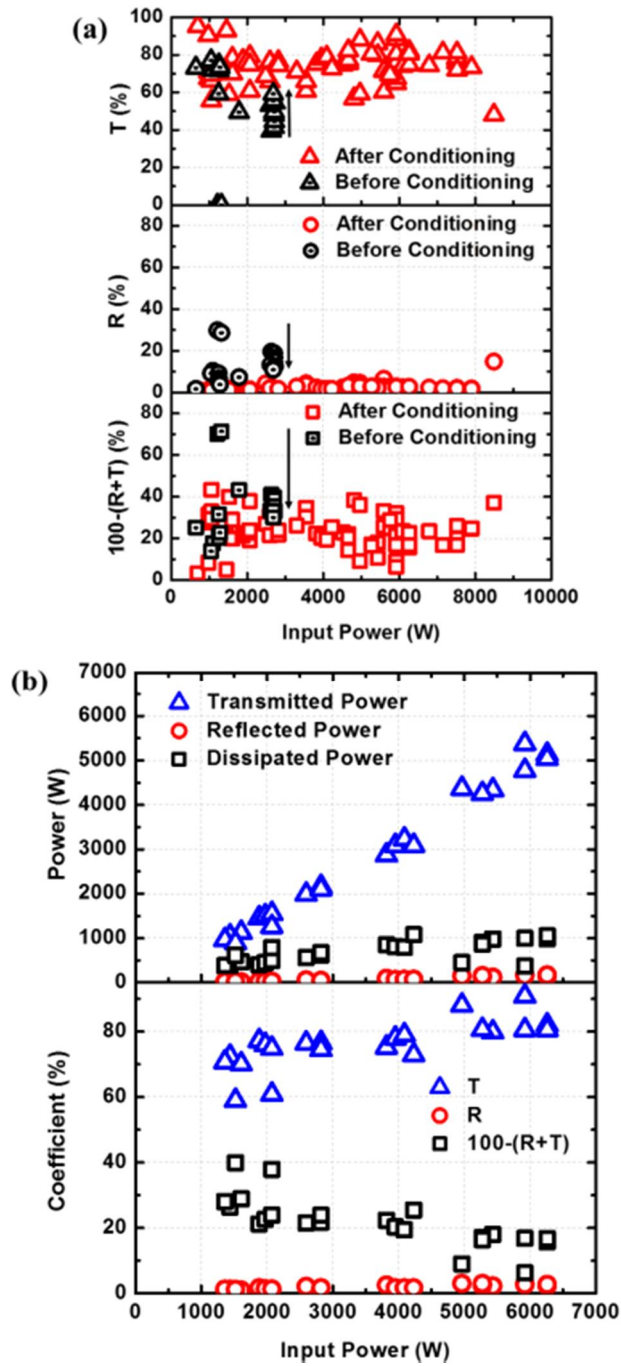


Figure A.7 (a) Transmission, reflection, and dissipation coefficients before and after RF conditioning. (b) Optimized performance of the antenna for 3 days a week.

In summary, Antenna performance is quantitatively analyzed by coefficients of transmission, reflection and dissipation with outgassing rate in order to investigate effect of RF conditioning on the antenna performance. RF conditioning is able to improve the antenna performance maximizing the transmission coefficient by eliminating impurities, which is identified to be mainly water, from antenna surfaces. A new figure-of-merit to evaluate degree of the RF conditioning is defined with outgassing rate per dissipated power, and successfully validated. Through the RF conditioning by repetitive shots, figure-of-merit value decreases largely from order of 10^{-7} to 10^{-9} . As a result, dissipation coefficient is reduced to below 10% while attaining the transmission coefficient of 80% with negligible reflection in well-conditioned stage in which the figure-of-merit value is about 5×10^{-9} . Antenna performance evaluated by transmission coefficient is almost doubled from intensive RF conditioning. Introduced new figure-of-merit provides a quantitative basis for antenna conditioning in order to improve antenna performance.

Bibliography

- [1] M. Kikuchi, K. Lackner and M. Q. Tran, *Fusion Physics*, Vienna: IAEA, 2012.
- [2] J. Wesson, *Tokamaks*, New York: Clarendon Press - Oxford, 2004.
- [3] B. B. Kadomtsev, *Tokamak Plasma: A Complex Physical System*, Bristol and Philadelphia: Institute of Physics Publishing, 1992.
- [4] F. M. Levinton, M. C. Zarnstorff, S. H. Batha, M. Bell, R. E. Bell, R. V. Budny, C. Bush, Z. Chang, E. Fredrickson, A. Janos, J. Manickam, A. Ramsey, S. A. Sabbagh, G. L. Schmidt, E. J. Synakowski and G. Taylor, "Improved confinement with reversed magnetic shear in TFTR," *Physical Review Letters*, vol. 75, p. 4417, 1995.
- [5] J. Team, "Fusion energy production from a deuterium-tritium plasma in the JET tokamak," *Nuclear Fusion*, vol. 32, p. 187, 1992.
- [6] M. Kikuchi, M. Azumi, S. Tsuji, K. Tani and H. Kubo, "Bootstrap current during perpendicular neutral injection in JT-60," *Nuclear Fusion*, vol. 30, p. 343, 1990.
- [7] [Online]. Available: <https://www.iter.org/proj/iterhistory>.
- [8] Masayuki Ono and Robert Kaita, "Recent progress on spherical torus research," *Physics of Plasmas*, vol. 22, p. 040501, 2015.
- [9] [Online]. Available: <https://www.iter.org/newsline/53/1589>.
- [10] M. Gryaznevich, R. Akers, P. G. Carolan, N. J. Conway, D. Gates, A. R. Field, T. C. Hender, I. Jenkins, R. Martin, M. P. S. Nightingale, C. Ribeiro, D. C. Robinson, A. Sykes, M. Tournianski, M. Valovi and M. J. Walsh, "Achievement of Record β in the START Spherical Tokamak," *Physical Review Letters*, vol. 80, p. 3972, 1998.

- [11] M. Ono and e. al., "Exploration of spherical torus physics in the NSTX device," *Nuclear Fusion*, vol. 40, p. 557, 2000.
- [12] B. Lloyd and e. al., "Overview of recent experimental results on MAST," *Nuclear Fusion*, vol. 43, p. 1665, 2003.
- [13] M. Brambilla, *Kinetic Theory of Plasma Waves: Homogeneous Plasmas*, Oxford: Clarendon Press, 1998.
- [14] N. J. Fisch, "Theory of current drive in plasmas," *Review of Modern Physics*, vol. 59, p. 175, 1987.
- [15] N. J. Fisch, "Confining a Tokamak Plasma with rf-Driven Currents," *Physical Review Letters*, vol. 41, p. 873, 1978.
- [16] S. Bernabei, C. Daughney, P. Efthimion, W. Hooke, J. Hosea, F. Jobes, A. Martin, E. Mazzucato, E. Meservey, R. Motley, J. Stevens, S. V. Goeler and R. Wilson, "Lower-Hybrid Current Drive in the PLT Tokamak," *Physical Review Letters*, vol. 49, p. 1255, 1982.
- [17] A. EKEDAHL, Y. BARANOV, J. DOBBING, B. FISCHER, C. GORMEZANO, T. JONES, M. LENNHOLM, V. PARAIL, F. RIMINI, J. ROMERO, P. SCHILD, A. SIPS, F. SOLDNER and B. TUBBING, "Profile control experiments in JET using off-axis lower hybrid current drive," *Nuclear Fusion*, vol. 38, p. 1397, 1998.
- [18] H. Zushi and e. al., "Steady-state tokamak operation, ITB transition and sustainment and ECCD experiments in TRIAM-1M," *Nuclear Fusion*, vol. 45, p. S142, 2005.
- [19] G. M. Wallace, R. R. Parker, P. T. Bonoli, A. E. Hubbard, J. W. Hughes, B. L. LaBombard, O. Meneghini, A. E. Schmidt, S. Shiraiwa, D. G. Whyte, J. C. Wright, S. J. Wukitch, R. W. Harvey, A. P. Smirnov and a. J. R. Wilson, "Absorption of

- lower hybrid waves in the scrape off layer of a diverted tokamak,” *Physics of Plasmas*, vol. 17, p. 082508, 2010.
- [20] S.-H. Kim, S.-H. Jeong, H. Lee, B. Lee, J.-G. Jo, H.-Y. Lee and Y.-S. Hwang, “Heating and current drive by fast wave in lower hybrid range offfrequency on Versatile Experiment Spherical Torus,” *Fusion Engineering and Design*, vol. 109, p. 707, 2016.
- [21] S. H. Kim, Y. S. Hwang, S. H. Jeong, S. J. Wang and J. G. Kwak, “A current drive by using the fast wave in frequency range higher than two timeslower hybrid resonance frequency on tokamaks,” in *22 Topical Conference on Radio-Frequency Power in Plasmas*, 2017.
- [22] M. Ono, “High harmonic fast waves in high beta plasmas,” *Physics of Plasmas*, vol. 2, p. 4075, 1995.
- [23] R. Prater, C. Moeller, R. Pinsker, M. Porkolab, O. Meneghini and V. Vdovin, “Application of very high harmonic fast waves for off-axis current drive in the DIII-D and FNSF-AT tokamaks,” *Nuclear Fusion*, vol. 54, p. 083024, 2014.
- [24] R. I. Pinsker, “Review of tokamak experiments on direct electron heating and current drive with fast waves,” in *AIP Conference Proceedings*, 1994.
- [25] J. Stevens, R. Bell, S. Bernabei, A. Cavallo, T. Chu, P. Colestock, W. Hooke, J. Hosea, F. Jobs, T. Luce, E. Mazzucato, R. Motley, R. Pinsker, S. V. Goeler and J. Wilson, “Lower hybrid experiments on PLT using grills with various $n \parallel$ spectral widths,” *Nuclear Fusion*, vol. 28, p. 217, 1988.
- [26] S. Ide, O. Naito, T. Kondoh, Y. Ikeda and K. Ushigusa, “Enhancement of Absorption of Lower Hybrid Wave by Filling the Spectral Gap,” *Physical Review Letters*, vol. 73, p. 2312, 1994.

- [27] J. Decker, Y. Peysson, J.-F. Artaud, E. Nilsson, A. Ekedahl, M. Goniche, J. Hillairet and D. Mazon, “Damping of lower hybrid waves in large spectral gap configurations,” *Physics of Plasmas*, vol. 21, p. 092504, 2014.
- [28] Y. Peysson, J. Decker, E. Nilsson, J.-F. Artaud, A. Ekedahl, M. Goniche, J. Hillairet, B. Ding, M. Li, P. T. Bonoli, S. Shiraiwa and M. Madi, “Advances in modeling of lower hybrid current drive,” *Plasma Physics and Controlled Fusion*, vol. 58, p. 044008, 2016.
- [29] E. Barbato and F. Romanelli, “Broadening of the lower hybrid k_{\parallel} spectrum by toroidal effects,” *Physics of Fluids B: Plasma Physics*, vol. 2, p. 2687, 1990.
- [30] F. Imbeaux and Y. Peysson, “Ray-tracing and Fokker–Planck modelling of the effect of plasma current on the propagation and absorption of lower hybrid waves,” *Plasma Physics and Controlled Fusion*, vol. 47, p. 2041, 2005.
- [31] M. Porkolab, S. Bernabei, W. M. Hooke, R. W. Motley and T. Nagashima, “Observation of Parametric Instabilities in Lower-Hybrid Radio-Frequency Heating of Tokamaks,” *Physical Review Letters*, vol. 38, p. 230, 1977.
- [32] K. Toi, K. Ohkubo, K. Kawahata, Y. Kawasumi, K. Matsuoka, N. Noda, I. Ogawa, Y. Ogawa, K. Sato, S. Tanahashi, T. Tetsuka, E. Kako, S. Hirokura, Y. Taniguchi, S. Kitagawa, Y. Hamada, J. Fujita and K. Matura, “Plasma current startup by lower hybrid waves in the JIPP T-IIU tokamak,” *Nuclear Fusion*, vol. 28, p. 147, 1988.
- [33] R. Cesario, A. Cardinali, C. Castaldo, F. Paoletti and D. Mazon, “Modeling of a Lower-Hybrid Current Drive by Including Spectral Broadening Induced by Parametric Instability in Tokamak Plasmas,” *Physical Review Letters*, vol. 92, p. 175002, 2004.

- [34] V. PERICOLI-RIDOLFINI, L. GIANNONE and R. BARTIROMO, “Frequency spectral broadening of lower hybrid waves in tokamak plasmas-causes and effects,” *Nuclear Fusion*, vol. 34, p. 469, 1994.
- [35] V. P. Ridolfini, M. Apicella, G. Calabr`o, C. Cianfarani, E. Giovannozzi and L. Panaccione, “Lower hybrid current drive efficiency in tokamaks and wave scattering by density fluctuations at the plasma edge,” *Nuclear Fusion*, vol. 51, p. 113023, 2011.
- [36] P. Bonoli and E. Ott, “Accessibility and Energy Depositon of Lower-Hybrid Waves in a Tokamak with Density Fluctuations,” *Physical Review Letters*, vol. 46, p. 424, 1981.
- [37] N. Bertelli, G. Wallace, P. T. Bonoli, R. W. Harvey, A. P. Smirnov, S. G. Baek, R. R. Parker, C. K. Phillips, E. J. Valeo, J. R. Wilson and J. C. Wright, “The effects of the scattering by edge plasma density fluctuations on lower hybrid wave propagation,” *Plasma Physics and Controlled Fusion*, vol. 55, p. 074003, 2013.
- [38] T. H. Stix, *Waves in Plasmas*, New York: Springer, 1992.
- [39] C. P. Moeller, R. W. Gould, D. A. Phelps and R. I. Pinsker, “Comblin antennas for launching traveling fast waves,” *AIP Conference Proceedings*, vol. 289, p. 323, 1994.
- [40] H. Ikezi and D. A. Phelps, “Traveling-Wave Antenna for Fast-Wave Heating and Current Drive in Tokamaks,” *Fusion technology*, vol. 31, p. 106, 1997.
- [41] R. I. Pinsker, “Development of impedance matching technologies for ICRF antenna arrays,” *Plasma Physics and Controlled Fusion*, vol. 40, p. A215, 1998.
- [42] T. Ogawa, K. Hoshino, S. Kanazawal, M. Saigusa, T. Ido, H. Kawashima, N. Kasuya, Y. Takase, H. Kimura, Y. Miura, K. Takahashi, C. Moeller, R. Pinsker, C.

- Petty and D. Phelps, "Radiofrequency experiments in JFT-2M: Demonstration of innovative applications of a travelling wave antenna," *Nuclear Fusion*, vol. 41, p. 1767, 2001.
- [43] Y. Takase, A. Ejiri, H. Kakuda, Y. Nagashima, T. Wakatsuki, O. Watanabe, P. Bonoli, O. Meneghini, S. Shiraiwa, J. Wright, C. Moeller, H. Kasahara, R. Kumazawa, T. Mutoh, K. Saito and T.-2. Group, "Development of a plasma current ramp-up technique for spherical tokamaks by the lower hybrid wave," *Nuclear Fusion*, vol. 51, p. 063017, 2011.
- [44] T. Wakatsuki, "A study of Non-inductive Plasma Current Start-Up Using the Lower Hybrid Wave in the TST-2 Spherical Tokamak," in *Doctoral Thesis*, Tokyo University, 2013.
- [45] H. Lee, S. Kim, S. Jung, J. Jo, H. Lee, Y. Hwang and B. Lee, "Traveling-wave antenna for the current drive using the fast wave in the lower hybrid-frequency range in the Versatile Experiment Spherical Torus (VEST)," *Fusion Engineering and Design*, p. published online, 2018.
- [46] J. Jo, J. Wang, S. H. Kim and Y. S. Hwang, "RF conditioning for the improvement of lower hybrid fast wave comb-line antenna performance on VEST," *Fusion Engineering and Design*, vol. 139, pp. 128-131, 2019.
- [47] J. Jo, Study on Electron Cyclotron Heating (ECH) Pre-ionization in Versatile Experiment Spherical Torus (VEST), Master's Thesis: Seoul National University, 2013.
- [48] S. Chen and T. Sekiguchi, "Instantaneous Direct-Display System of Plasma Parameters by Means of Triple Probe," *Journal of Applied Physics*, vol. 36, p. 2363, 1965.

- [49] Y. Takase and e. al., “Non-inductive plasma initiation and plasma current ramp-up on the TST-2 spherical tokamak,” *Nuclear Fusion*, vol. 53, p. 063006, 2013.
- [50] S. G. Baek, G. M. Wallace, T. Shinya, R. R. Parker, S. Shiraiwa, P. T. Bonoli, D. Brunner, I. Faust, B. L. LaBombard, Y. Takase and S. Wukitch, “Measurements of the parallel wavenumber of lower hybrid waves in the scrape-off layer of a high-density tokamak,” *Physics of Plasmas* , vol. 23, p. 050701, 2016.
- [51] T. Shinya, S. G. Baek, G. M. Wallace, S. Shiraiwa, Y. Takase, R. R. Parker, P. T. Bonoli, D. Brunner, I. Faust, B. L. LaBombard and S. Wukitch, “Identification of waves in the lower-hybrid frequency range in the scrape-off layer plasma of Alcator C-Mod,” *Nuclear Fusion*, vol. 57, p. 036005, 2016.
- [52] J. Jo, “Modified Propagation Path and Expanded Coupling Regime of Lower Hybrid Fast Wave by n_{\parallel} -Upshift via Wave Scattering in VEST,” *Physics of Plasmas*, vol. 26, p. 012506, 2019.
- [53] J. Jo, J. Wang, H. W. Lee, S. C. Kim, B. J. Lee, S. H. Kim and Y. S. Hwang, “Coupling study of fast wave near the lower hybrid frequency range in VEST,” *Physics of Plasmas*, vol. 25, p. 082511, 2018.
- [54] [Online]. Available: <http://www.comsol.com/>.
- [55] J. Jo, H. Y. Lee, S. C. Kim, S. H. Kim, Y. H. An and Y. S. Hwang, “Efficient pre-ionization by direct X-B mode conversion in VEST,” *Physics of Plasmas*, vol. 24, p. 012103, 2017.
- [56] D. G. Swanson, *Plasma Waves*, 2nd ed., London: Institute of Physics Publishing, 2003.
- [57] S. Wang, H. Wi, H. Kim, J. Kim, J. Jeong and J. Kwak, “Helicon wave coupling in KSTAR plasmas for off-axis current drive in high electron pressure plasmas,”

Nuclear Fusion, vol. 57, p. 046010, 2017.

- [58] P. L. Andrews and F. W. Perkins, “Spectral broadening of lower-hybrid waves by time-dependent density fluctuations,” *The Physics of Fluids*, vol. 26, p. 2546, 1983.
- [59] S. Maebara, M. Seki, K. Suganuma and Y. Ikeda, “Outgassing of the lower hybrid current drive antenna on JT-60U,” *Fusion Engineering and Design*, vol. 30, p. 253, 1995.
- [60] M. Seki, K. Obara, S. Maebara, Y. Ikeda, T. Imai, T. Nagashima, M. Goniche, J. Brossaud, C. Barral, G. Berger-By, P. Bibet, S. Poli, G. Rey and G. Tonon, “Outgassing measurement of the waveguide module for a steady state LHCD antenna,” *Fusion Engineering and Design*, vol. 30, p. 357, 1995.
- [61] S. Maebara, M. Goniche, F. Kazarian, M. Seki, Y. Ikeda, T. Imai, P. Bibet, P. Froissard and G. Rey, “Outgassing of plasma facing antenna front for lower hybrid wave launcher,” *Fusion Engineering and Design*, vol. 49, p. 269, 2000.
- [62] M. Goniche, P. B. F. Kazarian, S. Maebara, M. Seki, Y. Ikeda and T. Imai, “Outgassing of lower hybrid antenna modules during high-power long-pulse transmission,” *Journal of Vacuum Science & Technology A*, vol. 23, p. 55, 2004.
- [63] H. Lee, J. Yang, Y. Kim, S. Yang, Y. Kim, K. Lee, Y. An, K. Chung, Y. Na and Y. Hwang, “Development of wall conditioning and impurity monitoring systems in Versatile Experiment Spherical Torus (VEST),” *Fusion Engineering and Design*, vol. 109, p. 1082, 2016.

VEST 장치에서의 고속파 결합 연구

조 종 갑

에너지시스템공학부

(핵융합 및 플라즈마 공학 전공)

서울대학교 대학원

$2\omega_{lh}$ 보다 높은 저역혼성 주파수 영역의 고속파를 이용한 중심부 혹은 축 외 가열 및 전류구동이 저속파를 이용한 경우보다 높은 밀도의 플라즈마에서의 활용을 목표로 제안되었다. 고속파 발전을 위해 요구되는 컷오프 밀도는 일반적으로 저속파에 비해 수 백배 높다. 또한 높은 자기장과 나란한 방향의 전기장 성분을 위해 요구되는 높은 주파수는 좁은 결합 범위의 원인이 된다. 따라서 고속파 가열 및 전류구동을 실현하기 위해서는 안테나와 플라즈마 사이의 효율적인 결합이 가장 중요한 문제가 된다. 저역 파동의 흡수 조건을 만족하기 위해서는 플라즈마 내부에서 평행 굴절률의 상승이 일어날 것으로 이론적으로 예상되는데 이로 인해 파동의 접근 조건이 선형 이론으로부터 크게 바뀔 것으로 예상된다. 그러므로 고속파를 이용한 전류구동법의 원리 증명을 위해서는 결합 및 전파에 대한 집중적인 조사가 매우 중요한 시작점이다.

상용 전산모사 프로그램 COMSOL을 이용하여 주파수, 갭 크기, 전자 밀도 분포에 따른 고속파 결합의 특성을 조사했다. 500 MHz 부근에서 평행 굴절률의 값이 약 4.5를 가지며 안테나와 플라즈마 사이에 결합 효율이 가장

좋을 것으로 예측되었다. 결합 효율은 갭 크기가 0.5 cm에서 1 cm로 변함에 따라 90 %에서 60 %로 변했다. 이러한 조건에서 고속파 성분의 비율은 80 % 이상이다. 고속파의 결합과 전파는 결정적으로 컷오프 밀도 및 컨플루언스 밀도에 의해 결정되는 플라즈마 밀도 범위에 의해 결정된다. 저전력 파형 발생기를 이용한 예비 실험을 통해 안테나 앞에서 전자 밀도가 컷오프 밀도 이상 되는 시점에 고속파 결합 효율이 증가하기 시작함을 실증했다. 실험결과와 전산모사는 비교적 낮은 밀도에서는 일치하였지만, 컨플루언스 밀도 이상의 높은 밀도에서는 접근 조건을 만족하지 못함에도 전산모사의 예측과는 반대로 고속파 결합 효율이 증가하는 결과가 관측되었다. 이러한 차이는 높은 밀도의 플라즈마에서 또 다른 요인이 접근 조건의 한계를 극복하는 데에 영향을 끼쳤음을 암시한다. 실험결과와 전산모사 사이의 차이를 유발하는 원인을 파악하기 위해서 플라즈마 내부에서의 파동 측정을 고안했다.

고속파의 결합과 전파를 실험적으로 조사하기 위해서 자기장 탐침을 활용한 파동 측정을 VEST에서 수행하였다. 실험은 고속파 결합 효율이 낮거나 불가능할 것으로 예상되는 컨플루언스 밀도 보다 높은 고밀도 플라즈마에서 수행하였다. 결합 효율이 낮을 것으로 예상되는 플라즈마 전류가 25 kA 인 경우 평행 굴절률이 약 2배 정도 상승함을 측정했다. 파동의 전파 경로는 전산모사 결과와 매우 다름이 측정되었고, 결합 조건이 맞지 않는 중심부 플라즈마 영역으로의 진행이 가능했다. 이러한 평행 굴절률 상승 현상은 측정된 주파수 스펙트럼의 폭의 넓어짐 정도와 고속파의 주파수 범위($\omega_0/\omega_{th} \sim 15$), 약 20 % 정도의 높은 전자 밀도 변동을 통해 PDI 현상 보다는 파동 산란 현상과 긴밀한 관련이 있음이 관측되었다. 따라서 측정된 주파수 스펙트럼의 폭

이 넓어지는 현상은 평행 굴절률의 상승이 파동 산란 현상을 통해 발생함을 나타낸다. 고속파 결합이 불가능할 것으로 예상되는 플라즈마 전류가 100 kA 인 경우 오히려 고속파 결합 효율이 90 %까지 크게 증가함을 관측했다. 이때의 전자 밀도 변동은 낮은 플라즈마 전류의 경우와 비교해 큰 차이가 없었으나 크게 증가한 전자 밀도 및 플라즈마 유전 상수에 의해 강화된 파동 산란 현상이 그 원인으로 보인다.

결론적으로 파동 산란을 통한 평행 굴절률 상승을 통해 고속파의 접근 조건을 안테나 바로 앞에서조차 충족하지 못함에도 불구하고 실제적인 고속파의 결합 및 전파 범위가 고밀도 플라즈마로까지 넓어졌다. 유의미한 정도의 평행 굴절률 상승은 자기장 탐침을 이용해 처음으로 측정에 성공한 결과이다. 자기장 탐침으로 플라즈마 내부에서 전파하는 파동 측정을 통해 접근 조건이 기존의 선형 모델과 매우 큰 차이를 보임을 증명했다. 본 연구를 통해 가장자리 플라즈마에서 저역혼성 파동의 평행 굴절률 상승을 증명하는 새로운 증거들을 실험적으로 제시할 수 있었다.

주요어: 저역혼성 고속파, 구형 토러스, 결합, 접근 조건, 평행 굴절률 상승, 파동 산란.

학 번: 2013-30997